Acidification and CO_2-Driven Conditions in the Estuary and Gulf of St. Lawrence During 2025

Martine Lizotte, Marjolaine Blais, Joël Chassé, Peter S. Galbraith, Anne-Josée Hébert, Michel Starr

Regional Sciences Branch
Quebec Region
Pelagic and Ecosystemic Sciences Division
Fisheries and Oceans Canada
Maurice Lamontagne Institute
850, Route de la Mer
Mont-Joli, QC
G5H 3Z4

2026

Canadian Technical Report of Hydrography and Ocean Sciences 429

Fisheries and Oceans Canada | Pêches et Océans Canada

Canada

Canadian Technical Report of Hydrography and Ocean Sciences

Technical reports contain scientific and technical information of a type that represents a contribution to existing knowledge but which is not normally found in the primary literature. The subject matter is generally related to programs and interests of the Oceans and Science sectors of Fisheries and Oceans Canada.

Technical reports may be cited as full publications. The correct citation appears above the abstract of each report. Each report is abstracted in the data base *Aquatic Sciences and Fisheries Abstracts.*

Technical reports are produced regionally but are numbered nationally. Requests for individual reports will be filled by the issuing establishment listed on the front cover and title page.

Regional and headquarters establishments of Ocean Science and Surveys ceased publication of their various report series as of December 1981. A complete listing of these publications and the last number issued under each title are published in the *Canadian Journal of Fisheries and Aquatic Sciences*, Volume 38: Index to Publications 1981. The current series began with Report Number 1 in January 1982.

Rapport technique canadien sur l'hydrographie et les sciences océaniques

Les rapports techniques contiennent des renseignements scientifiques et techniques qui constituent une contribution aux connaissances actuelles mais que l'on ne trouve pas normalement dans les revues scientifiques. Le sujet est généralement rattaché aux programmes et intérêts des secteurs des Océans et des Sciences de Pêches et Océans Canada.

Les rapports techniques peuvent être cités comme des publications à part entière. Le titre exact figure au-dessus du résumé de chaque rapport. Les rapports techniques sont résumés dans la base de données *Résumés des sciences aquatiques et halieutiques*.

Les rapports techniques sont produits à l'échelon régional, mais numérotés à l'échelon national. Les demandes de rapports seront satisfaites par l'établissement auteur dont le nom figure sur la couverture et la page de titre.

Les établissements de l’ancien secteur des Sciences et Levés océaniques dans les régions et à l'administration centrale ont cessé de publier leurs diverses séries de rapports en décembre 1981. Vous trouverez dans l'index des publications du volume 38 du *Journal canadien des sciences halieutiques et aquatiques*, la liste de ces publications ainsi que le dernier numéro paru dans chaque catégorie. La nouvelle série a commencé avec la publication du rapport numéro 1 en janvier 1982.

Canadian Technical Report
of Hydrography and Ocean Sciences 429

2026

Acidification and CO_2-Driven Conditions in the Estuary and Gulf of St. Lawrence During 2025

by

[1]Martine Lizotte, [1]Marjolaine Blais, [2]Joël Chassé, [1]Peter S. Galbraith, [1]Anne-Josée Hébert, [1]Michel Starr

[1]Regional Sciences Branch
Quebec Region
Pelagic and Ecosystemic Sciences Division
Fisheries and Oceans Canada
Maurice Lamontagne Institute
850, Route de la Mer
Mont-Joli, QC
G5H 3Z4

[2]Regional Sciences Branch
Gulf Region
Gulf Fisheries Centre
Fisheries and Oceans Canada
P.O. Box 5030
Moncton, NB
E1C 9B6

© His Majesty the King in Right of Canada, as represented by the Minister of the Department of Fisheries and Oceans, 2026

This work is licensed under the Open Government Licence

Cat. No. Fs 97-18/429E-PDF ISBN 978-1-100-01210-0 ISSN 1488-5417
https://doi.org/10.60825/y1n0-8k84

Correct citation for this publication:

Lizotte, M., Blais, M., Chassé, J., Galbraith, P.S., Hébert, A.-J., Starr, M. 2026. Acidification and CO_2-Driven Conditions in the Estuary and Gulf of St. Lawrence During 2025. Can. Tech. Rep. Hydrogr. Ocean Sci. 429: v + 70 p. https://doi.org/10.60825/y1n0-8k84

TABLE OF CONTENTS

Abstract iv

Résumé v

1. Introduction 1

2. Methods 2

2.1 Sampling 2

2.2 Background on carbonate chemistry metrics 4

2.3 Analyses 6

2.3.1 CO_2-carbonate system laboratory analyses 6

2.3.2 CO_2-carbonate system calculations and data visualization 7

2.4 Annual anomaly scorecards 8

3. Results 9

3.1 Total alkalinity, dissolved inorganic carbon and carbonate system vulnerability index 9

3.1.1 High-frequency monitoring station 9

3.1.2 EGSL regions 10

3.2 Potential of hydrogen 11

3.2.1 High-frequency monitoring station 11

3.2.2 EGSL regions 12

3.3 Partial pressure of CO_2 13

3.3.1 High-frequency monitoring station 13

3.3.2 EGSL regions 13

3.4 Indices of biogenic calcium carbonate formation and dissolution 15

3.4.1 High-frequency monitoring station 15

3.4.2 EGSL regions 16

4. Discussion 18

4.1 Surface to seafloor: environmental gradients in CO_2-driven conditions 18

4.1.1 Surface and upper waters: atmosphere-influenced and CIL-conditioned carbonate dynamics 19

4.1.2 Deeper subsurface waters: from channel depths to shelf bottoms 19

4.2 Perspectives on EGSL regional vulnerability to CO_2-driven stressors 21

5. Key findings 23

Acknowledgements 26

References cited 27

6. Tables 41

Figures 42

Appendices 67

ABSTRACT

Lizotte, M., Blais, M., Chassé, J., Galbraith, P.S., Hébert, A.-J., Starr, M. 2026. Acidification and CO_2-Driven Conditions in the Estuary and Gulf of St. Lawrence During 2025. Can. Tech. Rep. Hydrogr. Ocean Sci. 429: v + 70 p. https://doi.org/10.60825/y1n0-8k84

This report presents an overview of marine acidification and CO2-driven conditions in the Estuary and Gulf of St. Lawrence (EGSL) for 2025, based on data collected through the Atlantic Zone Monitoring Program and the Aquatic Climate Change Adaptation Services Program, led by Fisheries and Oceans Canada. Regional observations are compared against climatological means to assess anomalies and trends of the carbonate system. Key indicators, including pHT, the carbonate system vulnerability index (CSVI), partial pressure of CO2 (pCO2), saturation states of aragonite (ΩA) and calcite (ΩC), and the substrate-inhibitor ratio (SIR), reveal regionally variable and depth-structured stressor patterns across the EGSL. The year 2025 was marked by a broad signal of near-normal or subdued anomalies in several subsurface depth layers, particularly in deep and near-bottom waters entering the Gulf. Despite this attenuation of anomalies relative to recent years, carbonate-system conditions remained unfavourable in several areas, with persistent hypercapnia, aragonite and calcite undersaturation, low SIR, and reduced buffering capacity, most notably in the Estuary and Northwest Gulf. The 200 m depth layer continues to stand out as a zone of sustained vulnerability, with multiple indicators reaching or exceeding established CO2-driven stress thresholds.

RÉSUMÉ

Lizotte, M., Blais, M., Chassé, J., Galbraith, P.S., Hébert, A.-J., Starr, M. 2026. Acidification and CO_2-Driven Conditions in the Estuary and Gulf of St. Lawrence During 2025. Can. Tech. Rep. Hydrogr. Ocean Sci. 429: v + 70 p. https://doi.org/10.60825/y1n0-8k84

Ce rapport présente un aperçu des conditions liées à l'acidification marine et à l'accumulation de CO2 dans l'estuaire et le golfe du Saint-Laurent pour l'année 2025, à partir de données recueillies dans le cadre du Programme de monitorage de la zone atlantique et du Programme de services d'adaptation aux changements climatiques aquatiques, menés par Pêches et Océans Canada. Les observations régionales sont comparées aux moyennes climatologiques afin d'évaluer les anomalies et les tendances du système des carbonates. Les indicateurs clés, incluant le pHT, l'indice de vulnérabilité du système des carbonates (CSVI), la pression partielle de CO2 (pCO2), les états de saturation de l'aragonite (ΩA) et de la calcite (ΩC), ainsi que le ratio substrat-inhibiteur (SIR), révèlent des patrons de stress variables selon les régions et structurés en fonction de la profondeur. L'année 2025 a été caractérisée par des anomalies généralement atténuées ou près de la normale dans plusieurs couches de profondeur, en particulier dans les eaux profondes qui entrent dans le golfe. Malgré cette atténuation des anomalies, les conditions du système des carbonates sont demeurées défavorables dans plusieurs régions, avec une hypercapnie persistante, une sous-saturation en aragonite et en calcite, et une capacité tampon réduite, particulièrement dans l'estuaire et le nord-ouest du golfe. La profondeur de 200 m continue de se distinguer comme une zone de vulnérabilité soutenue, où plusieurs indicateurs atteignent ou dépassent les seuils de stress liés au CO2.

1. INTRODUCTION

The acidification of seawater, commonly referred to as “ocean acidification” (OA), is a well-documented consequence of the accumulation of anthropogenic carbon dioxide (CO_2) in the atmosphere (Caldeira and Wickett 2003, Gattuso and Hansson 2020). Rising CO_2 levels lower surface seawater pH, which has declined by about 0.002 units annually across much of the global open ocean since the 1980s, with only minor decadal fluctuations (Doney et al. 2009, Bates et al. 2014, Lauvset et al. 2015). Although seemingly modest, this decline represents part of a long-term trend in which seawater acidity is increasing at a rate 10 times faster than during any period of the past 300 million years (Hönisch et al. 2012). Overall, global ocean acidity has risen by roughly 40 % since the pre-industrial Holocene epoch, reflecting an apparently small pH drop, from ~8.18 (pre-industrial) to 8.04 (in 2024), that has significant consequences on global ocean chemistry (EEA 2024, NOAA 2024). Recently, OA has been formally recognized as a transgressed planetary boundary (Findlay et al. 2025, Sakschewski et al. 2025) underscoring its significance as a threat to Earth system stability.

Unlike the steady pH decline at the surface of the open ocean, pH conditions in estuarine, coastal, nearshore and marginal sea systems show complex trends driven by local and regional processes (Cai et al. 2021, Hall et al. 2023, Li et al. 2025). In these environments, variability in pH may reflect not only atmospheric CO_2 uptake (Caldeira and Wickett 2003) but also the combined influence of external inputs, such as nutrient enrichment, watershed weathering, river discharge, and groundwater flow, as well as internal processes including water mass mixing, organic matter cycling, carbonate mineral reactions, and seasonal ice dynamics (Gruber et al. 2019, Chen et al. 2023, Middelburg et al. 2020, Cai et al. 2021). In many regions, the downward transport of anthropogenic inorganic carbon, combined with intensified respiration-driven metabolic carbon accumulation, leads to a faster rate of acidification below the pycnocline than in surface waters, a phenomenon termed “enhanced or intensified ocean acidification” (Cai et al. 2011, Lauvset et al. 2020, Fassbender et al. 2023, Findlay et al. 2025, Knor et al. 2025).

The marine carbonate system is a fundamental component of the global carbon cycle and acts as a natural chemical buffer that moderates changes in seawater pH (Zeebe and Wolf-Gladrow 2001, Emerson and Hedges 2008). Through a series of reversible reactions among dissolved CO_2, carbonic acid (H_2CO_3), bicarbonate (HCO_3^-), and carbonate (CO_3^{2-}), the ocean absorbs and stores large quantities of atmospheric CO_2, thereby reducing the rate of atmospheric accumulation and buffering natural variations in carbon inputs (Gruber et al. 2023). However, the rapid increase in anthropogenic CO_2 emissions has altered this equilibrium, decreasing the buffering capacity of seawater and driving widespread changes in ocean carbonate chemistry (Caldeira and Wickett 2003, Doney et al. 2020, Gattuso and Hansson 2020). By modifying the chemical environment experienced by marine organisms, this anthropogenic perturbation of the natural carbonate buffering system may affect physiology, growth, calcification, and reproduction through disruptions to acid-base regulation and energy allocation (Stumpp et al. 2012, Dixson et al. 2015, Melzner et al. 2020, Figuerola et al. 2021, Leung et al. 2022, Padilla-Gamino et al. 2022, Shi and Li 2024). For example, decreases in seawater pH and increases in H^+ concentrations, together with declining saturation states for calcite (Ω_C) and aragonite (Ω_A) that may increase dissolution risk, can increase the energetic costs of biocalcification and maintaining calcium carbonate structures in organisms such as coccolithophores, foraminifera, pteropods, mollusks, crustaceans, echinoderms, and corals (Fabry et al. 2008, Ries et al. 2009, Kroeker et al. 2010, Jokiel 2011, Thomsen et al. 2015, Clements and Hunt 2015, Toyofuku et al. 2017, Pousse et al. 2020). The occurrence of water masses with $pCO_2 > 1000$ µatm, a condition termed ocean hypercapnia (McNeil and Sasse 2016), reflects extremely CO_2-enriched marine

environments that may exacerbate challenges associated with organismal acid-base regulation and respiration. However, biological responses to elevated CO_2 occur along a continuum and are highly species- and life stage-dependent, with physiological, behavioural, and developmental effects often observed at pCO_2 levels below the hypercapnia threshold (Nilsson et al. 2012, McNeil and Sasse 2016, Feely et al. 2018, Noor and Das 2019). Developing a thorough understanding of the carbonate system in Canadian waters is thus fundamental for guiding ecosystem-based fisheries management and climate vulnerability assessments (Barclay et al. 2026).

Systematic measurements of OA parameters in the Estuary and Gulf of St. Lawrence (EGSL) have been ongoing since fall 2014 as part of the Atlantic Zone Monitoring Program (AZMP, see Therriault et al. 1998) and the Aquatic Climate Change Adaptation Services Program (ACCASP) of Fisheries and Oceans Canada (DFO) (Gibb et al. 2023, Blais et al. 2026, Galbraith et al. 2026a). Although some historical data on acidification in the Atlantic Zone exists (e.g., Mucci et al. 2011), DFO programs have provided continuous and detailed monitoring, building on the foundation of these earlier, more sporadic measurements. This fundamentally important monitoring has strengthened DFO's capacity to characterize and forecast marine ecosystem conditions, quantify climate-related changes, and identify emerging vulnerabilities. This document outlines chemical conditions associated with multifaceted CO_2-driven conditions in the EGSL, with a focus on the spatiotemporal variability of several key CO_2-carbonate system indices. The chemical environment of this dynamic estuarine and semi-enclosed sea reflects the complex interplay of physical and biological processes. For a comprehensive description of the 2025 physical and biogeochemical conditions in the EGSL, readers should consult Galbraith et al. (2026b) and Blais et al. (2026), respectively.

2. METHODS

2.1 SAMPLING

To ensure the highest standards of data quality, all sampling and processing procedures followed the Guide to Best Practices for Ocean CO_2 Measurements (Dickson et al. 2007), and the AZMP protocols (Mitchell et al. 2002). The field measurements presented in this report were gathered during dedicated AZMP surveys conducted in early summer and fall each year, as well as at one high-frequency monitoring station (Figure 1, and Table 1). Additional oceanographic data from multidisciplinary surveys, typically carried out in summer (Chamberland et al. 2025), and from the mackerel egg survey were included for all years for which these data are available (2014–2025, Table 1). In this document, sampling stations were grouped into six main regions for which carbonate system indices are presented (Figure 1):

- Estuary: The lower St. Lawrence Estuary is a transitional zone where freshwater from the St. Lawrence River mixes with incoming marine waters. Circulation and mixing in this region are shaped, among other factors, by tidal dynamics, winds and bathymetric features. A defining characteristic of the zone is the Laurentian Channel, a submerged valley that typically reaches depths exceeding 200 metres.

- Northwest Gulf: This area is typically deep (over 200 m). It is heavily influenced by freshwater runoff from the St. Lawrence River at the surface, and by dense waters flowing along the Laurentian Channel at greater depths.

- Centre Gulf and Cabot Strait: Generally deep (over 200 m), this region is directly affected by deep water mixing at the continental slope. It receives a mixture of warm North Atlantic Central Water (NACW) with a Gulf Stream signature and cold Labrador Current Water (LCW) through the Cabot Strait. For the sake of brevity, this region is referenced as Centre Gulf throughout the text.

- Northeast Gulf: Characterized by deep channels and a relatively wide shelf (less than 100 m deep), this region has high surface salinity. It encompasses the Anticosti and Esquiman subregions.

- Magdalen Shallows: This shallow region (~100 m and less) is typically warm at the surface during summer and is significantly influenced by the Gaspé Current. Chaleur Bay is included within this region.

- Northumberland Strait: This very shallow region (typically ~30 m and less) is characterized by a west-to-east flowing corridor between Prince Edward Island and the mainland, strong tidal mixing, and some of the warmest summer bottom waters in the southern Gulf of St. Lawrence (Chassé et al. 2014, Koutitonsky 1991).

Due to limited chemical data availability in Mécatina Trough (Figure 1), acidification indices are not included in the annual scorecards but remain visible on the spatial maps.

Details about the 2025 sampling surveys are provided in Table 1, while Figure 1 and Figure 2 summarize the sampling effort during the seasonal surveys and at the high-frequency monitoring station, respectively. Rimouski station (depth of 320 m) is a high-frequency monitoring station and has been sampled for CO_2-carbonate system parameters since 2014. Sampling at this station occurs approximately weekly during the summer, once or twice a month from early spring to late fall, and rarely in winter (except during the AZMP wintertime survey of the Gulf of St. Lawrence (Galbraith 2006), but no acidification parameters are measured then) due to the presence of sea ice. It is representative of the conditions in the Estuary. In 2025, Rimouski station was visited on 25 occasions that included the collection of carbonate system parameters.

Sampling along the oceanographic sections and at the high-frequency monitoring station includes a Conductivity-Temperature-Depth profile (CTD; temperature, salinity, fluorescence, dissolved oxygen) and water collection using Niskin bottles (2 m, 10 m, 15 m, 25 m, 50 m, 100 m, 200 m, 300 m, 400 m, bottom). In this report, the term “surface” refers to the uppermost sampled layer (top 10 m). Water collected from Niskin bottles is typically analyzed for seawater pH on the total scale (pH_T), total alkalinity (TA), and dissolved inorganic carbon (DIC). From these measurements, key ocean acidification metrics, including calcium carbonate saturation states for calcite (Ω_C) and aragonite (Ω_A), partial pressure of carbon dioxide (pCO_2), and substrate-inhibitor ratio (SIR), are derived using TA–pH_T pairs when available (see section 2.3.2 for further details). The carbonate system vulnerability index (CSVI), used to assess buffering capacity, is calculated from the difference between TA and DIC.

2.2 BACKGROUND ON CARBONATE CHEMISTRY METRICS

Total alkalinity, dissolved inorganic carbon, and carbonate system vulnerability index

Total alkalinity, expressed in μmol kg^{-1} of seawater, is operationally defined as the excess of proton acceptors over proton donors. Monitoring TA variability can provide insights on the seawater's buffering capacity against acidification. Higher TA levels generally indicate a greater capacity to neutralize acidity, which plays a critical role in maintaining stable pH conditions under rising concentrations of DIC from both anthropogenic and metabolic sources. It is important to note that this report does not distinguish between organic and inorganic contributions to TA, a known source of uncertainty in carbonate system assessments, particularly in coastal and high-dissolved organic matter (DOM) environments (Hu 2020, Kerr et al. 2021). Dissolved inorganic carbon, also expressed in μmol kg^{-1} of seawater, is the sum of all dissolved inorganic carbon species (aqueous [$CO_{2(aq)}$], carbonic acid [H_2CO_3], [HCO_3^-], and [CO_3^{2-}]). Monitoring DIC provides insights into carbon transport, storage, and transformation across the EGSL and helps identify changes in freshwater inflows, nutrient loading, and organic matter decomposition, among other processes.

In this report, TA and DIC are presented as distinct parameters; however, we emphasize their differential ([TA] – [DIC]) as a combined diagnostic metric to better highlight areas of heightened carbonate system vulnerability. The difference between TA and DIC ([TA] – [DIC]), hereby referred to as the carbonate system vulnerability index, is a fundamental metric of ocean water (Xue and Cai 2020) and can be used as a simple baseline indicator of buffering capacity. When CSVI values are positive, TA exceeds DIC and buffering capacity is high. When TA and DIC approach equivalence ([TA] – [DIC] = 0), even small increases in CO_2 concentration can trigger disproportionately large declines in pH. At this critical juncture, the buffering capacity of the carbonate system becomes substantially weakened (Frankignoulle et al. 1994, Egleston et al. 2010), resulting in non-linear and amplified pH responses to incremental CO_2 inputs. Negative CSVI values, where DIC exceeds TA, may indicate even more reduced buffering capacity and enhanced vulnerability to acidification. These conditions often reflect zones of intense organic matter degradation and CO_2 accumulation (see examples in Martínez-Trejo et al. 2024). CSVI is favoured over the [TA] / [DIC] ratio used elsewhere (e.g., Wang et al. 2013) because the [TA] – [DIC] difference behaves more conservatively under ocean mixing, is less affected by non-linear changes during mixing and variations in physical conditions, and more directly reflects biogeochemical influences on acidification. This framing supports a more integrated assessment of buffering capacity and acidification potential, particularly in regions subject to multiple interacting stressors. As such, CSVI provides a robust, interpretable and scalable metric for tracking OA processes across diverse marine environments (Xue and Cai 2020, Martínez-Trejo et al. 2024, Reimer et al. 2024).

Potential of hydrogen

The pH of seawater quantifies the activity of hydrogen ions and therefore its "acidity", expressed on a logarithmic scale as $-\log_{10}([H^+])$ (Caldeira and Wickett 2003, Feely et al. 2004, 2008). In this report, terms such as "more acidic" or "acidification" are used to describe the trend of increasing acidity levels (increasing H^+). Oceanic waters are typically mildly alkaline with a pH > 7.0 (genuinely acidic conditions, referring to water with a pH < 7.0, are unlikely to be encountered in marine systems). Unless noted otherwise, pH values in this report are expressed on the total hydrogen-ion scale (pH_T), the standard reporting scale for marine

carbonate chemistry (Dickson et al. 2007, Riebesell et al. 2010). Exceptions include the substrate-inhibitor ratio (see section 3.4) which uses H^+ on the free scale.

Partial pressure of CO_2

Partial pressure of CO_2 refers to the portion of the total pressure exerted by CO_2 in a mixture of gases dissolved in seawater (Emerson and Hedges 2008). Over the global ocean, pCO_2 typically varies from about 100 µatm to 1000 µatm (1 µatm = 10^{-6} atm = 0.101325 Pascal) (Takahashi et al. 2017). However, hypercapnic conditions (pCO_2 > 1000 µatm) are observed in contemporary oceanic environments (Feely et al. 2018) and often co-occur with hypoxia (Arroyo et al. 2022). Subsurface remineralization inherently links high pCO_2 (hypercapnia), low pH (acidification), and low dissolved oxygen values (hypoxia), which can be intensified on continental shelves, estuarine and semi-enclosed oceanic environments by locally driven processes (Cai et al. 2011, 2017, 2021, Feely et al. 2016, 2018, Chan et al. 2017, 2019). While direct pCO_2 measurements are the most accurate means to characterize these conditions, pCO_2 estimates derived from other CO_2-carbonate system variables (pH_T and TA as used in this report) remain highly valuable, though they come with a higher degree of uncertainty, especially for depths below 100 m due to increased hydrostatic pressure (Weiss 1974, Orr et al. 2015). Seacarb is currently one of the few packages that compute ocean carbonate chemistry while accounting for hydrostatic pressure effects on pCO_2, potentially reducing some of the associated uncertainties (Orr et al. 2015, Gattuso et al. 2024).

Indices of calcium carbonate mineral formation and dissolution

The saturation state of $CaCO_3$ minerals (Ω_{CaCO_3}) is a dimensionless ratio that compares the concentration of dissolved calcium (Ca^{2+}) and CO_3^{2-} ions in seawater to their saturation concentrations. It is a fundamental metric of the thermodynamic potential of $CaCO_3$ dissolution: $\Omega < 1$ indicates that dissolution of exposed carbonate structures is favoured (Morse et al. 2007). While acidification-driven dissolution is primarily an inorganic process governed by undersaturation states of $CaCO_3$ minerals, marine calcification is biologically mediated and therefore more complex. Biogenic $CaCO_3$ occurs in several polymorphic forms, mostly as calcite and aragonite, but also as vaterite, and hydrated or amorphous phases, each with distinct crystal structures and solubilities (Mucci 1983, Mann 2001, Bach 2015). Marine organisms may exert biological control over which polymorphs they produce by modulating conditions at their calcification sites and using organic macromolecules as crystallization templates (Stolarski et al. 2025). Consequently, many taxa deposit one or a mixture of tailored polymorphs: coccolithophores and foraminifera mainly form calcite (sometimes Mg-rich), corals and pteropods mainly produce aragonite, and mollusks, echinoderms, and crustaceans combine multiple forms depending on tissue and function (see Table 1 in Stolarski et al. 2025). Because aragonite is more soluble than calcite (Mucci 1983), aragonite-secreting organisms, particularly those with unprotected $CaCO_3$ structures, are generally more susceptible to dissolution under acidifying conditions. Calcifying marine organisms may experience acute or chronic stress responses well before carbonate undersaturation occurs, often when the saturation state of $CaCO_3$ minerals falls within the range of 1 to 2. This document focuses on two critical thresholds: 1) $\Omega = 1$, the thermodynamic dissolution boundary for $CaCO_3$ (Morse et al. 2007); and 2) a conservative biological threshold of $\Omega = 1.5$, deemed suboptimal for marine life, as it is associated with measurable physiological impacts and considered an early warning level for adverse biological effects (Dixson et al. 2010, Keppel et al. 2012, Gazeau et al. 2013, Waldbusser and Salisbury 2014, Long et al. 2016, Rodríguez-Domínguez et al. 2018, Bednaršek et al. 2019, Siedlecki et al. 2021).

Biocalcification typically involves uptake of Ca^{2+} and HCO_3^- as substrates (Mann 2001, Allemand et al. 2004, Mackinder et al. 2010, Stumpp et al. 2012, Cyronak et al. 2016, Kahil et al. 2021). The specific pathways of biocalcification vary widely among taxa, involving different modes of inorganic carbon acquisition and sensitivity to proton (H^+) concentrations (Mann 2001). This physiological and taxonomic diversity makes it difficult to predict the net response of marine calcifiers based solely on variability in the Ω metric (Bach 2015, Ninokawa et al. 2024). Recognizing that net biological calcification is controlled by physiological processes that extend beyond mineral saturation state alone, Bach (2015) proposed the substrate-inhibitor ratio (SIR) as a complementary metric for assessing the influence of carbonate chemistry on biocalcification. The SIR is defined as the ratio of the substrate ($[HCO_3^-]$) to the waste product ($[H^+]$). A higher SIR ($[HCO_3^-]/[H^+]$ in mol μmol^{-1}) indicates more favourable conditions for calcification, emphasizing the importance of HCO_3^- as a calcification substrate (e.g., Jokiel 2011, 2013, Bach 2015, Cyronak et al. 2016). It also acknowledges the need for organisms to overcome biochemical inhibition from waste protons, as H^+ must be expelled when HCO_3^- is used to form $CaCO_3$ (Roleda et al. 2012, Cyronak et al. 2016). Under elevated OA conditions, the exchange of H^+ between internal cellular compartments and external seawater becomes increasingly difficult, thereby raising the energetic cost of maintaining internal pH homeostasis (Toyofuku et al. 2017, Ziveri et al. 2025). As noted earlier, while pH is typically presented on the total scale, the hydrogen ion concentrations in the ratio $[HCO_3^-]/[H^+]$ (in mol μmol^{-1}) are expressed on the free scale. This distinction is biologically relevant, as marine calcifiers interact directly with free ions in their environment. An SIR threshold of 0.100 mol μmol^{-1} is adopted as a conservative indicator of conditions where inhibitory proton concentrations outweigh bicarbonate substrate availability by an order of magnitude. End-of-century carbonate chemistry projections yield SIR values approaching ~0.100 (Bach 2015), a regime associated with reduced calcification across multiple taxa (e.g., Cyronak et al. 2016). Although the SIR provides a straightforward numerical measure to conceptualize $CaCO_3$ production and enhance our understanding of how changing chemical conditions affect calcifying organisms, it does not fully encompass the intricate relationships among carbonate system variables that are believed to drive biocalcification. For example, Ninokawa et al. (2024) suggest that biocalcification responses may be governed by separate effects of HCO_3^- availability and pH, highlighting a limitation of representing calcification potential using a single ratio or carbonate-system metric.

2.3 ANALYSES

2.3.1 CO_2-carbonate system laboratory analyses

Seawater pH_T is determined spectrophotometrically using the dye perturbation method (Clayton and Byrne 1993, Dickson 2010). A volume of 40 µl of purified 2 mM m-cresol purple solution (University of South Florida) is added to approximately 28 mL of seawater sample held at 25 ± 0.5 °C in a 10 cm cylindrical quartz cell (100 mm length), and thoroughly mixed. Absorbances at 434, 578, and 730 nm are recorded with a temperature-controlled Agilent Technologies Cary 60 spectrophotometer, and blank-corrected ratios are used to calculate pH_T. While pH measurements are not corrected for dye perturbation, the m-cresol purple dye solution is visually inspected daily, and measurements are conducted to ensure its stability over time. Analytical precision and accuracy are evaluated daily by comparing measurements of a tris(hydroxymethyl)aminomethane (TRIS) buffer solution prepared at a salinity of 30 (Millero 1986). Both TRIS buffer and m-cresol purple reference solutions are verified every two days to ensure the reliability of calibration standards. Typical precision and accuracy are ± 0.003 pH units or better.

Total alkalinity is determined using open-cell potentiometric titration (Mintrop et al. 2000, Dickson 2010) with an automated sampling system. Each 104 mL seawater sample is warmed to 25 ± 0.5 °C and titrated with 0.1 M hydrochloric acid to the Gran equivalence point using a computer-controlled Dosimat (Metrohm AG, USA) dispenser coupled with a combination glass electrode. Certified Reference Materials (CRM, Dickson) are analyzed regularly (every 2 days) and used to adjust titrant concentration, providing a correction factor applied to all sample alkalinity calculations. TA analytical precision, determined from repeated analyses of bulk seawater, is reported as < 1.5 µmol kg^{-1}.

Total dissolved inorganic carbon is quantified using an automated sampling and gas extraction system coupled to a coulometric analyzer (Johnson et al. 1993). A measured aliquot of 17.5 mL of seawater, equilibrated at 25 ± 0.5 °C, is transferred into a stripping chamber containing 1 mL of phosphoric acid (8.5 %). Acidification liberates CO_2, which is purged from the sample by ultrahigh-purity nitrogen gas and directed to a coulometric cell for titration and photometric quantification. Dickson CRM is analyzed daily to calibrate the coulometer prior to sample measurements. Analytical precision for DIC is < 2 µmol kg^{-1}.

2.3.2 CO_2-carbonate system calculations and data visualization

Various seawater CO_2-carbonate system parameters, including pCO_2, Ω_A, Ω_C, CSVI, and SIR are calculated using in situ values of salinity (S), temperature (T), pH (typically on the total scale unless otherwise specified, e.g., for the SIR which reports H^+ on the free scale), total alkalinity (TA), and dissolved inorganic carbon (DIC) data with the Seacarb package (version 3.3.3) for R (Gattuso et al. 2024). Salinity and temperature values are extracted from CTD profiles at depths corresponding to the sampled bottles (e.g., Figure 2). The following constants are applied according to best-practice recommendations (Orr et al. 2015): the first and second dissociation constants for carbonic acid, K_1 and K_2 computed on the total scale (Lueker et al. 2000), the hydrogen sulfate constant K_{HSO_4} (Dickson 1990), the hydrogen fluoride constant K_f (Perez and Fraga 1987) is used as the default unless temperature or salinity are outside specified ranges, then Dickson and Riley (1979) is used, and total boron following Lee et al. (2010). When possible, the measured TA-pH_T pair is used to determine pCO_2, Ω_A, and Ω_C, SIR, and other OA metrics as this pair provides the best consistency in this region (Raimondi et al. 2019, Gibb et al. 2023). Data visualization is performed using R software (R version 4.4.2 - “Pile of Leaves”). Temporal data interpolation for the vertical water column plots at Rimouski station is conducted using the nonparametric Locally Estimated Scatterplot Smoothing (Loess) method, which effectively handles noisy data, provides a robust fit, and assists in capturing underlying trends (Moraga 2023). Temporal trends at Rimouski station (2014–2025) were assessed using ordinary least squares linear regression, with post-estimation Shapiro-Wilk, Durbin-Watson, and Breusch-Pagan diagnostics. Where autocorrelation was detected, first-order autoregressive generalized least squares were adopted for reported slopes and confidence intervals; heteroscedasticity-consistent robust standard errors and Sen’s nonparametric slope were computed as supplementary checks. Spatial data interpolation for regional maps is conducted using an Inverse Distance Weighting (IDW) interpolation method, computed on a standardized 2 km-resolution grid, with IDW weights calculated using a power factor of 2 (squared inverse distance). Estimations at each grid point are constrained to a local neighbourhood defined by a maximum search radius of 0.7° longitude and 0.35° latitude. The cross-sectional vertical transects use a two-step approach to couple continuous horizontal spatial variability with discrete vertical sampling profiles. Pre-interpolated IDW values are extracted along the geographical coordinates defining each transect axis to form a two-dimensional distance-by-depth matrix, which is then transformed into a continuous vertical profile using

Radial Basis Function interpolation with a Thin Plate Spline algorithm that produces smoother transitional gradients across water masses (Majdisova and Skala 2017).

2.4 ANNUAL ANOMALY SCORECARDS

Normalized anomalies for the indices presented in scorecards are computed for both Rimouski station and the EGSL regions. Each anomaly is calculated as the difference between a variable's annual average and its climatological mean over the 2014–2025 reference period, divided by the standard deviation (SD) for the same period. For the Northumberland Strait region, the spatial climatology is presently based on observations from 2017 to 2025 due to the absence of data in earlier years. The climatology used this year extends the previous reference period, which ended in 2020, by five years. This longer reference period generally increases the estimated SD and consequently reduces the magnitude of normalized anomalies, consistent with the methodological approach described by Blais et al. (2026). A caveat of using short climatologies for carbonate chemistry dynamics is that these reference periods may already incorporate some degree of anthropogenic acidification and other CO_2-driven changes, potentially biasing recent anomaly estimates toward smaller magnitudes. In contrast, temporally extending the baseline to include earlier years could yield more pronounced recent anomalies and provide a more robust representation of cumulative changes in pH and other carbonate system parameters over time.

Anomalies are displayed as scorecards, where above-normal anomalies are shown in shades of red, and below-normal anomalies in shades of blue, with increasing colour intensity corresponding to greater deviations from the mean. White cells represent anomalies within ± 1/2 SD and are considered normal conditions (i.e., similar to climatology). Grey cells indicate insufficient or missing data. To depict environmental variation patterns across the Northwest Atlantic shelf, zonal scorecards summarizing anomalies in TA, DIC, pH_T, SIR, pCO_2, Ω_C, and Ω_A from all AZMP regions are presented in Galbraith et al. (2026a). Caution is required when interpreting anomaly scorecards, as anomalies describe relative departures from climatological means and may therefore indicate above-normal or below-normal conditions even when absolute values remain within ranges associated with environmental stress or vulnerability.

Annual anomalies of CO_2-carbonate system indices are derived from mean annual values estimated at the high-frequency monitoring station and across the six EGSL regions shown in Figure 1. These estimates are generated using Gaussian General Linear Models (GLMs), a statistical approach frequently applied within the AZMP framework (e.g., Blais et al. 2026). Because chemical oceanographic datasets often exhibit uneven sampling and sparse observations, GLMs provide a robust framework for adjusting seasonal and spatial imbalances, reducing bias from irregular data coverage. The models applied were as follows:

For the high-frequency monitoring station:
$\log_{10}(y) = \alpha + \beta_{Year} + \delta_{Month} + \varepsilon$

For the regional analyses:
$\log_{10}(y) = \alpha + \beta_{Year} + \delta_{Season} + \gamma_{Station} + \varepsilon$

where y is the response variable, α is the intercept, and ε is the error. The GLM is applied to each region separately. For Rimouski station, β and δ are the categorical effects for year and month, respectively. For the EGSL regions, β, δ, and γ are the categorical effects of year, season, and station, respectively. Prior to model fitting, values are $\log_{10}$ transformed to account for the skewed distribution of observations. Least square means computed using type III sums of squares are used as standardized annual estimates to account for uneven seasonal and spatial sampling. Although adjusted R^2 values are generally low and categorical effects sometimes nonsignificant, GLMs remain appropriate for generating standardized annual means that are more robust than simple arithmetic averages when data coverage is uneven. Detailed GLM outputs (significance (*p*-value) of each factor and adjusted R^2) are presented in Appendices 1 and 2.

While comparing 2025 carbonate-system data against a relatively short and recent climatological baseline (2014–2025) has limitations, such as reduced ability to capture long-term variability and potential bias from short-term anomalies, the approach remains valuable for current assessments. This is especially true in deeper waters, where limited ventilation allows CO_2 to accumulate, leading to clearer ocean acidification signals even when using a relatively short climatological baseline. Although the short reference period may be less informative for surface waters, it can still reveal meaningful changes and help identify emerging patterns when interpreted with appropriate context and caution. Confidence in the assessment of the surface reference state and in the identified long-term trends will increase as these measurements are repeated and longer time series become available for analysis.

3. RESULTS

Dynamic estuarine and semi-enclosed oceanic environments, like the St. Lawrence marine system, exhibit substantial variability in their chemical properties, shaped by complex physical and biological interactions. While this report provides details about acidification and other CO_2-driven conditions, comprehensive descriptions of the 2025 physical and biogeochemical conditions in the EGSL are provided in Galbraith et al. (2026b) and Blais et al. (2026), respectively.

3.1 TOTAL ALKALINITY, DISSOLVED INORGANIC CARBON AND CARBONATE SYSTEM VULNERABILITY INDEX

3.1.1 High-frequency monitoring station

Vertical profiles of CSVI at Rimouski station (Figure 3) illustrate the seasonal and depth-dependent variability in carbonate buffering conditions. CSVI typically decreases with increasing depth. In the climatology, CSVI values remain relatively stable within the Cold Intermediate Layer (CIL : typically, 50–150 m; Galbraith et al. 2026b), while the upper-water values display greater seasonal variability, reflecting the stronger influences of surface processes. Beyond 200 m, climatological CSVI values remain below 0 µmol kg^{-1} for most of the year, with values dropping below −6 µmol kg^{-1} from October to December.

The 2025 CSVI depth profiles revealed a more vertically extensive and temporally persistent depletion of carbonate buffering capacity than indicated by the 2014–2025 climatology. The CSVI = 0 threshold straddled the lower boundary of the CIL (~150 m) for most of the year, while waters below 200 m exhibited sustained CSVI values in the −6 to −25 µmol kg^{-1} range from

May through November. This extended period of reduced deep-water buffering capacity exceeded the shorter period of low CSVI observed primarily in late autumn in the climatology, indicating that in 2025 low-CSVI conditions developed earlier and extended over a larger portion of the deep-water column. Overall, CSVI anomalies at Rimouski Station in 2025 were predominantly below- to near-normal. The deep-water CSVI decrease observed during summer 2025 was consistent with concurrent changes in its two constituent terms, TA and DIC (Figure 3). Although TA exhibited pronounced positive anomalies below ~200 m from June through September, suggesting enhanced buffering at depth, the simultaneous DIC accumulation and positive anomaly pattern at depth outweighed this effect during the summer months leading to mostly below-normal deep CSVI anomalies. Several processes may have contributed to the parallel increases in TA and DIC, including advection of deep-water masses enriched in both constituents and enhanced remineralization under low-oxygen conditions (e.g., denitrification, Pascal et al. 2025). Viewed together, these concurrent changes underscore that buffering capacity is governed by the interplay between TA and DIC rather than by the behaviour of either term on its own.

3.1.2 EGSL regions

Across all six EGSL regions, CSVI annual averages generally exhibit a vertical gradient, decreasing from surface to deeper waters, reflecting a broad-scale decline in buffering capacity with depth (Figure 4). Surface waters exhibit the highest CSVI climatological values. Buffering capacity begins to decline at 50 m, followed by a marked drop at 100 m across all regions. At 200–300 m, several sites, including Rimouski station and the Estuary, exhibit low, near-zero, or negative climatological average CSVI values, indicating a substantially reduced buffering capacity. Although the overall decline in CSVI from the surface to intermediate depth often extends into deep waters, many regions show localized increases in climatological CSVI near the bottom. These increases generally remain within the range of variability observed at the adjacent depth layer but suggest more complex carbonate system dynamics near the seafloor. Interpretation of near-bottom conditions is further complicated by regional bathymetric variability, as this depth category integrates observations collected at different absolute depths rather than at a single fixed depth. The near-bottom anomalies in CSVI coincide with TA and DIC signals that are spatially variable across regions (Figure 5), likely shaped by the combined influence of local physical, chemical, and biological processes, and potentially benthic-pelagic coupling.

Temporal analysis indicates a general reduction in buffering capacity over the past decade, at depth (100 m and deeper). The early part of the sampling period (2014–2019) is broadly characterized by higher CSVI values and more frequent above-normal anomalies (Figure 4). Beginning around 2020–2021, however, below-normal conditions become more spatially widespread and increasingly evident at depth. Particularly vulnerable sites, such as Rimouski station and the Estuary, show a clustering of below-normal anomalies in recent years, suggesting potential shifts in deeper carbonate system dynamics. Since 2019, deep waters (200–300 m) of the Estuary have consistently remained below the CSVI threshold of zero, indicating persistently reduced buffering capacity. More recently, the Northwest Gulf has approached this threshold, with near-zero to negative CSVI values emerging in 2023 at 200 m and persisting in subsequent years. 2025 was marked by mostly normal to below-normal CSVI anomalies at depths of 100 m and deeper. At 200 m, the Estuary (including Rimouski station) registered the third-lowest CSVI average values in the 2014–2025 record, while the Northwest Gulf showed the second-lowest values, tied with 2024. Despite the improvement in 2025 CSVI

conditions at 300 m in the Estuary (including at Rimouski station), the annual average values remained below the threshold of zero, indicating that deep waters in this region continue to exhibit reduced buffering capacity. Near-bottom CSVI values were generally normal across the EGSL, apart from a subdued above-normal anomaly at Rimouski station (Figure 4). This broad near-normal signal reflects the interplay of diverging TA–DIC patterns at depth (Figure 5), where increases or decreases in one constituent were often offset by opposing changes in the other, yielding muted CSVI anomalies despite substantial variability in the underlying carbonate system.

Spatial distributions of climatological CSVI values at 200 and 300 m (Figure 6) display a pronounced channel-oriented gradient. Buffering capacity decreases from mouth to head in the Laurentian and Anticosti Channels, while the pattern is less distinct in the Esquiman Channel (see Figure 1 for geographic landmarks). Most regions maintain positive climatological CSVI, but values approach zero in the Estuary. In 2025, buffering capacity at 200 m was weaker than the climatological average in the Estuary and parts of the Northwest Gulf where weakly below-normal CSVI anomalies were observed (Figure 6). The eastward expansion of the CSVI threshold contour in 2025 marked a spatial expansion of reduced buffering capacity along the Laurentian Channel at this depth. This pattern likely resulted from the combined influence of near-normal to weakly below-normal TA anomalies (Figure 7), and weakly above-normal DIC conditions (Figure 8) in the Estuary and parts of the Northwest Gulf. At 300 m, CSVI anomalies in 2025 were broadly near normal to weakly above normal across the Laurentian Channel. Near-bottom waters showed mixed buffering conditions in 2025, with a predominance of near-normal and weak above- or below-normal CSVI anomalies. The near-bottom waters at the mouth of the Laurentian Channel in Cabot Strait exhibited an above-normal CSVI plume feature that closely corresponded to the below-normal DIC anomaly observed in the same area (Figure 8). This increase in CSVI occurred despite a concurrent decrease in TA (Figure 7), indicating that the DIC reduction at depth was sufficiently large relative to the TA decline to produce a net increase in carbonate buffering capacity**.**

3.2 POTENTIAL OF HYDROGEN

3.2.1 High-frequency monitoring station

Vertical pH_T climatological values show a consistent reduction with increasing depth, with waters below 100 m exhibiting limited seasonal variability (Figure 9). Surface climatological pH_T shows greater seasonal variability, driven by dynamic physical and biogeochemical processes. The highest pH_T values (and lowest pCO_2 values; Figure 9) are observed in the euphotic layer during summer, coinciding with the activity of photosynthetic phytoplankton communities and warmer surface waters, both of which contribute to the reduction of CO_2 content (Borges and Gypens 2010, Hall et al. 2023).

From late April through August 2025, much of the water column exhibited below-normal pH_T anomalies (Figure 9). Beginning in late summer, these anomaly patterns weakened, giving way to predominantly near-normal conditions across most depths from September to December. The 2025 anomaly pattern at depth contrasted markedly with that observed in recent years. Unlike 2022–2024, when monthly near-bottom pH_T values consistently diverged from the climatological mean, the 2025 time series showed a clear return to the 2014–2025 climatological envelope (Figure 10). Near-bottom pH_T remained mostly within expected seasonal ranges throughout the

year. Acidification rates derived from the 2014–2025 record continue to indicate a statistically significant long-term decline in near-bottom pH_T, with a linear trend of −0.004 pH units yr^{-1} ($p < 0.001$). Although modest in magnitude, this decline represents an approximate 10 % increase in hydrogen ion concentration over a decade. This persistent downward trend underscores that the apparent stabilization of 2025 values occurred within the context of an ongoing decrease in deep-water pH_T.

3.2.2 EGSL regions

The pH_T scorecards show a depth-dependent gradient across EGSL regions (Figure 11). Surface waters show the highest climatological values, with 2014–2025 pH_T means from 7.92 and 7.93 in Northumberland Strait and the Estuary up to 8.02 in other regions. Climatological pH_T averages decline with depth, likely reflecting organic matter remineralization combined with limited CO_2 ventilation of deeper waters. At 100 m, climatological pH_T values drop by 0.1–0.2 units as compared to the surface. The lowest climatological pH_T values occur near 300 m, reaching 7.54 in the Estuary and 7.74 in the Centre Gulf. Near-bottom waters exhibit slightly higher climatological average pH_T than at 300 m (or at 100 m in the Magdalen Shallows), since average bottom depth is generally shallower than 300 m, but they remained more acidified than surface layers. Highest near-bottom climatological pH_T values are found in shallow near-coastal waters of the Magdalen Shallows and Northumberland Strait regions.

The observational record indicates a progressive acidification over the past decade (Figure 11 and Figure 12), particularly in waters deeper than 100 m. The early part of the sampling period (2014–2019) is broadly characterized by higher pH_T values and more frequent above-normal anomalies (Figure 11). The year 2020 marks the beginning of multiple below-normal pH_T anomalies across several EGSL regions, particularly in 100 m waters and deeper. A clear and consistent trend of predominantly below-normal pH_T anomalies is observed at 200 m across all deep regions since 2020 (Figure 11), pointing to broad-scale persistence of acidification at this intermediate depth. This trend continued in 2025 in the Estuary and Northwest Gulf with below-normal spatial pH_T anomalies at 200 m (Figure 12). At this depth, 2025 registered the second-lowest annual pH_T values in the 2014–2025 record for the Estuary and Northwest Gulf, following several years since 2020 with record or near-record low pH_T conditions (Figure 11). The spatial 2025 pH_T anomalies at 300 m were mostly near normal to weakly above normal across the deep regions (Figure 12). Near-bottom pH_T distributions and anomalies were more spatially heterogeneous reflecting localized processes across wide-ranging bottom relief.

3.3 PARTIAL PRESSURE OF CO_2

3.3.1 High-frequency monitoring station

The climatological vertical and seasonal distribution of pCO_2 at Rimouski station reveals a well-defined stratification of pCO_2 throughout the year (Figure 9, Figure 10). Surface waters down to ca. 150 m show variability, generally oscillating between ~400 to 800 µatm, with values fluctuating seasonally. Minimum surface pCO_2 values occur in spring and early summer, reflecting biological CO_2 drawdown during spring, followed by a progressive increase through late summer and fall. This seasonal rise likely reflects reduced CO_2 uptake later in the phytoplankton growth season and the influence of accumulated respiratory CO_2 produced through organic-matter remineralization. The fall deepening of the CIL (Galbraith et al. 2026b, Fig. 67) likely also contributes to elevated subsurface CO_2 during this period. At greater depths, pCO_2 levels are consistently elevated. The 1000 µatm threshold, marking hypercapnic conditions, is positioned below the CIL, at approximately 150 m, and remains relatively vertically stable throughout the seasonal survey period of the climatology (2014–2025). Below this depth, climatological pCO_2 values increase further, reaching 1300 µatm and higher in near-bottom waters (Figure 9), indicating a persistent hypercapnic state at Rimouski station since measurements began in 2014.

From late April through August 2025, much of the water column displayed above-normal pCO_2 paired with below-normal pH_T anomalies, marking a coherent early-season departure toward elevated pCO_2 and reduced pH_T relative to the 2014–2025 climatology (Figure 9). Consistent with this pattern, the hypercapnic threshold shoaled in 2025, with pCO_2 values above 1000 µatm reaching depths near ~100 m, substantially shallower than its typical climatological position near 150 m. The threshold subsequently deepened toward its climatological depth in late summer and fall. Beginning in September, the anomaly structure weakened, giving way to predominantly near-normal pCO_2 anomalies across most depths through to December. This seasonal contrast is consistent with the DIC structure observed in 2025 (Figure 3), particularly at depth, where elevated DIC concentrations and positive anomalies during summer coincided with above-normal pCO_2, with both variables returning toward near-normal conditions in fall. Near-bottom pCO_2 values in 2025 remained hypercapnic throughout the year, generally exceeding 1200 µatm, but unlike 2022–2024, they did not diverge strongly from the climatological envelope (Figure 10). This attenuation of deep-water pCO_2 anomalies aligns with the improved oxygen conditions documented in 2025 (Blais et al. 2026, Fig. 6), when near-bottom oxygen saturation was also close to the climatological mean. Together, these observations indicate that while deep waters at Rimouski remained CO_2-rich and oxygen-poor in 2025, the severity of hypercapnic and hypoxic pressures was reduced relative to the preceding five-year period.

3.3.2 EGSL regions

The pCO_2 scorecards show a pronounced vertical gradient across all EGSL regions, inversely mirroring pH_T (Figure 11). Surface waters have the lowest pCO_2, with climatological means (2014–2025) from 403 to 533 µatm across the EGSL. These values globally track annual atmospheric CO_2, which rose from ~398 µatm in 2014 to 427 µatm in 2025 (NOAA/GML, Lan and Keeling, last accessed in July 2026). Most surface waters fluctuate around atmospheric equilibrium, alternating between undersaturation and supersaturation relative to the atmosphere

as a result of seasonal and interannual variability in biological production, respiration, temperature, mixing, and air-sea CO_2 exchange (e.g., Dinauer and Mucci 2017, Mucci and Jutras 2026). Annual pCO_2 values increase with depth across all regions. At 100 m, climatological values range from ~550 µatm (Centre Gulf) to ~770 µatm (Estuary). At 200 m, all regions reach ~800–1200 µatm, with climatological hypercapnia (>1000 µatm) occurring in the Estuary and Northwest Gulf. The highest climatological pCO_2 values generally occur at 300 m, where all regions except the Centre Gulf exhibit hypercapnic conditions.

Temporal analysis shows that pCO_2 trends mirror pH_T patterns but with opposite direction, reflecting intensified carbon accumulation since 2020 (Figure 11). This mirroring is expected, as pCO_2 is derived from pH and other carbonate system parameters (TA in this document), underscoring the coupled nature of these changes across the EGSL. In the early years of the sampling record (2014–2019), waters at intermediate and deep layers (100 m to 300 m) exhibit anomalies dominated by below-normal values. From 2020 onward, above-normal anomalies become more frequent at these depths, indicating a shift toward higher pCO_2. In 2025, pCO_2 anomalies at 200 m in the Estuary and Northwest Gulf remained above normal, whereas most other regions exhibited a general shift to either near-normal or weakly below-normal conditions (Figure 11). Lowest regional near-bottom pCO_2 2025 values were found in Northumberland Strait and the Magdalen Shallows, with 615 µatm and 692 µatm, respectively. For 2025, the Estuary recorded the third-highest pCO_2 at 100 m and the second-highest at 200 m in the 2014–2025 time series, the latter tied with the 2023 annual average.

Spatial pCO_2 patterns in deep and near-bottom waters (Figure 13) are consistent with overall patterns of CSVI (Figure 6), DIC (Figure 8), and pH_T (Figure 12), with a distinctive channel-oriented gradient. The lowest climatological pCO_2 values at 300 m occur in Centre Gulf near Cabot Strait. At 200 m, they occur there as well, in addition to the head of Esquiman Channel in the Northeast Gulf. On the other end of the spectrum, the highest climatological pCO_2 spatial values are found in the Estuary and Northwest Gulf regions. This longitudinal gradient is particularly evident in the channel sections (Figure 14, Figure 15, and Figure 16) and highlights the influence of water-mass origin, circulation, residence time, and biogeochemical transformation on the accumulation of inorganic carbon in intermediate and deep waters.

Hypercapnic conditions in 2025 were observed at 200 m in the Estuary and Northwest Gulf, and at 300 m in the Estuary, Northwest Gulf and Northeast Gulf. Hypercapnia was also present in near-bottom waters of the Estuary and the Northwest Gulf, reflecting CO_2 accumulation along the deep waters of the Laurentian Channel. In the Estuary, more than half of the near-bottom waters deeper than 100 m have been hypercapnic ($pCO_2 \geq 1000$ µatm) since about 2014, with 2015 as the only exception. The proportion of hypercapnic near-bottom waters has generally risen over time, peaking in 2020 (82 %) and reaching roughly 75 % in 2025 (Figure 17). In the Gulf of St. Lawrence, hypercapnia remains more limited but has also increased over time: since 2020, more than 25 % of near-bottom waters deeper than 100 m have been hypercapnic, with a maximum in 2023 (43 %) followed by values near 25 % in 2024 and 2025 (Figure 17).

Along the Laurentian Channel, the upper boundary of hypercapnic waters shoaled slightly above 200 m in the climatology to ~150 m in 2025 (Figure 14). Hypercapnic waters also extended over ~500 km from the mouth of the channel toward Cabot Strait and their distribution closely mirrored the 30 % oxygen saturation contour shown in Figure 8 of Blais et al. (2026). Above-normal pCO_2 anomalies were evident along the Laurentian Channel transect in 2025, particularly within the upper 200 m, while deeper waters at the mouth of the Channel (Cabot

Strait) exhibited below-normal conditions, indicating a shift in the chemical signature of the source waters at depth. The Anticosti Channel showed a contraction of hypercapnic conditions, with both the vertical and horizontal extent of the threshold reduced in 2025 relative to the climatology (Figure 15). The 2025 anomaly patterns across the Anticosti Channel were broadly dominated by near-normal conditions between 50 m and ~200 m, while anomalies were mostly below normal at depths deeper than 200 m. Localized hypercapnic conditions were also found near the bottom in the Esquiman Channel with little variation between 2025 and the climatological period (Figure 16). In 2025, pCO_2 anomalies in the subsurface layers of the Esquiman Channel were generally near normal, particularly between 50 m and ~200 m, with below-normal conditions at depth (Figure 16).

Near-bottom waters of the EGSL show greater spatial heterogeneity in pCO_2 (Figure 13) reflecting a diverse near-seafloor environment shaped by both depth and proximity to coastal and shelf areas. Climatological values reveal a pronounced gradient, with the highest pCO_2 near the Laurentian Channel head and lower values, although still elevated, near the Anticosti and Esquiman Channel heads. Climatological partial pressures of CO_2 in shallow areas such as the Magdalen Shallows and Northumberland Strait largely remain lower due to stronger mixing and ventilation. In 2025, hypercapnic near-bottom waters extended farther eastward into the Northwest Gulf, indicating localized CO_2 accumulation consistent with the above-normal anomalies observed in this region. However, the near-bottom spatial anomaly map (Figure 13), shows a patchy distribution of mostly below-normal anomalies interspersed with localized near- and above-normal features. Some of the strongest above-normal anomalies occurred in the western portion of Magdalen Shallows including Chaleur Bay, emphasizing the importance of regional and local processes in shaping near-bottom carbonate chemistry.

3.4 INDICES OF BIOGENIC CALCIUM CARBONATE FORMATION AND DISSOLUTION

3.4.1 High-frequency monitoring station

Surface waters are generally supersaturated during the summer months with respect to climatological aragonite ($\Omega_A \geq 1$), whereas the shoulder seasons, spring and fall into winter, show periods of surface undersaturation, as indicated by the upward intrusion of the $\Omega_A = 1$ contour. Climatological depth contours of Ω_A suggest that intermediate to near-bottom waters (below ~100 m) at Rimouski station remain chronically undersaturated with respect to aragonite throughout the year, posing persistent challenges for calcifying organisms inhabiting these deeper layers.

The climatological distribution of Ω_C at Rimouski station shows a broadly similar structure to Ω_A, but with key differences in magnitude and depth of undersaturation (Figure 18). Surface waters remain consistently supersaturated ($\Omega_C \geq 1$) throughout the year, with values typically exceeding 1.5. Unlike Ω_A, climatological average values of Ω_C do not fall below 1 in the upper 100 m. Persistent undersaturation occurs only below ~200 m, reflecting calcite's greater stability due to its lower solubility (Mucci 1983) and more compact crystal structure (Morse and Mackenzie 1990). As a result, Ω_C remains higher than Ω_A throughout much of the water column, and the depth of calcite undersaturation occurs deeper than that of aragonite.
At Rimouski station, climatological SIR values in the upper 100 m typically show high values (>0.155 mol μmol^{-1}) from April through December, with the highest values in June–July in surface waters (>0.220 mol μmol^{-1}, Figure 18), indicating favourable conditions for calcification. Values of SIR decrease with depth, reaching ~0.100–0.155 mol μmol^{-1} between 100 and 200 m

as [H^+] rises with CO_2 accumulation. Below ~200 m, values fall under 0.100 mol µmol^{-1}, corresponding to the biological reference threshold adopted in this report (Thomsen et al. 2015).

In 2025, values of all three $CaCO_3$-related indices (Ω_A, Ω_C, SIR) showed seasonal patterns broadly consistent with those observed for other carbonate-system parameters at Rimouski station. From late April through July, anomalies were predominantly below normal to near normal throughout most of the water column, indicating reduced saturation states and lower substrate–inhibitor ratios relative to climatological expectations. Beginning in August, these anomalies shifted toward predominantly near-normal conditions, with the remainder of the sampling period showing less deviation from the climatological envelope. A shoaling of key thresholds (Ω_C = 1 and SIR = 0.100 mol µmol^{-1}) was evident in spring through early fall, with the depth ranges associated with lower carbonate system favourability shifting upward into shallower intermediate waters linked to the CIL (<100 m–150 m), with occasional shallow features extending into the upper ~50 m. These thresholds subsequently deepened toward their climatological positions later in the season. For aragonite, the lowest saturation values ($\Omega_A \approx 0.50–0.65$) also extended upward into the upper ~50 m during summer, indicating a temporary expansion of low-Ω_A conditions into near-surface waters. Taken together, these patterns suggest that $CaCO_3$-related conditions at Rimouski station in 2025, while still relatively challenging, more closely resembled the 2014–2025 climatological conditions particularly during the second half of the sampling period.

3.4.2 EGSL regions

Across the EGSL, climatological Ω_A, Ω_C (Figure 19), and SIR (Figure 20) consistently decrease with depth, reflecting progressively less favourable conditions for $CaCO_3$ formation and preservation. Surface waters of the Northwest Gulf and the Estuary, including Rimouski station, fall below the biological threshold of Ω_A = 1.5, a benchmark associated with increasingly less favourable conditions for some calcifying organisms (Figure 19). All other EGSL regions maintain surface Ω_A climatological averages above this limit of 1.5. At 50 m, the Ω_A = 1 critical threshold is crossed in the Estuary and approaches this value in the Magdalen Shallows (1.02) and Northwest Gulf (1.09). At 200 m, 300 m, and in near-bottom waters, Ω_A climatological averages are consistently ≤ 1 across all EGSL regions, except for the shallow Northumberland Strait. Calcite exhibits a similar depth-dependent pattern, but the corresponding thresholds occur at greater depths because of its lower solubility relative to aragonite (Figure 19). Unlike aragonite, surface and 50 m waters remain above the Ω_C = 1.5 biological benchmark across all EGSL regions, but this limit is crossed at 100 m in all regions except the Centre Gulf and Northeast Gulf. Climatological Ω_C falls below the saturation threshold of 1 at 200 m and 300 m in the Estuary, whereas all other EGSL regions maintain supersaturation ($\Omega_C \geq 1$) throughout the water column during the reference period (2014–2025). Climatological SIR follows the same vertical pattern, with SIR values ≤ 0.100 mol µmol^{-1} emerging at 200 m, 300 m, and near-bottom in the Estuary (Figure 20). Other EGSL regions also show depth-related reductions in climatological SIR but remain above the 0.100 benchmark.

The anomaly scorecards for subsurface waters below 100 m and near-bottom layers reveal two broad temporal regimes across the EGSL: ~2014–2019 and ~2020–2025 (Figure 19 and Figure 20). During the earlier period, anomalies are predominantly above- to near-normal. Beginning around 2020, below-normal Ω_A, Ω_C, and SIR anomalies become increasingly frequent across several regions and depth layers. This shift is particularly evident at 100 and 200 m, where anomalies for all three indices have been predominantly below normal since 2020. Shallower regions (Magdalen Shallows and Northumberland Strait) exhibit greater interannual variability in anomalies and less coherent temporal patterns among depth layers. In

2025, Ω_A, Ω_C, and SIR conditions at 300 m and in near-bottom waters improved relative to recent years across several regions, with anomalies shifting toward predominantly near-normal to above-normal values. However, in the Estuary, despite above-normal anomalies at these depths, values remained below or at the critical thresholds for these calcium carbonate indices.

The vertical perspectives presented in Figure 19 and Figure 20 help frame the spatial imprint of carbonate mineral stability and calcification potential across key depth layers (Figure 21, Figure 22, Figure 23). At 200 m, climatological Ω_A values are below 1 in most regions, with the Estuary and Northwest Gulf most heavily undersaturated (Figure 21). In 2025, the spatial extent of Ω_A undersaturation at 200 m near Cabot Strait showed no expansion, as indicated by the stable position of the white threshold line, and near-normal anomalies in the Centre Gulf. In contrast, undersaturation intensified in the Estuary and in parts of the Northwest Gulf, as reflected by the below-normal anomalies. Patterns of climatological Ω_C (Figure 22) differ in magnitude but follow the same spatial progression as Ω_A: highest supersaturation near Cabot Strait and lowest in the Estuary and Northwest Gulf. In 2025, the Ω_C undersaturation contour at 200 m expanded eastward into the Northwest Gulf, as shown by the displacement of the white boundary line. This pattern is consistent with the below-normal anomalies in these regions, whereas other areas with 200 m waters were characterized by mostly near-normal conditions. The climatological spatial patterns in SIR values at 200 m indicate favourable conditions (>0.100) in most areas, highest near Cabot Strait, lowest in the Estuary and Northwest Gulf (Figure 23). In 2025, the SIR threshold contour at 200 m also expanded eastward in the Northwest Gulf.

At 300 m, climatological Ω_A patterns show widespread undersaturation across the EGSL regions (Figure 21). In 2025, Ω_A conditions at 300 m improved relative to the climatology and the undersaturation contour line receded into the Centre Gulf, giving way to predominantly above-normal anomalies in this region and across other areas. Spatial climatological Ω_C patterns mirror Ω_A but with higher absolute values (Figure 22). The climatology indicates widespread supersaturation, with strongest values in the Centre Gulf and Northeast Gulf and weakest in the Estuary and Northwest Gulf. In 2025, Ω_C anomalies at 300 m similarly indicated relative improvement, with predominantly near- to above-normal saturation states. Although the Ω_C undersaturation threshold is not visible in the climatology at 300 m because it lies within a data-gap region, the contour line receded into the Estuary in 2025. Climatological SIR values remain above 0.100 mol μmol^{-1} in most areas, with the highest values near Cabot Strait, and the lowest values in the Estuary and Northwest Gulf (Figure 23). However, localized zones of SIR ≤ 0.100 mol μmol^{-1} are present near the head of the Laurentian Channel in the Estuary. In 2025, near- to above-normal SIR anomalies predominated at 300 m in deep-water regions indicating a relative improvement in global conditions at this depth.

At near-bottom depths, carbonate indicators predominantly show irregular spatial patterns shaped by bathymetry and coastal proximity. Climatological Ω_A values are below 1 in many regions including the Estuary, Northwest Gulf and parts of the Magdalen Shallows and Northeast Gulf (Figure 21). Highest near-bottom Ω_A values are found in shallow waters of the Northumberland Strait and near the Magdalen Islands. In 2025, Ω_A anomalies were spatially heterogeneous with notable areas of relative improvement indicated by above-normal anomalies such as in Cabot Strait, for example. Climatological Ω_C (Figure 22) and SIR (Figure 23) show similar spatial patterns, with critical threshold crossings ($\Omega_C < 1$; SIR < 0.100) concentrated in near-bottom waters of the deep channel in the Estuary. In 2025, the Ω_C and SIR threshold zones showed a reduced spatial extent in the Estuary, although the Ω_C contour is less clearly resolved in the near-bottom maps. Across all three metrics (Ω_A, Ω_C, and SIR), 2025 bottom-layer anomalies formed a fragmented pattern of below- to near- to above-normal conditions.

4. DISCUSSION

4.1 SURFACE TO SEAFLOOR: ENVIRONMENTAL GRADIENTS IN CO_2-DRIVEN CONDITIONS

Unlike the open ocean, where acidification is primarily driven by atmospheric CO_2 uptake, estuaries and semi-enclosed marine environments are influenced by a broader set of interacting physical, biological, and biogeochemical processes (Cai et al. 2011, 2021, Mucci et al. 2011, 2017, Li et al. 2023). As a result, regional drivers can amplify, modulate, or mask the effects of increasing atmospheric CO_2 on carbonate-system dynamics.

The EGSL marine system exemplifies these dynamics with its structure dominated by the Laurentian Channel, a submarine valley 250–500 m deep and 1240 km long that extends from the continental shelf to the Saguenay Fjord confluence. Estuarine circulation prevails, with buoyant surface waters flowing seaward and dense deep waters moving landward, driven by freshwater runoff from the Great Lakes and rivers draining Northern Quebec and Labrador. Freshwater inputs strongly influence surface carbonate variability and buffering capacity (Mucci et al. 2011, Mucci and Jutras 2026). Notably, these inputs may supply dissolved organic matter that contributes to measured total alkalinity potentially affecting interpretations of buffering capacity in near-surface waters receiving substantial terrestrial inputs (Hu 2020, Kerr et al. 2021). Seasonal changes in temperature and salinity under atmospheric forcing further shape stratification, mixing, and nutrient supply, which in turn affect ecosystem productivity and CO_2-carbonate system fluctuations (Gilbert and Pettigrew 1997, Galbraith 2006, Lavoie et al. 2020, 2021, Gibb et al. 2023, Blais et al. 2026, Galbraith et al. 2026b). Warming trends in the Gulf of St. Lawrence (Galbraith et al. 2026b) may further modulate these processes through temperature-dependent effects on stratification, CO_2 solubility, carbonate speciation, and oxygen availability (Cai et al. 2021). Together, these physical and biogeochemical drivers generate pronounced vertical gradients in carbonate-system conditions throughout the EGSL, making a depth-resolved perspective essential for understanding regional acidification patterns and organism exposure to changing chemical environments (IPBES 2019; Findlay et al. 2025).

The vertical structure of the carbonate system in the EGSL reveals striking contrasts. In 2025, surface waters maintained broadly favourable chemical conditions, while deeper layers exhibited more vulnerability. This differentiation reflects in large part differences in ventilation and air–sea exchange shaped by the estuarine circulation, with surface layers strongly coupled to the atmosphere, while deep waters remain largely isolated. The Laurentian Channel bottom waters consist of Labrador Current waters (LCW) and North Atlantic Central waters (NACW), with proportions varying over decades (Bugden 1991, Gilbert et al. 2005, Jutras et al. 2023a). Bottom waters in the Laurentian Channel are already preconditioned by anthropogenic CO_2 absorbed during their last surface residence (Gattuso et al. 1998, Orr et al. 2005, Gattuso and Hansson 2020, Mucci et al. 2011). Over the past century, this baseline has been compounded by shifts in mixing ratios between LCW and NACW entering the channel (Gilbert et al. 2005, Jutras et al. 2023a), along with rising bottom-water temperatures (Galbraith et al. 2026b) and microbial degradation of organic matter (Thibodeau et al. 2006, 2010, Genovesi et al. 2011, Jutras et al. 2023b, Nesbitt et al. 2025). These processes can drive gradual deoxygenation and intensify acidification (Cai et al. 2011, Gehlen et al. 2011, Mucci et al. 2011, Mucci et al. 2017, Gibb et al. 2023, Blais et al. 2026, Galbraith et al. 2026a). To reflect these different regimes, the following discussion is organized into two parts: surface waters in contact with, and responsive to the atmosphere, and deeper subsurface layers below the CIL, where carbonate dynamics are shaped by longer-term physical and biogeochemical processes.

4.1.1 Surface and upper waters: atmosphere-influenced and CIL-conditioned carbonate dynamics

This section focuses on the surface and upper waters of the EGSL, including the seasonally variable surface mixed layer and the CIL. These layers remain strongly influenced by atmospheric forcing, freshwater inputs, biological production, and air-sea CO_2 exchange, resulting in greater seasonal and interannual carbonate-system variability than is observed at depth (Mucci et al. 2011, Gibb et al. 2023, Mucci and Jutras 2026). Phytoplankton blooms, stratification, ice conditions, and river discharge can substantially modify surface carbonate chemistry and buffering capacity from year to year, often masking or amplifying underlying acidification trends (Mucci et al. 2011; Lavoie et al. 2020, 2021 ; Gibb et al. 2023; Hall et al. 2023). Consequently, annual surface and upper water anomalies should be interpreted cautiously, as local environmental drivers, interannual variability, and episodic events can substantially influence carbonate-system conditions and obscure longer-term trends.

Surface carbonate system conditions across the EGSL in 2025 were overall more favourable, with most regions showing either near-normal anomalies or subdued improvements compared to the 2014–2025 climatology. Surface layers in the Northwest Gulf, Northeast Gulf, Centre Gulf, and Northumberland Strait were characterized by more favourable or near-normal conditions, with only limited departures from the climatology, such as above-normal DIC in these regions. The Magdalen Shallows also exhibited predominantly near-normal surface conditions, with only pCO_2, pH_T, and SIR exhibiting less favourable anomalies compared to the climatology. In contrast, the Estuary, including Rimouski station, remained the principal exception to this basin-wide pattern, showing mostly reduced carbonate-system resilience at the surface despite above-normal TA.

At the 50 m and 100 m depths, carbonate system conditions across the EGSL in 2025 were also broadly characterized by near-normal or more favourable anomalies against the backdrop of the 2014–2025 climatology. At 50 m, the Centre Gulf, Northeast Gulf, Estuary (including Rimouski station), and Magdalen Shallows displayed uniformly more favourable or near-normal anomalies, while the Northwest Gulf also aligned with this pattern aside from an isolated exception of below-normal TA. At 100 m, signals remained dominated by improved or near-normal anomalies across most deep regions, with some exceptions. The Northwest Gulf, Northeast Gulf, and Magdalen Shallows showed either improvements or near-normal conditions in all carbonate-system conditions with the exception of below-normal TA in all of these regions. On the other hand, the Centre Gulf and Estuary were characterized by less favourable carbonate chemistry indicators relative to the climatology, apart from near-normal TA in these two regions. The less favourable 100 m conditions seen in the Estuary did not occur at Rimouski station, which showed near-normal annual anomalies for all indicators aside from below-normal TA. Taken together, the upper 100 m of the EGSL exhibited a broad tendency toward near-normal or improved carbonate system conditions in 2025 compared to the climatology, with relatively few departures from this general pattern.

4.1.2 Deeper subsurface waters: from channel depths to shelf bottoms

This section focuses on the deeper layers of the EGSL intersected by the Laurentian, Esquiman, and Anticosti Channels. These waters originate near the continental shelf break and circulate landward with limited exchange with upper layers (Galbraith et al. 2026b). Regional carbonate-system gradients reflect this deep-water transport along the channels: marine waters entering through Cabot Strait progressively accumulate respiration-derived CO_2 as they

progress landward. Strong density stratification acts as a physical barrier, trapping carbon-rich waters, and intensifying acidification toward channel heads. This connectivity is further modulated by decadal shifts in LCW and NACW relative proportions, influencing carbonate system parameters and driving spatial variability in acidification exposure across the EGSL. Compared to surface layers, these deeper waters exhibit less pronounced seasonal variability, providing a useful baseline for detecting emerging trends. Variability at depth more strongly reflects persistent physical and biogeochemical processes rather than episodic events, offering a stronger basis for assessing sustained carbonate system constraints. Beyond these deep layers, bottom waters span a wide bathymetric range, where nearshore and sediment–water interactions, and variable mixing and ventilation further shape carbonate chemistry.

Among the deeper layers, the 200 m layer in 2025 continues to stand out as a zone of greater carbonate-system vulnerability in the EGSL. At this depth, the Estuary, including Rimouski station, and the Northwest Gulf exhibited less favourable anomalies relative to the climatology for every indicator except TA, which remained near normal. The Northeast Gulf showed a similar pattern of reduced carbonate-system resilience at this depth, although DIC, pCO_2, pH_T, and SIR remained near normal, indicating a slightly moderated response relative to other deep regions. In contrast, the Centre Gulf exhibited predominantly near-normal conditions at 200 m, with TA as the main exception, showing a below-normal anomaly. Collectively, these patterns identify the 200 m layer as the depth at which unfavourable carbonate-system anomalies were most consistently expressed across the deep EGSL regions in 2025.

At 300 m and in near-bottom waters, carbonate-system conditions across the EGSL in 2025 were broadly characterized by near-normal anomalies or shifted toward more favourable conditions relative to the climatology, indicating a partial relief from the more challenging anomalies observed at 200 m. The Northeast Gulf was an exception to this broad pattern with most indicators shifting toward less favourable conditions relative to the climatology, while TA and pCO_2 remained near normal.

This overall pattern extended to the near-bottom layers of the deep regions, where the Estuary, the Northwest Gulf, the Northeast Gulf, and the Centre Gulf all exhibited mostly near-normal or improved carbonate-system indicators, with modest deviations confined to TA, DIC, and pCO_2, reflecting slight shifts toward less favourable conditions for these indicators. Near-bottom waters in the shallower regions were similarly dominated by near-normal anomalies. Conditions in the Magdalen Shallows were entirely near normal across all indicators, while Northumberland Strait was also predominantly near normal aside from above-normal TA counteracting an above-normal DIC anomaly. Near-bottom patterns in 2025 reflect how local physical structure and benthic processes may modulate carbonate conditions, with residence time, remineralization, and ventilation varying across the channel and shelf. Freshwater and terrestrial inputs further shape shelf variability. These depth-specific behaviours, consistent with other marine systems (Li et al. 2022), underscore the importance of vertically resolved assessments of CO_2-driven stress in the EGSL.

Taken together, the 2025 observations reveal a broad basin-wide tendency toward more favourable deep-water conditions below 200 m compared with the 2020–2024 period, while near-bottom waters in shallower regions show correspondingly near-normal anomalies within their limited depth range. Despite these subdued anomalies, several 2025 annual carbonate system values remain elevated in absolute terms, suggesting that CO_2-driven pressures persist even where interannual signals appear muted. In 2025, a notable contrast emerges between the deeper layers of the deep regions and the 200 m depth, which continued to be the main depth of carbonate-system pressure in several areas of the EGSL. The similar qualitative patterns

between the physical conditions (Galbraith et al. 2026b), oxygenation (Blais et al. 2026), and carbonate system suggest that variations in source-water composition and ventilation remain the major controls on deep-water carbonate chemistry in the EGSL.

4.2 PERSPECTIVES ON EGSL REGIONAL VULNERABILITY TO CO_2-DRIVEN STRESSORS

The following section shifts the focus from individual carbonate-system indicators and annual anomaly patterns to a tiered assessment of regional vulnerability, examining how CO_2-driven stressors manifest, co-occur, and accumulate across regions and depths of the EGSL in 2025. This framing highlights the spatial and vertical gradients of exposure, and identifies areas where multiple carbonate-system stressors may pose increasing challenges to ecosystem resilience.

Despite substantial natural variability in carbonate chemistry across the EGSL, annual mean conditions in 2025 reveal a pronounced regional and vertical gradient in the number of CO_2-driven stressor thresholds reached or exceeded (Figure 24). Complementary cumulative frequencies of observations reaching or exceeding these same thresholds provide a longer-term perspective on how frequently potentially stressful conditions have occurred across regions and depths during the 2014–2025 period (Figure 25). The combined occurrence of multiple thresholds provides a diagnostic measure of relative exposure to acidification and other CO_2-driven stressors. Thresholds are used here not as absolute limits, but as ecologically meaningful benchmarks translating complex chemical variability into biologically relevant risk indicators. This threshold-based approach aligns with recent planetary boundary assessments and ecological risk frameworks (Cornwall et al. 2024, Findlay et al. 2025, Sakschewski et al. 2025), which emphasize the practical value of clear inflection points for guiding management decisions and evaluating systemic vulnerability.

At one end of the spectrum, the Estuary emerges as a zone of extreme vulnerability, where all five CO_2-driven stressor thresholds are reached or exceeded at depth (Figure 24 and Figure 25). Episodic aragonite undersaturation occurs at the surface in the Estuary (Figure 25) however annual-average conditions indicate that aragonite undersaturation is more established from 50 m and deeper (Figure 24). While episodic observations also show occasional threshold attainment for CSVI, pCO_2, calcite undersaturation, and SIR from the surface to 100 m, these events remain infrequent compared to the more persistent signals emerging at depth (Figure 25).

The 200 m depth represents a critical zone, where annual average values for all five CO_2-driven stressor thresholds are simultaneously reached or exceeded in the Estuary (Figure 24). These conditions reflect a lockstep intensification of hypercapnia, impaired buffering capacity, undersaturation of the carbonate minerals aragonite and calcite, and low SIR conditions. They also coincide with indicators of organic matter degradation in deeper layers, aligning with recent observations of increased deoxygenation at depth reported by Blais et al. (2026) particularly since ca. 2020. Together, such stressors may impose multiple overlapping physiological constraints on CO_2-sensitive organisms.

Moving eastward, the Northwest Gulf presents an intermediate level of vulnerability (Figure 24 and Figure 25). Within the upper 100 m, threshold-level observations for CSVI, pCO_2, Ω_A, Ω_C, and SIR occur sporadically and generally represent only less than 25 % of observations, with aragonite undersaturation being the principal exception (Figure 25). Annually averaged aragonite undersaturation appears around 100 m, but vulnerability intensifies at 200 m, where four stressor thresholds are reached/exceeded, including hypercapnia and combined stressors associated with less favourable conditions for calcium carbonate formation and preservation (Figure 24). At 300 m and in near-bottom waters, the comparatively low frequency of CSVI

threshold exceedance suggests greater buffering capacity than in the Estuary, moderating overall CO_2-driven vulnerability despite the persistence of other stressors.

The Northeast Gulf and Centre Gulf exhibit relatively lower vulnerability compared to other deep regions, with only one or two stressor thresholds typically reached or exceeded on average in 2025 (Figure 24). Notably, the Northeast Gulf is the only region where CSVI and calcite undersaturation thresholds are never reached (0 % of observations) from the surface to near-bottom waters throughout the 2014–2025 period (Figure 25). Nevertheless, aragonite undersaturation extends from approximately 100 m to near-bottom waters, and annual mean hypercapnic conditions occurred at 300 m in 2025 (Figure 24), indicating that deep-water vulnerability remains significant. The Centre Gulf shows a more limited stressor profile: while aragonite undersaturation is present annually from 100 m down to near-bottom waters, pCO_2 levels remain below the hypercapnia threshold in 2025, indicating comparatively lower vulnerability. Figure 25 shows that low-frequency threshold-level observations (1–25 %) have become somewhat more common during the latter half of the observational record in waters 200 m and deeper of the Centre Gulf.

The Magdalen Shallows and Northumberland Strait differ fundamentally from the deeper EGSL regions because their shallower bathymetry excludes the deep-water masses occupying the Laurentian, Anticosti, and Esquiman Channels. Their deepest waters remain within the more dynamic upper ocean, where mixing and ventilation are comparatively stronger. As a result, exposure to persistent CO_2-driven stressors is limited; in 2025, the only threshold reached on an annual basis is aragonite undersaturation in the Magdalen Shallows, occurring near ~100 m and in near-bottom waters (Figure 24). Low-frequency threshold-level observations (1–25 %) do occur in both shallow regions, particularly in the Magdalen Shallows, and have become somewhat more common in these waters during the latter half of the record (Figure 25). However, these signals do not display a consistent intensification in their percentage of occurrence. Consequently, the Magdalen Shallows and Northumberland Strait represent zones of low multi-stressor exposure, with relatively buffered carbonate conditions.

This report establishes that enhanced ocean acidification, documented in other regions of the world's oceans (Cai et al. 2011, Lauvset et al. 2020, Fassbender et al. 2023), is also occurring in the deep waters of the EGSL. Long residence times, strong stratification, limited ventilation, and organic matter remineralization promote the accumulation of respiratory CO_2, creating low-pH and hypercapnic conditions below the pycnocline. These stressor regimes have intensified since 2020, generating pronounced vertical and regional gradients that may increase biological vulnerability. Although the drivers in estuarine and marginal seas differ from those in the open ocean, the outcome is similar: intensification of acidification below the pycnocline. In the global ocean, this process is primarily driven by the downward transport of anthropogenic dissolved inorganic carbon and respiration-derived CO_2 (Cai et al. 2011, Lauvset et al. 2020, Fassbender et al. 2023). Globally, approximately 60 % of subsurface waters from 50 m down to 200 m had entered the uncertainty range of the planetary boundary for ocean acidification by 2020, compared to 40 % of surface waters, further emphasizing the importance of subsurface acidification (Findlay et al. 2025). Both regional and global evidence confirm that enhanced acidification below the pycnocline is a defining feature of the changing carbonate system.

In the EGSL, spatial and vertical gradients in CO_2-driven stressors may shape exposure patterns and influence biological vulnerability. These gradients complicate efforts to evaluate ecosystem resilience and predict species-level responses because physical, chemical, and biological processes interact across scales. Biological vulnerability spans multiple habitats, including benthic communities that include a diverse array of calcifying organisms, mollusks,

bivalves, benthic foraminifera, crustaceans, echinoderms, cnidarians, and gastropods, that play key ecological roles and contribute to biogeochemical cycling (Steinhart 2023, Chamberland et al. 2025). Deeper pelagic layers support midwater and vertically migrating organisms, including invertebrates and numerous fish species, ranging from pelagic to demersal taxa, which sustain trophic connectivity, carbon flux, and, together with benthic taxa, underpin regional fisheries of commercial importance (Nozères et al. 2010, Bourdages et al. 2017, Bernier et al. 2023). Pelagic larval phases of many species link surface, midwater, and benthic habitats, reinforcing ecosystem connectivity (e.g., Ouellet and Sainte-Marie 2018). This network's resilience depends partly on the integrity of deep-water habitats and the cohesion of carbonate system dynamics throughout the EGSL.

Ocean acidification, hypercapnia, hypoxia, and warming can interact in complex and non-linear ways to affect marine organisms and ecosystems (Small et al. 2020, Collins et al. 2021, Huo et al. 2021, 2023). Carbonate undersaturation can reduce net calcification, with early life stages of many calcifying taxa being particularly sensitive (Waldbusser and Salisbury 2014, Small et al. 2015, 2016, Dodd et al. 2020, Stiasny et al. 2021, Figuerola et al. 2022). Non-calcifying organisms may also experience physiological effects under hypercapnic conditions through disruptions to acid–base regulation and associated energetic costs (Michaelidis et al. 2007, Spicer and Morley 2022). Responses vary substantially among taxa and populations according to physiological plasticity, genetic diversity, environmental history, and local adaptation (Gaitán-Espitia et al. 2017a, 2017b, 2023, Alter et al. 2024). Consequently, chemical thresholds alone cannot predict ecological responses, but they provide a useful framework for identifying habitats where multiple stressors increasingly overlap and where biological vulnerability warrants closer investigation.

Building on this recognition, the findings presented in this report highlight the crucial role of long-term, multi-decadal observational programs for advancing our understanding of ocean acidification and other related CO_2-driven stressors. Such programs are indispensable for disentangling natural variability from anthropogenic trends, a priority consistently reaffirmed by the international scientific community (Bates et al. 2014, Hassoun et al. 2025). Sustained monitoring is also essential for ecosystem-based fisheries management, providing the foundational data needed to assess exposure, evaluate vulnerability, and develop adaptive management strategies (e.g., Wright-Fairbanks et al. 2025). Deepening our grasp of the ecological consequences of OA and other CO_2-driven conditions requires high-resolution observations, experimental validation, and predictive modelling, supported by multidisciplinary collaboration across marine sciences.

5. KEY FINDINGS

This report documents acidification and CO_2-driven conditions observed in the Estuary and Gulf of St. Lawrence during 2025, in the context of ongoing variability and longer-term changes in the region's physical and biological environment. Surface and upper mixed layer carbonate chemistry is highly variable in the EGSL, shaped by short-term physical, chemical, and biological processes. Because surface water annual anomalies largely reflect local and episodic variability, reliable trend detection in upper layers of the water column will require longer-term records and contextualization; therefore, key findings presented below focus on subsurface and deep-water conditions where signals are more persistent.

- In 2025, carbonate-system conditions at Rimouski station showed a distinct two-phase seasonal pattern: an early-season intensification of acidification and threshold shoaling (CSVI,

pCO_2, Ω_A, Ω_C, SIR) in intermediate to deep waters, followed by late-season moderation toward climatological conditions. Hypercapnic conditions persisted throughout the year from ~200 m to the bottom.

- Buffering capacity, as indicated by the carbonate system vulnerability index (CSVI), was near-normal to below-normal at 100 m and 200 m, showed mixed anomalies at 300 m, and was mostly normal in near-bottom waters across the EGSL.

    - At 200 m, the Estuary (including Rimouski station) registered the third-lowest CSVI average values in the 2014–2025 record, while the Northwest Gulf showed the second-lowest values, tied with 2024.

- Subsurface pH_T anomalies were mixed at 100 m and 300 m, were broadly near-normal in near-bottom waters, and at 200 m displayed below-normal values in the Estuary and Northwest Gulf contrasted with near-normal conditions in the Centre and Northeast Gulf.

    - At 200 m, 2025 registered the second-lowest annual pH_T values in the 2014–2025 record for the Estuary, Northwest Gulf and third-lowest pH_T in the Northeast Gulf. These record low values have also occurred repeatedly since 2020, indicating a persistence of similarly acidified conditions.

- Subsurface pCO_2 anomalies displayed mixed patterns at 100 m and 300 m, remained broadly normal in near-bottom waters, and were above normal at 200 m in the Estuary and Northwest Gulf while remaining near normal in the Centre and Northeast Gulf.

    - Annually averaged hypercapnic conditions were found at 200 m, 300 m, and in near-bottom waters in the Estuary and Northwest Gulf and at 300 m in the Northeast Gulf.

    - Time-series records show the third-highest pCO_2 at 100 m and the second-highest at 200 m (tied with 2023) in the Estuary.

- Subsurface aragonite saturation state (Ω_A) anomalies showed mostly near-normal to below-normal conditions at 100 m and 200 m, and mostly near-normal to above-normal conditions at 300 m and in near-bottom waters.

    - Annually averaged aragonite undersaturation occurred in all regions at near-bottom depths and at 100 m and deeper (where such depths exist), except in the Northeast Gulf at 100 m ($\Omega_A = 1$) and in near-bottom waters of the Northumberland Strait ($\Omega_A = 1.19$).

    - For 2025, Ω_A ranked third-lowest at 100 m in the Centre Gulf and second-lowest at 200 m in the Estuary and Northwest Gulf, though these values have also occurred repeatedly in multiple years since 2020, indicating a persistence of unfavourable conditions.

- Regional and depth-dependent subsurface anomalies in calcite saturation state (Ω_C) across the EGSL exhibited spatial patterns that mirror those observed for Ω_A.

    - Calcite undersaturation was present at 200 m in the Estuary and Northwest Gulf and at 300 m in the Estuary, with near-bottom waters in the Estuary lying on the cusp of annually averaged undersaturation ($\Omega_C = 1$).

    - In 2025, Ω_C in the Estuary ranked third-lowest at 100 m and second-lowest at 200 m (both tied with 2023). The Centre Gulf showed the third-lowest value at 100 m (tied with 2020), and Rimouski station the third-lowest at 200 m (tied with 2020).

- Subsurface substrate-inhibitor ratio (SIR) anomalies displayed mixed patterns at 100 m and 300 m, were below normal to near-normal at 200 m, and were near-normal to above normal in near-bottom waters.

    - Annual 2025 values of SIR were below the threshold of 0.100 in the Estuary (at 200 m, 300 m, and bottom) and in the Northwest Gulf (at 300 m).

    - For 2025, SIR ranked third-lowest at 100 m and second-lowest at 200 m in the Estuary (both records matching 2023), while the Northwest Gulf recorded its third-lowest value at 200 m.

- Since 2020 and continuing in 2025, the 200 m depth stands out as a zone of generally sustained below-normal conditions in CSVI, pH_T, Ω_A, Ω_C, and SIR, alongside above-normal levels of pCO_2 and DIC, marking it as a key zone of carbonate system vulnerability particularly in the Estuary and the Northwest Gulf.

- A regional gradient in annual average cumulative CO_2-driven stressor threshold attainment was present across the EGSL in 2025:

    - The Estuary showed the most severe multi-stressor vulnerability from 200 m to the bottom, where all five thresholds, CSVI, pCO_2, Ω_A, Ω_C, and SIR, were reached or exceeded, with annual aragonite undersaturation extending as shallow as 50 m.

    - The Northwest Gulf exhibited high annual vulnerability, particularly at 200 m, where four thresholds, pCO_2, Ω_A, Ω_C, and SIR, were reached or crossed.

    - The Northeast Gulf showed moderate annual vulnerability, with hypercapnia and aragonite undersaturation present at 300 m.

    - The Centre Gulf and Magdalen Shallows displayed annual vulnerability but remained comparatively less affected overall; however, annual aragonite undersaturation was present in near-bottom waters and at depths of 100 m and deeper (where such depths occur).

    - The Northumberland Strait experienced episodic, low-frequency attainment of the aragonite undersaturation threshold in 2025, but annual averages did not indicate sustained vulnerability, and the region remained comparatively less affected over the year.

ACKNOWLEDGEMENTS

The monitoring of data presented here is made possible thanks to the dedicated commitment of the employees participating in the Atlantic Zone Monitoring Program and the Aquatic Climate Change Adaptation Services Program of DFO.

Rimouski station Monitoring
David Leblanc, Félix St-Pierre, Michel Rousseau, Anthony Ouellet, Nicolas Coulombe, Guillaume Mercier, Myranda Blouin, Sylvain Dubé, Bruno St-Denis, Geneviève Perrin, and the Canadian Coast Guard ship workshop crew.
Shediac Valley Monitoring Station
Quebec Region AZMP surveys; Renée Allain, Lindsay Beazley, François Turcotte, François-Étienne Sylvain, Stéphanie Ratelle, Félix St-Pierre, and Sylvain Dubé.
June AZMP Survey
David Leblanc, Véronique Desborbes, Guillaume Mercier, Myranda Blouin, Hélèna Talbot, Talia Koll-Egyed, Jean-Luc Shaw; officers and crew of the CCGS Capt. Jacques Cartier.
June Mackerel Egg Survey
Caroline Lehoux, Guillaume Mercier, Laurence Lévesque, Geneviève Perrin, Mélanie Boudreau, Anthony Ouellet ; officers and crew of the CCGS Capt. Jacques Cartier.
August Ecosystemic Survey
Guillaume Mercier, Myranda Blouin, Bruno St-Denis; officers and crew of the CCGS Cabot.
September Ecosystem Survey (Gulf and Maritimes Regions)
Pablo Vergara, Quentin Stoyel, Adam Drozdowski, and David Fishman (survey operations).
October–November AZMP Survey
David Leblanc, Caroline Lafleur, Mélanie Boudreau, Marie-Pier Boulanger, Hélèna Talbot, Anthony Ouellet, Sylvain Dubé ; officers and crew of the Coriolis II.
Data Management
Marie-Noëlle Bourrassa, Caroline Lafleur, and Hélèna Talbot.

We warmly thank Claude Potvin for his preparation, analysis, and calibration of the CO_2-carbonate system data, and acknowledge with gratitude his many years of dedicated service at DFO. We are grateful to Carrie-Ellen Gabriel and Daniel Small for reviewing the manuscript and providing insightful comments, and to Jean-Luc Shaw as the technical report editor.

REFERENCES CITED

Allemand, D., Ferrier-Pagés, C., Furla, P., Houlbrèque, F., Puverel, S., Reynaud, S., Tambutté, É., Tambutté, S., and Zoccola, D. 2004. Biomineralisation in reef-building corals: from molecular mechanisms to environmental control. C. R. Palevol 3:453–467. https://doi.org/10.1016/j.crpv.2004.07.011

Alter, K., Jacquemont, J., Claudet, J., Lattuca, M.E., Barrantes, M.E., Marras, S., Manríquez, P.H., González, C.P., Fernández, D.A., Peck, M.A., Cattano, C., Milazzo, M., Mark, F.C., and Domenici, P. 2024. Hidden impacts of ocean warming and acidification on biological responses of marine animals revealed through meta-analysis. Nat. Commun. 15:2885. https://doi.org/10.1038/s41467-024-47064-3

Arroyo, M.C., Fassbender, A.J., Carter, B.R., Edwards, C.A., Fiechter, J., Norgaard, A., and Feely, R.A. 2022. Dissimilar sensitivities of ocean acidification metrics to anthropogenic carbon accumulation in the central North Pacific Ocean and California Current Large Marine Ecosystem. Geophys. Res. Lett. 49(15):e2022GL097835. https://doi.org/10.1029/2022GL097835

Bach, L.T. 2015. Reconsidering the role of carbonate ion concentration in calcification by marine organisms. Biogeosciences 12:4939–4951. https://doi.org/10.5194/bg-12-4939-2015

Barclay, K. M., Gurney-Smith, H. J., Ahmed, M., Christian, J. R., Cyr, F., Duke, P. J., Else, B. G. T., Gimenez, I., Lizotte, M., Reader, M. C., Roth, M., Rutherford, K., Starr, M., Steiner, N. S., Turner, J., VanderZwaag, D. L., and Evans, W. 2026. Ocean acidification in Canada: the current state of knowledge and pathways for action. Front. Mar. Sci. 13:1761703. https://doi.org/10.3389/fmars.2026.1761703

Bates, N.R., Astor, Y.M., Church, M.J., Currie, K., Dore, J.E., González-Dávila, M., Lorenzoni, L., Muller-Karger, F., Olafsson, J., and Santana-Casiano, J.M. 2014. A time-series view of changing ocean chemistry due to ocean uptake of anthropogenic CO_2 and ocean acidification. Oceanography 27(1):126–141. https://doi.org/10.5670/oceanog.2014.16

Bednaršek, N., Feely, R.A., Howes, E.L., Hunt, B.P.V., Kessouri, F., León, P., Lischka, S., Maas, A.E., McLaughlin, K., Nezlin, N.P., Sutula, M., and Weisberg, S.B. 2019. Systematic review and meta-analysis toward synthesis of thresholds of ocean acidification impacts on calcifying pteropods and interactions with warming. Front. Mar. Sci. 6:227. https://doi.org/10.3389/fmars.2019.00227

Bernier, R.Y., Jamieson, R.E., Kelly, N.E., Lafleur, C., and Moore, A.M. (eds.). 2023. State of the Atlantic Ocean: synthesis report. Can. Tech. Rep. Fish. Aquat. Sci. 3544: v+219 p.

Blais, M., Clay, S.A., Galbraith, P.S., Bourassa, M.N. 2026. Chemical and Biological Oceanographic Conditions in the Gulf of St. Lawrence During 2025. Can. Tech. Rep. Hydrogr. Ocean. Sci. 425 : vi + 92 p. https://doi.org/10.60825/2tnm-4r87

Borges, A.V., and Gypens, N. 2010. Carbonate chemistry in the coastal zone responds more strongly to eutrophication than ocean acidification. Limnol. Oceanogr. 55(1):346–353.

Bourdages, H., Brassard, C., Desgagnés, M., Galbraith, P., Gauthier, J., Légaré, B., Nozères, C., and Parent, E. 2017. Preliminary results from the groundfish and shrimp multidisciplinary survey in August 2016 in the Estuary and northern Gulf of St. Lawrence. DFO Can. Sci. Advis. Sec. Res. Doc. 2017/002. v+87 p.

Bugden, G.L. 1991. Changes in the temperature–salinity characteristics of the deeper waters of the Gulf of St. Lawrence over the past several decades. In Therriault, J.-C. (ed.). The Gulf of St. Lawrence: small ocean or big estuary? Can. Spec. Publ. Fish. Aquat. Sci. 113:139–147.Cai, W.-J., Hu, X., Huang, W.-J., Murrell, M.C., Lehrter, J.C., Lohrenz, S.E., Chou, W.-C., Zhai, W., Hollibaugh, J., Wang, Y., Zhao, P., Guo, X., Gundersen, K., Dai, M., and Gong, G.-C. 2011. Acidification of subsurface coastal waters enhanced by eutrophication. Nat. Geosci. 4:766–770. https://doi.org/10.1038/ngeo1297

Cai, W.-J., Hu, X., Huang, W.-J., Murrell, M.C., Lehrter, J.C., Lohrenz, S.E., Chou, W.-C., Zhai, W., Hollibaugh, J.T., Wang, Y., Zhao, P., Guo, X., Gundersen, K., Dai, M., and Gong, G.-C. 2011. Acidification of subsurface coastal waters enhanced by eutrophication. Nat. Geosci. 4:766-770. https://doi.org/10.1038/ngeo1297

Cai, W.-J., Huang, W.-J., Luther III, G.W., Pierrot, D., Li, M., Testa, J., Xue, M., Joesoef, A., Mann, R., Brodeur, J., Xu, Y.-Y., Chen, B., Hussain, N., Waldbusser, G.G., Cornwell, J., and Kemp, M.W. 2017. Redox reactions and weak buffering capacity lead to acidification in the Chesapeake Bay. Nat. Commun. 8:369. https://doi.org/10.1038/s41467-017-00417-7

Cai, W.-J., Feely, R.A., Testa, J.M., Li, M., Evans, W., Alin, S.R., Xu, Y.-Y., Pelletier, G., Ahmed, A., Greeley, D.J., Newton, J.A., and Bednaršek, N. 2021. Natural and anthropogenic drivers of acidification in large estuaries. Annu. Rev. Mar. Sci. 13:23–55. https://doi.org/10.1146/annurev-marine-010419-011004

Caldeira, K., and Wickett, M. 2003. Anthropogenic carbon and ocean pH. Nature 425:365. https://doi.org/10.1038/425365a

Chamberland, J.-M., Bourdages, H., Desgagnés, M., Galbraith, P., Isabel, L., Ouellette-Plante, J., Roux, M.-J., Scallon-Chouinard, P.-M., and Senay, C. 2025. Preliminary results from the 2024 August ecosystemic survey in the Estuary and northern Gulf of St. Lawrence. DFO Can. Sci. Advis. Sec. Res. Doc. 2025/032. iv+101 p.

Chan, F., Barth, J.A., Blanchette, C.A., Byrne, R.H., Chavez, F., Cheriton, O., Feely, R.A., Friederich, G., Gaylord, B., Gouhier, B., Hacker, S., Hill, T., Hofmann, G., McManus, M.A., Menge, B.A., Nielsen, K.J., Russell, A., Sanford, E., Sevadjian, J., and Washburn, L. 2017. Persistent spatial structuring of coastal ocean acidification in the California Current System. Sci. Rep. 7:2526. https://doi.org/10.1038/s41598-017-02777-y

Chan, F., Barth, J.A., Kroeker, K.J., Lubchenco, J., and Menge, B.A. 2019. The dynamics and impact of ocean acidification and hypoxia: insights from sustained investigations in the Northern California Current Large Marine Ecosystem. Oceanography 32(3):62–71. https://doi.org/10.5670/oceanog.2019.312

Chassé, J., Lambert, N., Comeau, M., Galbraith, P., Larouche, P., and Pettipas, R. 2014. Environmental conditions in the southern Gulf of St. Lawrence relevant to lobster. DFO Can. Sci. Advis. Sec. Res. Doc. 2014/031. v + 25 p.

Chen, J., Glibert, P.M., Cai, W.-J., and Huang, D. 2023. Editorial: eutrophication, algal bloom, hypoxia and ocean acidification in large river estuaries, volume II. Front. Mar. Sci. 10:1225903. https://doi.org/10.3389/fmars.2023.1225903

Clayton, T.D., and Byrne, R.H. 1993. Spectrophotometric seawater pH measurements: total hydrogen ion concentration scale calibration of m-cresol purple and at-sea results. Deep Sea Res. Part I Oceanogr. Res. Pap. 40(10):2115–2129. https://doi.org/10.1016/0967-0637(93)90048-8

Clements, J.C., and Hunt, H.L. 2015. Marine animal behaviour in a high CO_2 ocean. Mar. Ecol. Prog. Ser. 536:259–279. https://doi.org/10.3354/meps11426

Collins, M., Truebano, M., Verbeke, W.C.E.P., and Spicer, J.I. 2021. Do aquatic ectotherms perform better under hypoxia after warm acclimation? J. Exp. Biol. 224:jeb232512. https://doi.org/10.1242/jeb.232512

Cornwall, C.E., Comeau, S., and Harvey, B.P. 2024. Are physiological and ecosystem-level tipping points caused by ocean acidification? A critical evaluation. Earth Syst. Dynam. 15(3):671–687. https://doi.org/10.5194/esd-15-671-2024

Cyronak, T., Schulz, K.G., and Jokiel, P.L. 2016. The omega myth: what really drives lower calcification rates in an acidifying ocean. ICES J. Mar. Sci. 73(3):558–562. https://doi.org/10.1093/icesjms/fsv075

Dickson, A.G. 1990. Standard potential of the reaction AgCl(s) + 1/2 H2(g) = Ag(s) + HCl(aq), and the standard acidity constant of the ion HSO_4^- in synthetic seawater from 273.15 to 318.15 K. J. Chem. Thermodyn. 22(2):113–127. https://doi.org/10.1016/0021-9614(90)90074-Z

Dickson, A.G. 2010. Standards for ocean measurements. Oceanography 23(3):34–47. https://doi.org/10.5670/oceanog.2010.22

Dickson, A.G., and Riley, J.P. 1979. The estimation of acid dissociation constants in seawater media from potentiometric titrations with strong base. Mar. Chem. 7(2):89–99. https://doi.org/10.1016/0304-4203(79)90001-X

Dickson, A.G., Sabine, C.L., and Christian, J.R. (eds.). 2007. Guide to best practices for ocean CO_2 measurements. PICES Spec. Publ. 3. 191 p.

Dinauer, A., and Mucci, A. 2017. Spatial variability in surface-water pCO_2 and gas exchange in the world's largest semi-enclosed estuarine system: St. Lawrence Estuary (Canada). Biogeosciences, 14, 3221-3237. https://doi.org/10.5194/bg-14-3221-2017

Dixson, D.L., Munday, P.L., and Jones, G.P. 2010. Ocean acidification disrupts the innate ability of fish to detect predator olfactory cues. Ecol. Lett. 13(1):68–75. https://doi.org/10.1111/j.1461-0248.2009.01400.x

Dixson, D.L., Jennings, A.R., Atema, J., and Munday, P.L. 2015. Odor tracking in sharks is reduced under ocean acidification conditions. Glob. Change Biol. 21:1454–1462. https://doi.org/10.1111/gcb.12678

Dodd, L. F., Grabowski, J. H., Piehler, M. F., and Westfield, I. 2020. Ocean acidification impairs crab larval development and survival. Mar. Environ. Res. 159:104948. https://doi.org/10.1016/j.marenvres.2020.104948

Doney, S.C., Fabry, V.J., Feely, R.A., and Kleypas, J.A. 2009. Ocean Acidification: The Other CO_2 Problem. Annu. Rev. Mar. Sci. 1:169–192. https://doi.org/10.1146/annurev.marine.010908.163834

Doney, S.C., Busch, D.S., Cooley, S.R., and Kroeker, K.J. 2020. The Impacts of Ocean Acidification on Marine Ecosystems and Reliant Human Communities. Annu. Rev. Environ. Resour. 45:83–112. https://doi.org/10.1146/annurev-environ-012320-083019

European Environment Agency (EEA). 2024. Ocean acidification. Indicators. https://www.eea.europa.eu/en/analysis/indicators/ocean-acidification

Egleston, E.S., Sabine, C.L., and Morel, F.M.M. 2010. Revelle revisited: Buffer factors that quantify response of ocean chemistry to changes in DIC and alkalinity. Global Biogeochem. Cy. 24:9 p. https://doi.org/10.1029/2008GB003407

Emerson, S., and Hedges, J. 2008. Chemical oceanography and the marine carbon cycle. Cambridge University Press, New York. 453 p. https://doi.org/10.1017/CBO9780511793202

Fabry, V.J., Seibel, B.A., Feely, R.A., and Orr, J.C. 2008. Impacts of ocean acidification on marine fauna and ecosystem processes. ICES J. Mar. Sci. 65(3):414–432. https://doi.org/10.1093/icesjms/fsn048

Fassbender, A.J., Carter, B.R., Sharp, J.D., Huang, Y., Arroyo, M.C., and Frenzel, H. 2023. Amplified subsurface signals of ocean acidification. Global Biogeochem. Cy. 37(12):14 p. https://doi.org/10.1029/2023GB007843

Feely, R.A., Sabine, C.L., Lee, K., Berelson, W., Kleypas, J., Fabry, V.J., and Millero, F.J. 2004. Impact of Anthropogenic CO_2 on the $CaCO_3$ System in the Oceans. Science 305:362–366. https://doi.org/10.1126/science.1097329

Feely, R.A., Sabine, C.L., Hernandez-Ayon, J.M., Ianson, D., and Hales, B. 2008. Evidence for Upwelling of Corrosive "Acidified" Water onto the Continental Shelf. Science 320:1490–1492. https://doi.org/10.1126/science.1155676

Feely, R.A., Alin, S.R., Carter, B., Bednarsek, N., Hales, B., Chan, F., Hill, T.M., Gaylord, B., Sanford, E., Byrne, R.H., Sabine, C.L., Greeley, D., and Juranek, L. 2016. Chemical and biological impacts of ocean acidification along the west coast of North America. Estuar. Coast. Shelf Sci. 183:260–270. http://dx.doi.org/10.1016/j.ecss.2016.08.043

Feely, R.A., Okazaki, R.R., Cai, W.-J., Bednarsek, N., Alin, S.R., Byrne, R.H., and Fassbender, A. 2018. The combined effects of acidification and hypoxia on pH and aragonite saturation in the coastal waters of the California current ecosystem and the northern Gulf of Mexico. Cont. Shelf Res. 152:50–60. https://doi.org/10.1016/j.csr.2017.11.002

Figuerola, B., Hancock, A. M., Stark, J. S., and King, C. K. 2021. A review and meta-analysis of potential impacts of ocean acidification on marine calcifiers from the Southern Ocean. Front. Mar. Sci. 8:584445. https://doi.org/10.3389/fmars.2021.584445

Figuerola, B., Griffiths, H.J., Krzeminska, M., Piwoni-Piorewicz, A., Iglikowska, A., and Kuklinski, P. 2022. Temperature as a likely driver shaping global patterns in mineralogical composition in bryozoans: implications for marine calcifiers under global change. Ecography e06381, 14 p. https://doi.org/10.1111/ecog.06381

Findlay, S.F., Feely, R.A., Jiang, L.-Q., Pelletier, G., and Bednaršek, N. 2025. Ocean Acidification: Another Planetary Boundary Crossed. Glob. Chang. Biol. 17p. https://doi.org/10.1111/gcb.70238

Frankignoulle, M., Canon, C., and Gattuso, J.-P. 1994. Marine calcification as a source of carbon dioxide: Positive feedback of increasing atmospheric CO_2. Limnol. Oceanogr. 39(2):458–462. https://doi.org/10.4319/lo.1994.39.2.0458

Gaitán-Espitia, J.D., Marshall, D., Dupont, S., Bacigalupe, L.D., Bodrossy, L., and Hobday, A.J. 2017a. Geographical gradients in selection can reveal genetic constraints for evolutionary responses to ocean acidification. Biol. Lett. 13:20160784. https://doi.org/10.1098/rsbl.2016.0784

Gaitán-Espitia, J.D., Villanueva, P.A., Lopez, J., Torres, R., Navarro, J.M., and Bacigalupe, L.D. 2017b. Spatio-temporal environmental variation mediates geographical differences in phenotypic responses to ocean acidification. Biol. Lett. 13:20160865. https://doi.org/10.1098/rsbl.2016.0865

Gaitán-Espitia, J.D., Vargas, C.A., and Hofmann, G.E. 2023. Phenotypic plasticity and physiological tolerance shape marine organisms' responses to climate change. Front. Mar. Sci. 10:1231099. https://doi.org/10.3389/fmars.2023.1231099

Galbraith, P.S. 2006. Winter water masses in the Gulf of St. Lawrence. J. Geophys. Res. Oceans 111:C06022. https://doi.org/10.1029/2005JC003159

Galbraith, P.S., Blais, M., Lizotte, M., Bélanger, D., Casault, B., Clay, S., Layton, C., Penney, J., Gabriel, C.-E., Ringuette, M., Azetsu-Scott, K., Chassé, J., Coyne, J., Devred, E., Johnson, C.L., Maillet, G., Shaw, J.-L., Starr, M. 2026a. Oceanographic conditions in the Atlantic Zone in 2025. Can. Tech. Rep. Hydrogr. Ocean. Sci. 420: v + 49 p. https://doi.org/10.60825/q1xj-q540

Galbraith, P.S., Chassé, J., Shaw, J.-L., Lefaivre, D., and Bourassa, M.-N. 2026b. Physical Oceanographic Conditions in the Gulf of St. Lawrence during 2025. Can. Tech. Rep. Hydrogr. Ocean Sci. 418: v + 94 p. https://doi.org/10.60825/a1qy-zx55

Gattuso, J.-P., Epitalon, J.-M., Lavigne, H., Orr, J., Gentili, B., Hagens, M., Hofmann, A., Mueller, J.-D., Proye, A., Rae, J., and Soetaert, K. 2024. seacarb: seawater carbonate chemistry, version 3.3.3. https://doi.org/10.32614/CRAN.package.seacarb

Gattuso, J.-P., Frankignoulle, M., and Wollast, R. 1998. Carbon and carbonate metabolism in coastal aquatic ecosystems. Annu. Rev. Ecol. Syst. 29:405–434. https://doi.org/10.1146/annurev.ecolsys.29.1.405

Gattuso, J.-P., and Hansson, L. 2020. Ocean acidification. Oxford University Press, Oxford. xix+326 p.

Gazeau, F., Parker, L.M., Comeau, S., Gattuso, J.-P., O'Connor, W.A., Martin, S., Pörtner, H.-O., and Ross, P.M. 2013. Impacts of ocean acidification on marine shelled molluscs. Mar. Biol. 160:2207–2245. https://doi.org/10.1007/s00227-013-2219-3

Gehlen, M., Gruber, N., Gangsto, R., Bopp, L., and Oschlies, A. 2011. Biogeochemical consequences of ocean acidification and feedbacks to the Earth system. In Gattuso, J.-P., and Hansson, L. (eds.). Ocean acidification. https://doi.org/10.1093/oso/9780199591091.003.0017

Genovesi, L., de Vernal, A., Thibodeau, B., Hilaire-Marcel, C., Mucci, A., and Gilbert, D. 2011. Recent changes in bottom water oxygenation and temperature in the Gulf of St. Lawrence: micropaleontological and geochemical evidence. Limnol. Oceanogr. 56(4):1319–1329. https://doi.org/10.4319/lo.2011.56.4.1319

Gibb, O., Cyr, F., Azetsu-Scott, K., Chassé, J., Childs, D., Gabriel, C.-E., Galbraith, P.S., Maillet, G., Pepin, P., Punshon, S., and Starr, M. 2023. Spatiotemporal variability in pH and carbonate parameters on the Canadian Atlantic continental shelf between 2014 and 2022. Earth Syst. Sci. Data 15:4127–4162. https://doi.org/10.5194/essd-15-4127-2023

Gilbert, D., and Pettigrew, B. 1997. Interannual variability (1948–1994) of the CIL core temperature in the Gulf of St. Lawrence. Can. J. Fish. Aquat. Sci. 54(S1):57–67. https://doi.org/10.1139/f96-160

Gilbert, D., Sundby, B., Gobeil, C., Mucci, A., and Tremblay, G.-H. 2005. A seventy-two-year record of diminishing deep-water oxygen in the St. Lawrence Estuary: the northwest Atlantic connection. Limnol. Oceanogr. 50(5):1654–1666. https://doi.org/10.4319/lo.2005.50.5.1654

Gruber, N., Clement, D., Carter, B.R., Feely, R.A., van Heuven, S., Hoppema, M., Ishii, M., Key, R.M., Kozyr, A., Lauvset, S.K., Monaco, C.L., Mathis, J.T., Murata, A., Olsen, A., Pérez, F.F., Sabine, C.L., Tanhua, T., and Wanninkhof, R. 2019. The oceanic sink for anthropogenic CO_2 from 1994 to 2007. Science 363:1193–1199. https://doi.org/10.1126/science.aau5153

Gruber, N., Bakker, D.C.E., DeVries, T., Gregor, L., Hauck, J., Landschützer, P., McKinley, G.A., and Müller, J.D. 2023. Trends and variability in the ocean carbon sink. Nat. Rev. Earth Environ. 4:119–134. https://doi.org/10.1038/s43017-022-00381-x

Hall, N.S., Testa, J.M., Li, M., and Paerl, H.W. 2023. Assessing drivers of estuarine pH: a comparative analysis of the continental U.S.A.'s two largest estuaries. Limnol. Oceanogr. 68:2227–2244. https://doi.org/10.1002/lno.12418

Hassoun, A.E.R., Sutton, A., Dupont, S., Guo, X., and Hernandez-Ayon, J.M. 2025. Editorial: Time-series observations of ocean acidification: a key tool for documenting impacts on a changing planet. Front. Mar. Sci. 12:1581134. https://doi.org/10.3389/fmars.2025.1581134

Hönisch, B., Ridgwell, A., Schmidt, D.N., Thomas, E., Gibbs, S.J., Sluijs, A., Zeebe, R., Kump, L., Martindale, R.C., Greene, S.E., Kiessling, W., Ries, J., Zachos, J.C., Royer, D.L., Barker, S., Marchitto, T.M., Moyer, R., Pelejero, C., Ziveri, P., Foster, G.L., and Williams, B. 2012. The geological record of ocean acidification. Science 335:1058–1063. https://doi.org/10.1126/science.1208277

Hu, X. 2020. Effect of organic alkalinity on seawater buffer capacity: a numerical exploration. Aquat. Geochem. 26:161–178. https://doi.org/10.1007/s10498-020-09375-x

Huo, D., Sun, L., Sun, J., Zhang, L., Liu, S., Su, F., and Yang, H. 2021. Sea cucumbers in a high temperature and low dissolved oxygen world: roles of miRNAs in the regulation of environmental stresses. Environ. Pollut. 268:115509. https://doi.org/10.1016/j.envpol.2020.115509

Huo, D., Gaitán-Espitia, J.D., Spicer, J.I., and Yang, H. 2023. Editorial: the adaptation and response of aquatic animals in the context of global climate change. Front. Mar. Sci. 10:1231099. https://doi.org/10.3389/fmars.2023.1231099

IPBES. 2019. Summary for policymakers of the global assessment report on biodiversity and ecosystem services of the Intergovernmental Science-Policy Platform on Biodiversity and Ecosystem Services. IPBES secretariat, Bonn, Germany. 56 p. https://doi.org/10.5281/zenodo.3553579

Johnson, K.M., Wills, K.D., Butler, D.B., Johnson, W.K., and Wong, C.S. 1993. Coulometric total carbon dioxide analysis for marine studies: maximizing the performance of an automated gas extraction system and coulometric detector. Mar. Chem. 44(2–4):167–187. https://doi.org/10.1016/0304-4203(93)90201-X

Jokiel, P.L. 2011. Ocean acidification and control of reef coral calcification by boundary layer limitation of proton flux. Bull. Mar. Sci. 87(3):639–657. https://doi.org/10.5343/bms.2010.1107

Jokiel, P.L. 2013. Coral reef calcification: carbonate, bicarbonate and proton flux under conditions of increasing ocean acidification. Proc. R. Soc. B 280(1764):20130031. https://doi.org/10.1098/rspb.2013.0031

Jutras, M., Dufour, C.O., Mucci, A., Talbot, L.C., 2023a. Large-scale control of the retroflection of the Labrador Current. Nature Communications 14:2623. https://doi.org/10.1038/s41467023-38321-y

Jutras, M., Mucci, A., Chaillou, G., Nesbitt, W.A., and Wallace, D.W.R. 2023b. Temporal and spatial evolution of bottom-water hypoxia in the St Lawrence estuarine system, Biogeosciences, 20, 839-849. https://doi.org/10.5194/bg-20-839-2023

Kahil, K., Weiner, S., Addadi, L., and Gal, A. 2021. Ion pathways in biomineralization: perspectives on uptake, transport, and deposition of calcium, carbonate, and phosphate. J. Am. Chem. Soc. 143(50):21100–21112. https://doi.org/10.1021/jacs.1c09174

Keppel, E.A., Scrosati, R.A., and Courtenay, S.C. 2012. Ocean acidification decreases growth and development in American lobster (Homarus americanus) larvae. J. Northw. Atl. Fish. Sci. 44:61–66. https://doi.org/10.2960/J.v44.m683

Kerr, D.E., Brown, P.J., Grey, A., and Kelleher, B.P. 2021. The influence of organic alkalinity on the carbonate system in coastal waters. Mar. Chem. 237:104050. https://doi.org/10.1016/j.marchem.2021.104050

Knor, L. A. C. M., Sabine, C. L., Dore, J. E., White, A. E., and Potemra, J. 2025. Drivers and variability of intensified subsurface ocean acidification trends at station ALOHA. J. Geophys. Res. Oceans, 130, e2024JC022251. https://doi.org/10.1029/2024JC022251

Koutitonsky, V. 1991. The physical oceanography of the Gulf of St. Lawrence: A review with emphasis on the synoptic variability of the motion. In The Gulf of St. Lawrence: Small ocean or big estuary? Can. Spec. Publ. Fish. Aquat. Sci. Edited by J.-C. Therriault. pp. 57–90.

Kroeker, K.J., Kordas, R.L., Crim, R.N., and Singh, G.G. 2010. Meta-analysis reveals negative yet variable effects of ocean acidification on marine organisms. Ecol. Lett. 13(11):1419–1434. https://doi.org/10.1111/j.1461-0248.2010.01518.x

Lauvset, S.K., Gruber, N., Landschützer, P., Olsen, A., and Tjiputra, J. 2015. Trends and drivers in global surface ocean pH over the past three decades. Biogeosciences 12:1285–1298. https://doi.org/10.5194/bg-12-1285-2015

Lauvset, S.K., Carter, B.R., Pérez, F.F., Feely, R.A., Velo, A., and Olsen, A. 2020. Processes driving global interior ocean pH distribution. Global Biogeochem. Cycles 34(1):e2019GB006229. https://doi.org/10.1029/2019GB006229

Lavoie, D., Lambert, N., Rousseau, S., Dumas, J., Chassé, J., Long, Z., Perrie, W., Starr, M., Brickman, D., and Azetsu-Scott, K. 2020. Projections of future physical and biochemical conditions in the Gulf of St. Lawrence, on the Scotian Shelf and in the Gulf of Maine using a regional climate model. Can. Tech. Rep. Hydrogr. Ocean Sci. 334: xiii+102 p.

Lavoie, D., Lambert, N., Starr, M., Chassé, J., Riche, O., Le Clainche, Y., Azetsu-Scott, K., Béjaoui, B., Christian, J.R., and Gilbert, D. 2021. The Gulf of St. Lawrence Biogeochemical Model: a modelling tool for fisheries and ocean management. Front. Mar. Sci. 8:732269. https://doi.org/10.3389/fmars.2021.732269

Lee, K., Kim, T.-W., Byrne, R.H., Millero, F.J., Feely, R.A., and Liu, Y.-M. 2010. The universal ratio of boron to chlorinity for the North Pacific and North Atlantic oceans. Geochim. Cosmochim. Acta 74(6):1801–1811. https://doi.org/10.1016/j.gca.2009.12.027

Leung, J.Y.S., Zhang, S., and Connell, S.D. 2022. Is ocean acidification really a threat to marine calcifiers? A systematic review and meta-analysis of 980+ studies spanning two decades. Small 18(35):e2107407. https://doi.org/10.1002/smll.202107407

Li, M., Guo, Y., Cai, W.-J., Testa, J.M., Shen, C., Li, R., and Su, J. 2023. Projected increase in carbon dioxide drawdown and acidification in large estuaries under climate change. Commun. Earth Environ. 4:68. https://doi.org/10.1038/s43247-023-00733-5

Li, M., Li, R., Guo, Y., Testa, J.M., Cai, W.-J., Shen, C., Chen, Y., and Kaushal, S.S. 2025. Disentangling the effects of global and regional drivers on diverse long-term pH trends in coastal waters. AGU Adv. 6:e2024AV001350. https://doi.org/10.1029/2024AV001350

Long, W.C., Swiney, K.M., Harris, C., Page, H.N., and Foy, R.J. 2016. Effects of ocean acidification on juvenile red king crab (Paralithodes camtschaticus) and Tanner crab (Chionoecetes bairdi) growth, condition, calcification, and survival. ICES J. Mar. Sci. 73(3):716–726. https://doi.org/10.1093/icesjms/fsv205

Lueker, T.J., Dickson, A.G., and Keeling, C.D. 2000. Ocean pCO_2 calculated from dissolved inorganic carbon, alkalinity, and equations for K1 and K2: validation based on laboratory measurements of CO2 in gas and seawater at equilibrium. Mar. Chem. 70(1–3):105–119. https://doi.org/10.1016/S0304-4203(00)00022-0

Mackinder, L., Wheeler, G., Schroeder, D., Riebesell, U., and Brownlee, C. 2010. Molecular mechanisms underlying calcification in coccolithophores. Geomicrobiol. J. 27:585–595. https://doi.org/10.1080/01490451003703014

Majdisova, Z., and Skala, V. 2017. Radial basis function approximations: comparison and applications. Appl. Math. Model. 51:728–743. https://doi.org/10.1016/j.apm.2017.07.033

Mann, S. 2001. Biomineralization: principles and concepts in bioinorganic materials chemistry. Oxford University Press, New York. https://doi.org/10.1093/oso/9780198508823.001.0001

Martínez-Trejo, J.A., Cardoso-Mohedano, J.G., Sanchez-Cabeza, J.A., Ayón, J.M.H., Ruiz-Fernández, A.C., Gómez-Ponce, M.A., Barranco, L., and Pech, D. 2024. Variability of dissolved inorganic carbon in the most extensive karst estuarine–lagoon system of the southern Gulf of Mexico. Estuaries Coasts 47:2573–2588. https://doi.org/10.1007/s12237-024-01384-1

McNeil, B., and Sasse, T. 2016. Future ocean hypercapnia driven by anthropogenic amplification of the natural CO_2 cycle. Nature 529:383–386. https://doi.org/10.1038/nature16156

Melzner, F., Mark, F.C., Seibel, B.A., and Tomanek, L. 2020. Ocean acidification and coastal marine invertebrates: tracking CO2 effects from seawater to cell. Annu. Rev. Mar. Sci. 12:499–523. https://doi.org/10.1146/annurev-marine-010419-010658

Michaelidis, B., Spring, A., and Pörtner, H.-O. 2007. Effects of long-term acclimation to environmental hypercapnia on the physiology of the Mediterranean fish Sparus aurata. Mar. Biol. 150(6):1417–1429. https://doi.org/10.1007/s00227-006-0390-5

Middelburg, J.J., Soetaert, K., and Hagens, M. 2020. Ocean alkalinity, buffering and biogeochemical processes. Rev. Geophys. 58(3):e2019RG000681. https://doi.org/10.1029/2019RG000681

Millero, F.J. 1986. The pH of estuarine waters. Limnol. Oceanogr. 31(4):839–847. https://doi.org/10.4319/lo.1986.31.4.0839

Mintrop, L., Pérez, F.F., González-Dávila, M., Santana-Casiano, J.M., and Körtzinger, A. 2000. Alkalinity determination by potentiometry: intercalibration using three different methods. Cienc. Mar. 26(1):23–27. https://doi.org/10.7773/cm.v26i1.573

Mitchell, M.R., Harrison, G., Pauley, K., Gagné, A., Maillet, G., and Strain, P. 2002. Atlantic Zonal Monitoring Program sampling protocol. Can. Tech. Rep. Hydrogr. Ocean Sci. 223: iv+23 p.

Moraga, P. 2023. Spatial statistics for data science: theory and practice with R (1st ed.). Chapman and Hall/CRC, New York. 298 p. https://doi.org/10.1201/9781032641522

Morse, J.W., and Mackenzie, F.T. 1990. Geochemistry of sedimentary carbonates. Elsevier, Amsterdam. 707 p.

Morse, J.W., Arvidson, R.S., and Lüttge, A. 2007. Calcium carbonate formation and dissolution. Chem. Rev. 107(2):342–381. https://doi.org/10.1021/cr050358j

Mucci, A. 1983. The solubility of calcite and aragonite in seawater at various salinities, temperatures, and one atmosphere total pressure. Am. J. Sci. 283(7):780–799. https://doi.org/10.2475/ajs.283.7.780

Mucci, A., Starr, M., Gilbert, D., and Sundby, B. 2011. Acidification of Lower St. Lawrence Estuary bottom waters. Atmos.–Ocean 49(3):206–218. https://doi.org/10.1080/07055900.2011.599265

Mucci, A., Levasseur, M., Gratton, Y., Martias, C., Scarratt, M., Gilbert, D., Tremblay, J.-É., Ferreyra, G., and Lansard, B. 2017. Tidally induced variations of pH at the head of the Laurentian Channel. Can. J. Fish. Aquat. Sci. 75:1128–1141. https://doi.org/10.1139/cjfas-2017-0007

Mucci, A., and Jutras, M. 2026. Seasonally-variable surface-water CO_2 gradients and fluxes along the Gulf and St. Lawrence Estuary (Quebec, Canada). Mar. Chem. 276:104637. https://doi.org/10.1016/j.marchem.2026.104637

Nesbitt, W. A., Stevens, S. W., Mucci, A. O., Gerke, L., Tanhua, T., Chaillou, G., and Wallace, D. W. R. 2025. The coupled oxygen and carbon dynamics in the subsurface waters of the Gulf and Lower St. Lawrence Estuary and implications for artificial oxygenation, Ocean Sci., 21, 2179–2195. https://doi.org/10.5194/os-21-2179-2025

Nilsson, G.E., Dixson, D.L., Domenici, P., McCormick, M.I., Sørensen, C., Watson, S.-A., and Munday, P.L. 2012. Near-future carbon dioxide levels alter fish behaviour by interfering with neurotransmitter function. Nat. Clim. Change 2:201–204. https://doi.org/10.1038/nclimate1352

Ninokawa, A.T., Saley, A.M., Shalchi, R., and Gaylord, B. 2024. Multiple carbonate system parameters independently govern shell formation in a marine mussel. Commun. Earth Environ. 5:273. https://doi.org/10.1038/s43247-024-01440-5

NOAA Ocean Acidification Program. 2024. Ocean acidification. Copernicus Marine Environment Monitoring Service.

Noor, N.M., and Das, S.K. 2019. Effects of Elevated Carbon Dioxide on Marine Ecosystem and Associated Fishes. *Thalassas* 35: 421-429. https://doi.org/10.1007/s41208-019-00161-3

Nozères, C., Archambault, D., Chouinard, P.-M., Gauthier, J., Miller, R., Parent, E., Schwab, P., Savard, L., and Dutil, J.-D. 2010. Identification guide for marine fishes of the estuary and northern Gulf of St. Lawrence and sampling protocols used during trawl surveys between 2004 and 2008. Can. Tech. Rep. Fish. Aquat. Sci. 2866: xi+243 p.

Orr, J., Fabry, V., Aumont, O., Bopp, L., Doney, S.C., Feely, R.A., Gnanadesikan, A., Gruber, N., Ishida, A., Joos, F., Key, R.M., Lindsay, K., Maier-Reimer, E., Matear, R., Monfray, P., Mouchet, A., Najjar, R.G., Plattner, G.-K., Rodgers, K.B., Sabine, C.L., Sarmiento, J.L., Schlitzer, R., Slater, R.D., Totterdell, I.J., Weirig, M.-F., Yamanaka, Y., and Yool, A. 2005. Anthropogenic ocean acidification over the twenty-first century and its impact on calcifying organisms. Nature 437:681–686. https://doi.org/10.1038/nature04095

Orr, J.C., Epitalon, J.-M., and Gattuso, J.-P. 2015. Comparison of ten packages that compute ocean carbonate chemistry. Biogeosciences 12:1483–1510. https://doi.org/10.5194/bg-12-1483-2015

Ouellet, P., and Sainte-Marie, B. 2018. Vertical distribution of snow crab (Chionoecetes opilio) pelagic stages in the Gulf of St. Lawrence (Canada) and effect of temperature on development and survival. ICES J. Mar. Sci. 75(2), 773–784. https://doi.org/10.1093/icesjms/fsx169

Padilla-Gamino, J.L., Alma, L., Spencer, L.H., Venkataraman, Y.R., and Wessler, L. 2022. Ocean acidification does not overlook sex: review of understudied effects and implications of low pH on marine invertebrate sexual reproduction. Front. Mar. Sci. 9:977754. https://doi.org/10.3389/fmars.2022.977754

Pascal, L., Cloutier-Artiwat, F., Zanon, A., Wallace, D. W. R., and Chaillou, G. 2025. New deoxygenation threshold for N_2 and N_2O production in coastal waters and sediments. Global Biogeochem. Cy., 39, e2024GB008218. https://doi.org/10.1029/2024GB008218

Perez, F.F., and Fraga, F. 1987. Association constant of fluoride and hydrogen ions in seawater. Mar. Chem. 21(2):161–168. https://doi.org/10.1016/0304-4203(87)90036-3

Pousse, E., Poach, M.E., Redman, D.H., Sennefelder, G., White, L.E., Lindsay, J.M., Munroe, D., Hart, D., Hennen, D., Dixon, M.S., Li, Y., Wikfors, G.H., and Meseck, S. 2020. Energetic response of Atlantic surfclam Spisula solidissima to ocean acidification. Mar. Pollut. Bull. 161:111740. https://doi.org/10.1016/j.marpolbul.2020.111740

Raimondi, L., Matthews, J.B.R., Atamanchuk, D., Azetsu-Scott, K., and Wallace, D.W.R. 2019. The internal consistency of the marine carbon dioxide system for high latitude shipboard and in situ monitoring. Mar. Chem. 213:49–70. https://doi.org/10.1016/j.marchem.2019.03.001

Reimer, J.J., Medeiros, P.M., Hussain, N., Gonski, S.F., Xu, Y.-Y., Huang, T.-H., and Cai, W.-J. 2024. Carbonate chemistry and the potential for acidification in Georgia coastal marshes and the South Atlantic Bight, USA. Estuaries Coasts 47:76–90. https://doi.org/10.1007/s12237-023-01261-3

Riebesell, U., Fabry, V.J., Hansson, L., and Gattuso, J.-P. (Editors). 2010. Guide to Best Practices for Ocean Acidification Research and Data Reporting. Publications Office of the European Union. 260 p.

Ries, J.B., Cohen, A.L., and McCorkle, D.C. 2009. Marine calcifiers exhibit mixed responses to CO2-induced ocean acidification. Geology 37(12):1131–1134. https://doi.org/10.1130/G30210A.1

Rodríguez-Domínguez, A., Connell, S.D., Baziret, C., and Nagelkerken, I. 2018. Irreversible behavioural impairment of fish starts early: embryonic exposure to ocean acidification. Mar. Pollut. Bull. 133:562–567. https://doi.org/10.1016/j.marpolbul.2018.06.004

Roleda, M.Y., Boyd, P.W., and Hurd, C.L. 2012. Before ocean acidification: calcifier chemistry lessons. J. Phycol. 48(4):840–843. https://doi.org/10.1111/j.1529-8817.2012.01195.x

Sakschewski, B., Caesar, L., Andersen, L., Bechthold, M., Bergfeld, L., Beusen, A., Billing, M., Bodirsky, B.L., Botsyun, S., Dennis, D., Donges, J.F., Dou, X., Eriksson, A., Fetzer, I., Gerten, D., Häyhä, T., Hebden, S., Heckmann, T., Heilemann, A., Huiskamp, W.N., Jahnke, A., Kaiser, J., Kitzmann, N., Krönke, J., Kühnel, D., Laureanti, N.C., Li, C., Liu, Z., Loriani, S., Ludescher, J., Mathesius, S., Norström, A., Otto, F., Paolucci, A., Pokhotelov, D., Rafiezadeh Shahi, K., Raju, E., Rostami, M., Schaphoff, S., Schmidt, C., Steinert, N.J., Stenzel, F., Virkki, V., Wendt-Potthoff, K., Wunderling, N., and Rockström, J. 2025. Planetary health check 2025: a scientific assessment of the state of the planet. Potsdam Institute for Climate Impact Research, Potsdam. 144 p. https://doi.org/10.48485/pik.2025.017

Shi, Y., and Li, Y. 2024. Impacts of ocean acidification on physiology and ecology of marine invertebrates: a comprehensive review. Aquat. Ecol. 58:207–226. https://doi.org/10.1007/s10452-023-10058-2

Siedlecki, S.A., Salisbury, J., Gledhill, D.K., Bastidas, C., Meseck, S., McGarry, K., Hunt, C.W., Alexander, M., Lavoie, D., Wang, Z.A., Scott, J., Brady, D.C., Mlsna, I., Azetsu-Scott, K., Liberti, C.M., Melrose, D.C., White, M.M., Pershing, A., Vandemark, D., Townsend, D.W., Chen, C., Mook, W., and Morrison, R. 2021. Projecting ocean acidification impacts for the Gulf of Maine to 2050: new tools and expectations. Elem. Sci. Anth. 9(1):29. https://doi.org/10.1525/elementa.2020.00062

Small, D.P., Calosi, P., Boothroyd, D., and Spicer, J.I. 2015. Stage-specific changes in physiological and life-history responses to elevated temperature and pCO_2 during the larval development of the European lobster Homarus gammarus (L.). Physiol. Biochem. Zool. 88(5):494–507. https://doi.org/10.1086/682238

Small, D.P., Calosi, P., Boothroyd, D., and Spicer, J.I. 2016. The sensitivity of the early benthic juvenile stage of the European lobster Homarus gammarus (L.) to elevated pCO_2 and temperature. Mar. Biol. 163:53. https://doi.org/10.1007/s00227-016-2834-x

Small, D.P., Calosi, P., Rastrick, S.P.S., Turner, L.M., Widdicombe, S., and Spicer, J.I. 2020. The effects of elevated temperature and pCO2 on the energetics and haemolymph pH homeostasis of juveniles of the European lobster Homarus gammarus. J. Exp. Biol. 223(8):jeb209221. https://doi.org/10.1242/jeb.209221

Spicer, J.I., and Morley, S.A. 2022. Hypercapnia in marine environments: physiological impacts and ecological consequences. Front. Mar. Sci. 9:977754. https://doi.org/10.3389/fmars.2022.977754

Steinhart, R. 2023. Temporal and spatial analysis of the relationship between hypoxia, temperature, and benthic biodiversity in the St. Lawrence Estuary and Gulf. M.Sc. thesis, Memorial University of Newfoundland. 143 p.

Stiasny, M.H., Mittermayer, F.H., Sswat, M., Voss, R., Jutfelt, F., Chierici, M., Puvanendran, V., Mortensen, A., Reusch, T.B.H., and Clemmesen, C. 2021. Ocean acidification effects on Atlantic cod larval survival and recruitment to the fished population. PLoS One 16(8):e0155448. https://doi.org/10.1371/journal.pone.0155448

Stolarski, J., van Dijk, I., and Benning, L. G. 2025. Controls on $CaCO_3$ Polymorphism: From Laboratory Precipitation to Biomineralization across Geological Time. Elements 21 (2): 92–97. https://doi.org/10.2138/gselements.21.2.92

Stumpp, M., Hu, M.Y., Melzner, F., Gutowska, M.A., Dorey, N., Himmerkus, N., Holtmann, W.C., Dupont, S., Thorndyke, M.C., and Bleich, M. 2012. Acidified seawater impacts sea urchin larval pH regulatory systems relevant for calcification. Proc. Natl. Acad. Sci. U.S.A. 109(44):18192–18197. https://doi.org/10.1073/pnas.1209174109

Takahashi, T., Sutherland, S.C., and Kozyr, A. 2017. Global ocean surface water partial pressure of CO2 database (1957–2019), LDEO database (version 2019). NOAA Natl. Cent. Environ. Inf. Dataset. https://doi.org/10.3334/CDIAC/OTG.NDP088(V2015)

Therriault, J.-C., Petrie, B., Gagnon, J., Gregory, D., Helbig, J., Herman, A., Lefaivre, D., Mitchell, M., Pelchat, B., Runge, J., and Sameoto, D. 1998. Proposal for a Northwest Atlantic Zonal Monitoring Program. Can. Tech. Rep. Hydrogr. Ocean Sci. 194: vii+57 p.

Thibodeau, B., de Vernal, A., and Mucci, A. 2006. Recent eutrophication and consequent hypoxia in the bottom waters of the Lower St. Lawrence Estuary: micropaleontological and geochemical evidence. Mar. Geol. 231(1–4):37–50. https://doi.org/10.1016/j.margeo.2006.05.010

Thibodeau, B., de Vernal, A., Hillaire-Marcel, C., and Mucci, A. 2010. Twentieth-century warming in deep waters of the Gulf of St. Lawrence: a unique feature of the last millennium. Geophys. Res. Lett. 37(17):L17604. https://doi.org/10.1029/2010GL044771

Thomsen, J., Haynert, K., Wegner, K.M., and Melzner, F. 2015. Impact of seawater carbonate chemistry on the calcification of marine bivalves. Biogeosciences 12:4209–4220. https://doi.org/10.5194/bg-12-4209-2015

Toyofuku, T., Matsuo, M.Y., de Nooijer, L.J., Nagai, Y., Kawada, S., Fujita, K., Reichart, G.-J., Nomaki, H., Tsuchiya, M., Sakaguchi, H., and Kitazato, H. 2017. Proton pumping accompanies calcification in foraminifera. Nat. Commun. 8:14145. https://doi.org/10.1038/ncomms14145

Waldbusser, G.G., and Salisbury, J.E. 2014. Ocean acidification in the coastal zone from an organism's perspective: multiple system parameters, frequency domains, and habitats. Annu. Rev. Mar. Sci. 6:221–247. https://doi.org/10.1146/annurev-marine-121211-172238

Wang, Z.A., Wanninkhof, R., Cai, W.-J., Byrne, R.H., Hu, X., Peng, T.-H., and Huang, W.-J. 2013. The marine inorganic carbon system along the Gulf of Mexico and Atlantic coasts of the United States: insights from a transregional coastal carbon study. Limnol. Oceanogr. 58(1):325–342. https://doi.org/10.4319/lo.2013.58.1.0325

Weiss, R.F. 1974. Carbon dioxide in water and seawater: the solubility of a non-ideal gas. Mar. Chem. 2(3):203–215. https://doi.org/10.1016/0304-4203(74)90015-2

Wright-Fairbanks, E., Jewett, E.B., and Coyle, K.O. 2025. Management considerations for establishing a coastal acidification monitoring system: insights from the U.S. Coastal Acidification Networks. Environ. Monit. Assess. 197:990. https://doi.org/10.1007/s10661-025-14434-3

Xue, L., and Cai, W.-J. 2020. Total alkalinity minus dissolved inorganic carbon as a proxy for deciphering ocean acidification mechanisms. Mar. Chem. 222:103791. https://doi.org/10.1016/j.marchem.2020.103791

Zeebe, R.E., and Wolf-Gladrow, D.A. 2001. CO_2 in Seawater: Equilibrium, Kinetics, Isotopes. Elsevier Oceanography Series 65. Elsevier Science B.V., Amsterdam, Netherlands. 346 p.

Ziveri, P., Langer, G., Chaabane, S., de Vries, J., Gray, W.R., Keul, N., Hatton, I.A., Manno, C., Norris, R., Pallacks, S., Young, J.R., Schiebel, R., Zarkogiannis, S., Anglada-Ortiz, G., Bianco, S., de Garidel-Thoron, T., Grelaud, M., Lucas, A., Probert, I., and Mortyn, P.G. 2025. Calcifying plankton: From biomineralization to global change. Science 390: eadq8520. https://doi.org/10.1126/science.adq8520

6. TABLES

Table 1: Overview of oceanographic sampling, including dates, vessels, regions, and number of stations sampled during high frequency monitoring and seasonal surveys conducted in 2025.

High Frequency Monitoring Station

Dates (2025)	Vessel	Station Name	Station Count
Apr. 15 - Nov. 13	*Beluga II* (+ others)	Rimouski	25

Surveys

Dates (2025)	Vessel	Region / Subregion	Station Count
May 31 - July 7	*Capt. Jacques Cartier*	Estuary	18
		Northwest Gulf	14
		Magdalen Shallows	41
		Northumberland Strait	2
		Centre Gulf / Cabot Strait	19
		Northeast Gulf	14
		Total	**108**
Aug. 8 - Sept. 20	*John Cabot / Capt. Jacques Cartier*	Estuary	11
		Northwest Gulf	7
		Magdalen Shallows	93
		Northumberland Strait	37
		Centre Gulf / Cabot Strait	22
		Northeast Gulf	13
		Total	**183**
Oct. 15 - Nov. 4	*Coriolis II*	Estuary	14
		Northwest Gulf	14
		Magdalen Shallows	18
		Northumberland Strait	11
		Centre Gulf / Cabot Strait	16
		Northeast Gulf	14
		Total	**87**

FIGURES

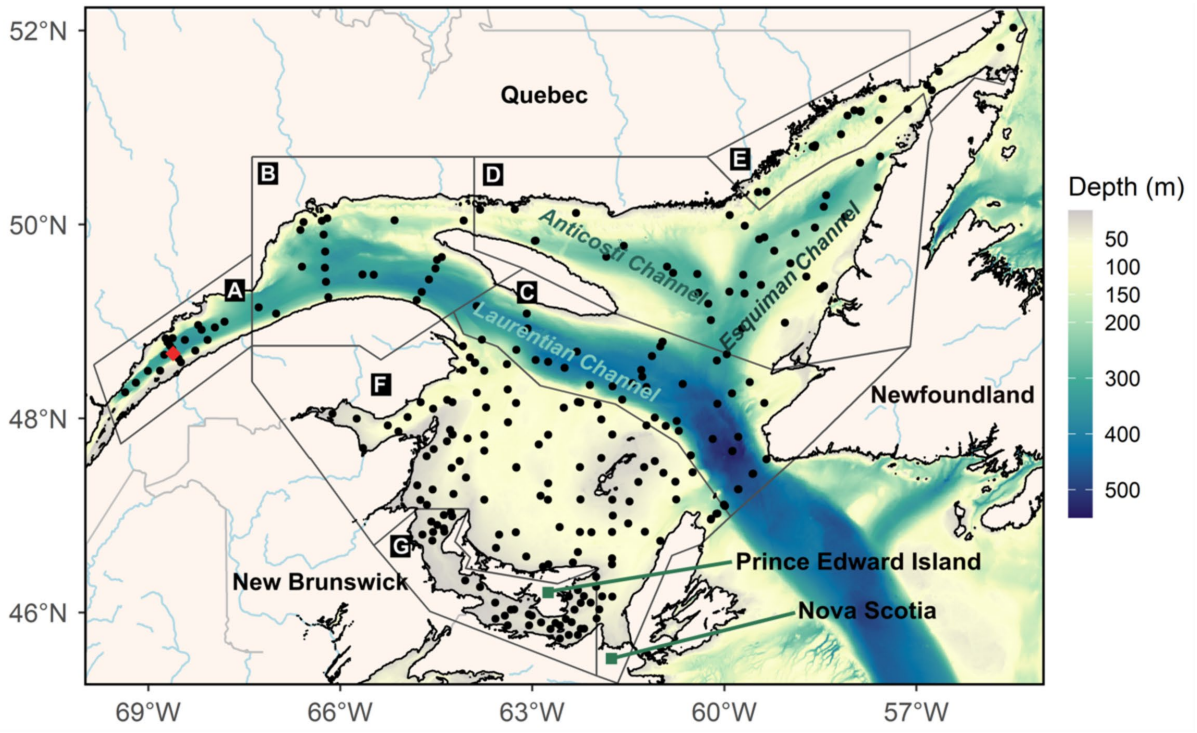


Figure 1: Bathymetric map of the Estuary and Gulf of St. Lawrence showing location of standard stations (black dots) and the high-frequency monitoring station of Rimouski (red diamond) sampled in 2025. The regional divisions can be identified as (A) Estuary, (B) Northwest Gulf, (C) Centre Gulf and Cabot Strait, (D) Northeast Gulf, (E) Mécatina Trough and Strait of Belle Isle, (F) Magdalen Shallows (including Chaleur Bay), and (G) Northumberland Strait.

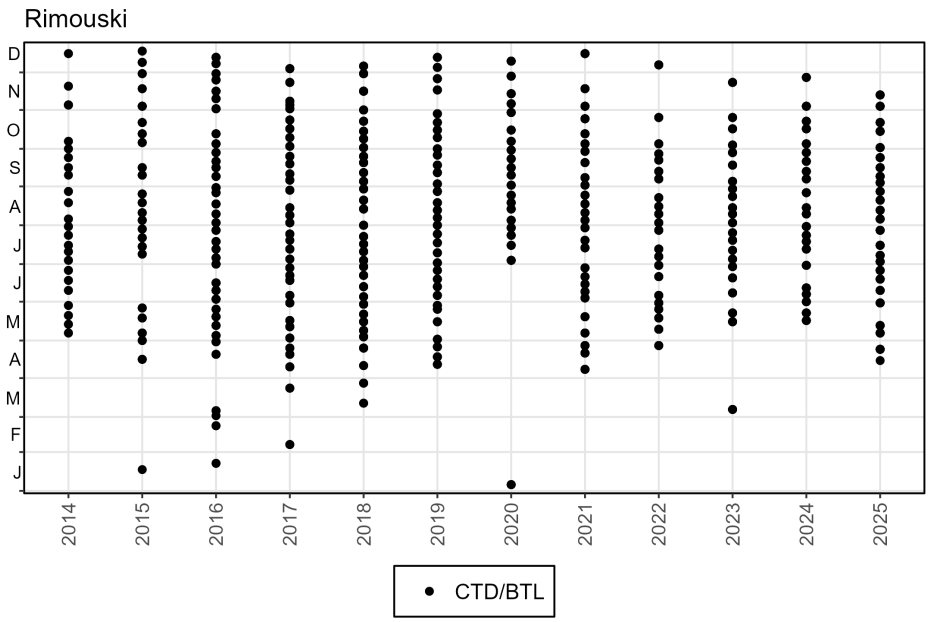


Figure 2: Annual sampling date distributions at Rimouski station: months, from January (J) to December (D) appear on the y-axis while years, from 2014 to 2025, appear on the x-axis. The term CTD refers to Conductivity-Temperature-Depth probe deployment, and the term BTL refers to bottle sampling.

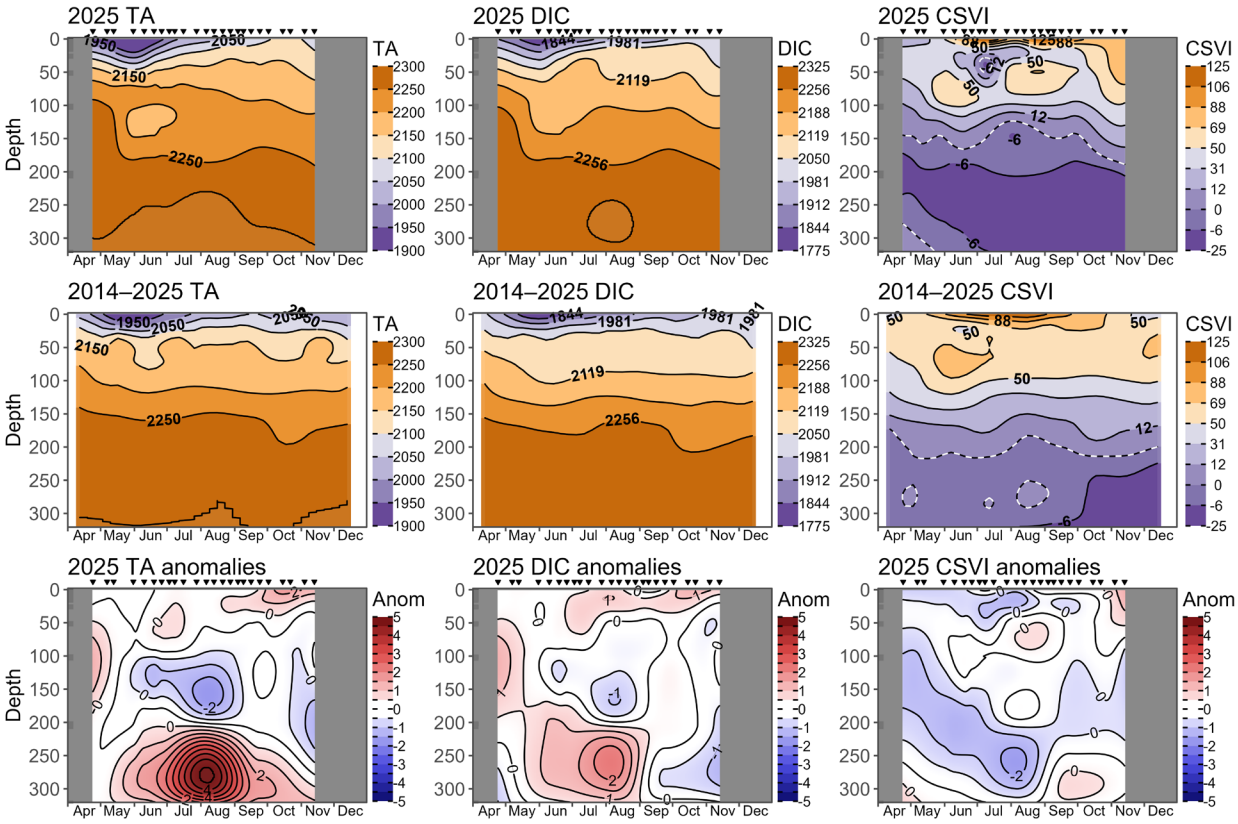


Figure 3: Vertical profiles of total alkalinity (TA in µmol kg^{-1}, left column); dissolved inorganic carbon (DIC in µmol kg^{-1}, middle column), and the carbonate system vulnerability index (CSVI = [TA] - [DIC] in µmol kg^{-1}, right column) at Rimouski station in 2025 (upper row), climatology 2014–2025 (middle row) and normalized anomalies (bottom row). Anomaly colours convey both the direction and magnitude of deviations: white indicates normal values within ±½ standard deviation (SD) of the climatological mean, red denotes above-normal anomalies, and blue reflects below-normal anomalies. The dotted line indicates the threshold where TA = DIC ([TA] - [DIC] = 0). Station occupation dates are indicated by black triangles. Months appear on the x-axis, starting from April (Apr) and ending in December (Dec).

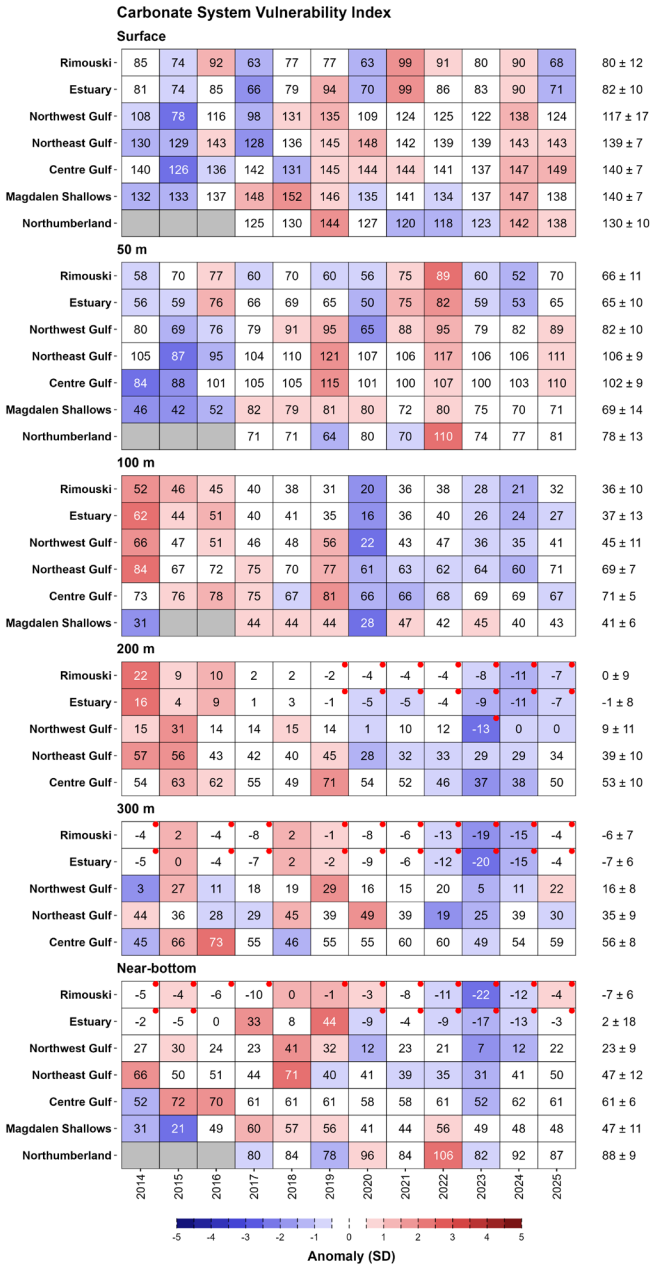


Figure 4: Time series of annual anomalies in the carbonate system vulnerability index (CSVI = [TA] - [DIC], expressed in µmol kg^{-1}) from 2014 to 2025, calculated at six depths: surface, 50 m, 100 m, 200 m, 300 m, and near-bottom. The boxed values indicate annual CSVI averages, while the numbers aligned on the right represent the climatological means and standard deviations (SD) calculated over the period 2014–2025. Cell colours convey the direction and magnitude of anomalies: white cells indicate values within ± ½ SD of the climatological mean, red cells denote above-normal anomalies, and blue cells reflect below-normal anomalies. Grey cells mark insufficient or missing data. To enhance legibility, white text is used within cells where anomalies exceed ± 2 SD. Tiles showcasing a red circle identify years in which the annual average CSVI fell below the threshold of 0 µmol kg^{-1}.

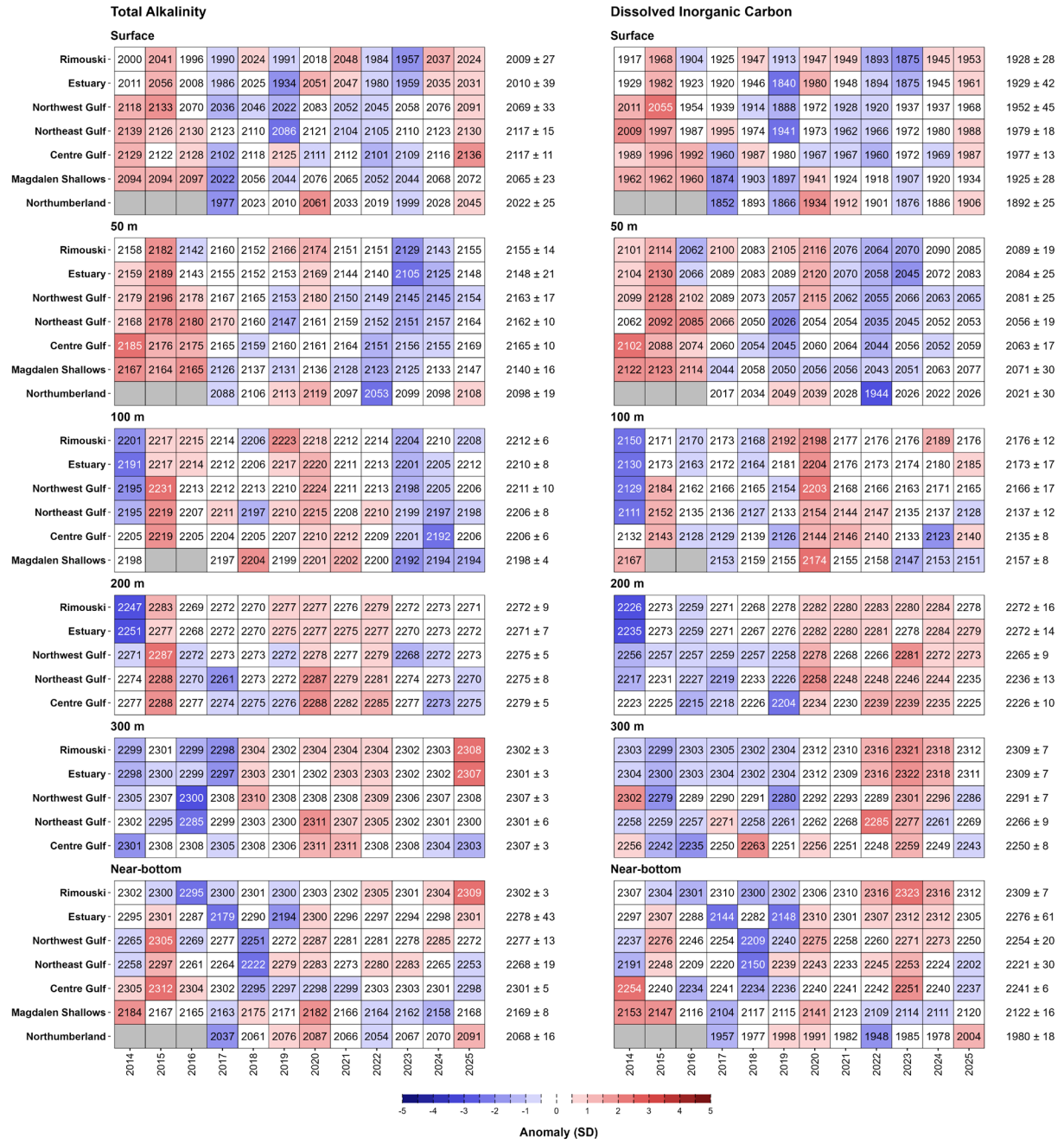


Figure 5: Time series of annual anomalies in total alkalinity (TA, left panel, expressed in µmol kg^{-1}), and dissolved inorganic carbon (DIC, right panel, expressed in µmol kg^{-1}) from 2014 to 2025, measured at six depths: surface, 50 m, 100 m, 200 m, 300 m, and bottom. The boxed values indicate annual TA or DIC averages, while the numbers aligned on the right represent the climatological means and standard deviations (SD) calculated over the period 2014–2025. Cell colours convey the direction and magnitude of anomalies: white cells indicate values within ± ½ SD of the climatological mean, red cells denote above-normal anomalies, and blue cells reflect below-normal anomalies. Grey cells mark insufficient or missing data. To enhance legibility, white text is used within cells where anomalies exceed ± 2 SD.

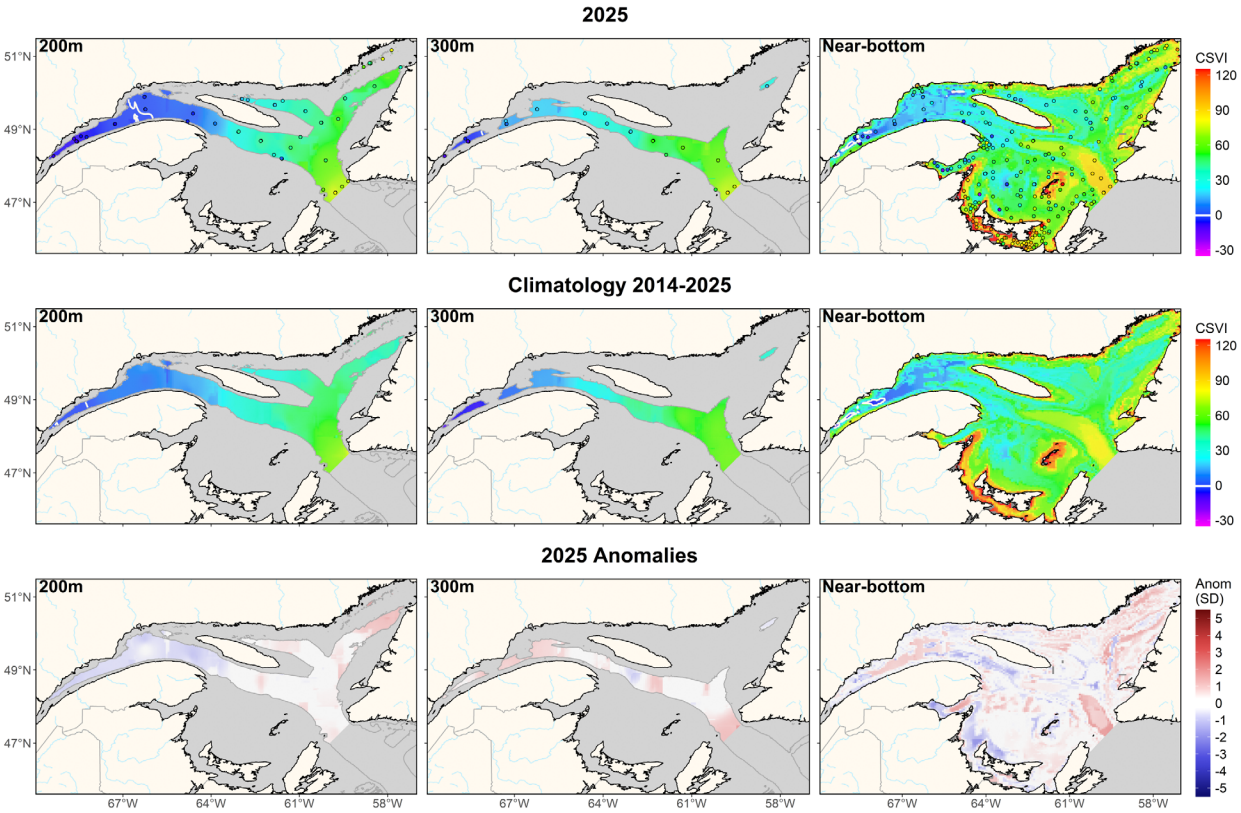


Figure 6: Annual average distribution of carbonate system vulnerability index (CSVI in µmol kg^{-1}) at depths of 200 m and 300 m, and at the bottom in the Estuary and Gulf of St. Lawrence during 2025 (upper panels). The climatology (2014–2025; middle panels) and anomalies (lower panels) are also shown. In the bottom panels, anomaly colours convey both the direction and magnitude of deviations: white indicates normal values within ± ½ standard deviation (SD) of the climatological mean, red denotes above-normal anomalies, and blue reflects below-normal anomalies. The white contour line identifies a threshold of zero (0). Open circles (upper panel) show station locations in 2025.

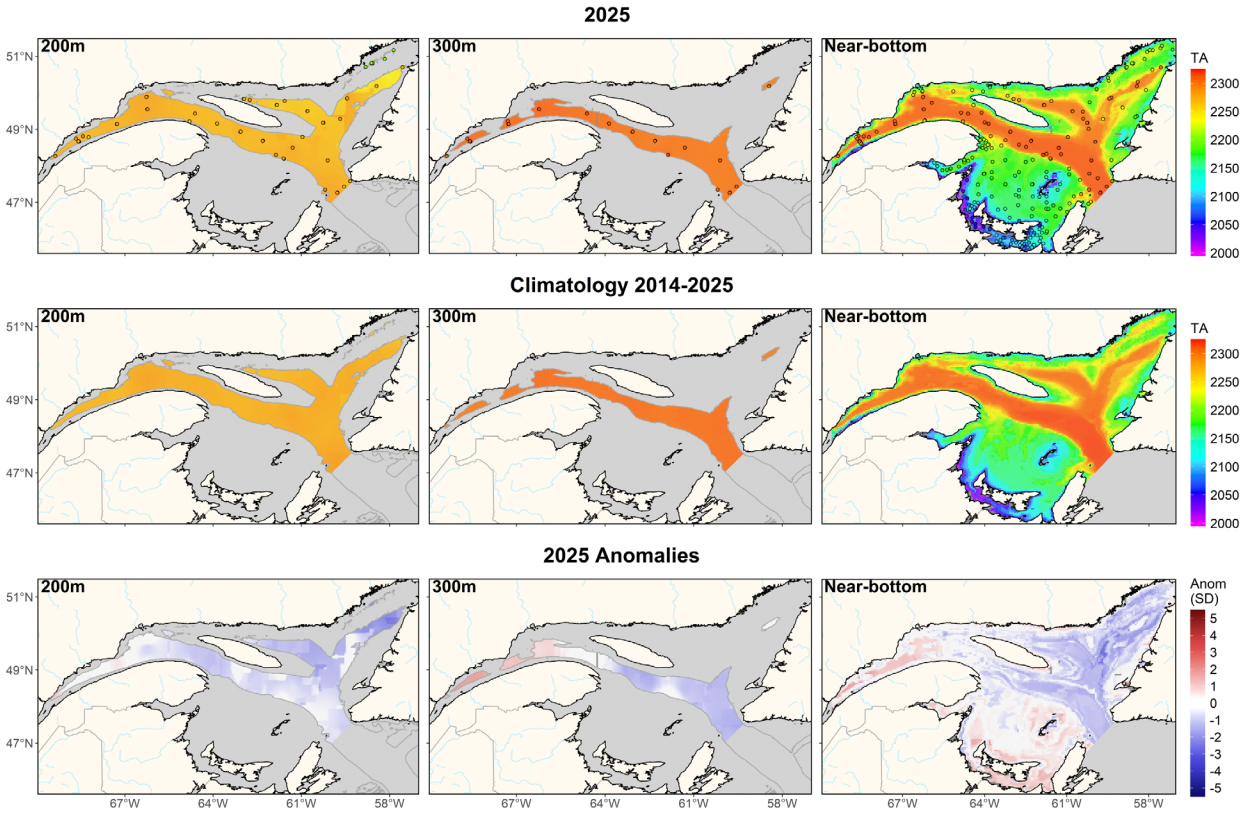


Figure 7: Annual average distribution of total alkalinity (TA in µmol kg^{-1}) at depths of 200 m and 300 m, and at the bottom in the Estuary and Gulf of St. Lawrence during 2025 (upper panels). The climatology (2014–2025; middle panels) and anomalies (lower panels) are also shown. In the bottom panels, anomaly colours convey both the direction and magnitude of deviations: white indicates normal values within ± ½ standard deviation (SD) of the climatological mean, red denotes above-normal anomalies, and blue reflects below-normal anomalies. Open circles (upper panel) show station locations in 2025.

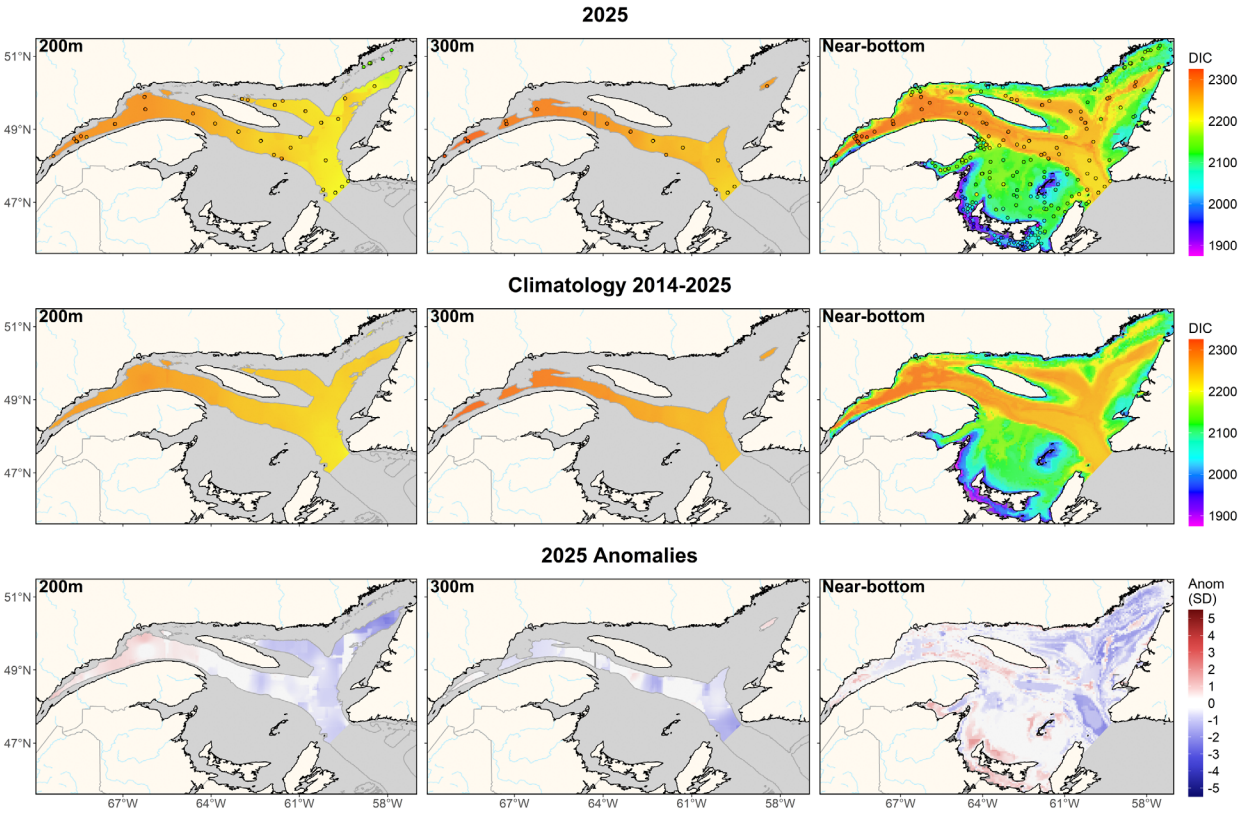


Figure 8: Annual average distribution of dissolved inorganic carbon (DIC in µmol kg^{-1}) at depths of 200 m and 300 m, and at the bottom in the Estuary and Gulf of St. Lawrence during 2025 (upper panels). The climatology (2014–2025; middle panels) and anomalies (lower panels) are also shown. In the bottom panels, anomaly colours convey both the direction and magnitude of deviations: white indicates normal values within ± ½ standard deviation (SD) of the climatological mean, red denotes above-normal anomalies, and blue reflects below-normal anomalies. Open circles (upper panel) show station locations in 2025.

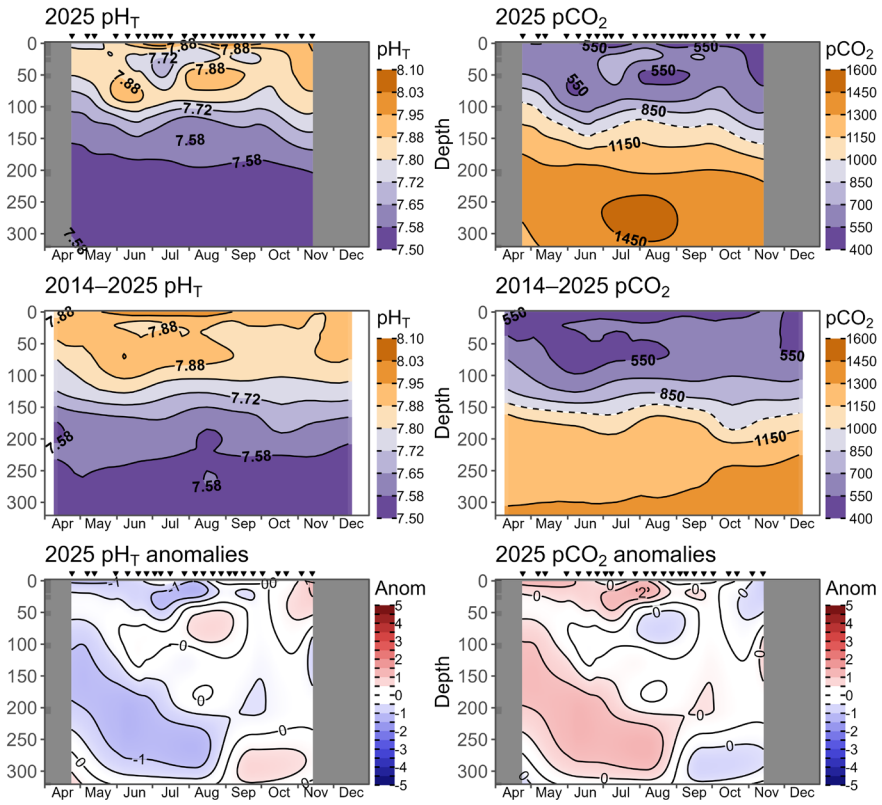


Figure 9: Vertical profiles of pH_T (pH on the total scale; left panels) and partial pressure of CO_2 (pCO_2 in µatm, right panels) at Rimouski station in 2025 (upper panels), climatology 2014–2025 (middle panels) and normalized anomalies (bottom panels). Anomaly colours convey both the direction and magnitude of deviations: white indicates normal values within ± ½ standard deviation (SD) of the climatological mean, red denotes above-normal anomalies, and blue reflects below-normal anomalies. The dotted line in pCO_2 panels indicates the hypercapnic threshold of 1000 µatm. Station occupation dates are indicated by black triangles. Months appear on the x-axis, starting from April (Apr) and ending in December (Dec).

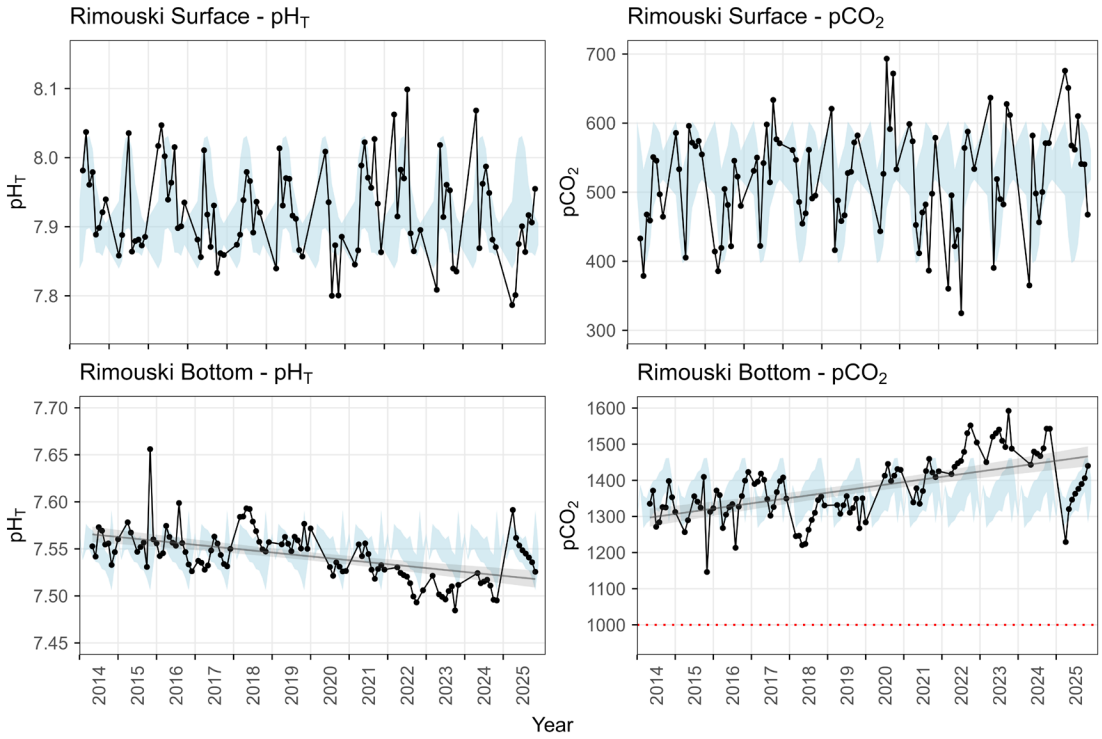


Figure 10: Time series of the monthly average pH on the total scale (pH_T; left panels) and partial pressure of CO_2 (pCO_2 in µatm, right panels) at Rimouski station in surface waters (top 0–15 m, upper panels), and in near-bottom waters (270–320 m, bottom panels). The blue shaded area on each panel indicates the respective monthly climatology for the 2014–2025 period. Note the different ranges in scales for pCO_2 and pH_T in different depth panels. Grey lines on the bottom panels represent ordinary least squares (OLS) regression trends with shaded 95 % confidence intervals. The dotted red line in the near-bottom pCO_2 panel indicates the hypercapnic threshold of 1000 µatm.

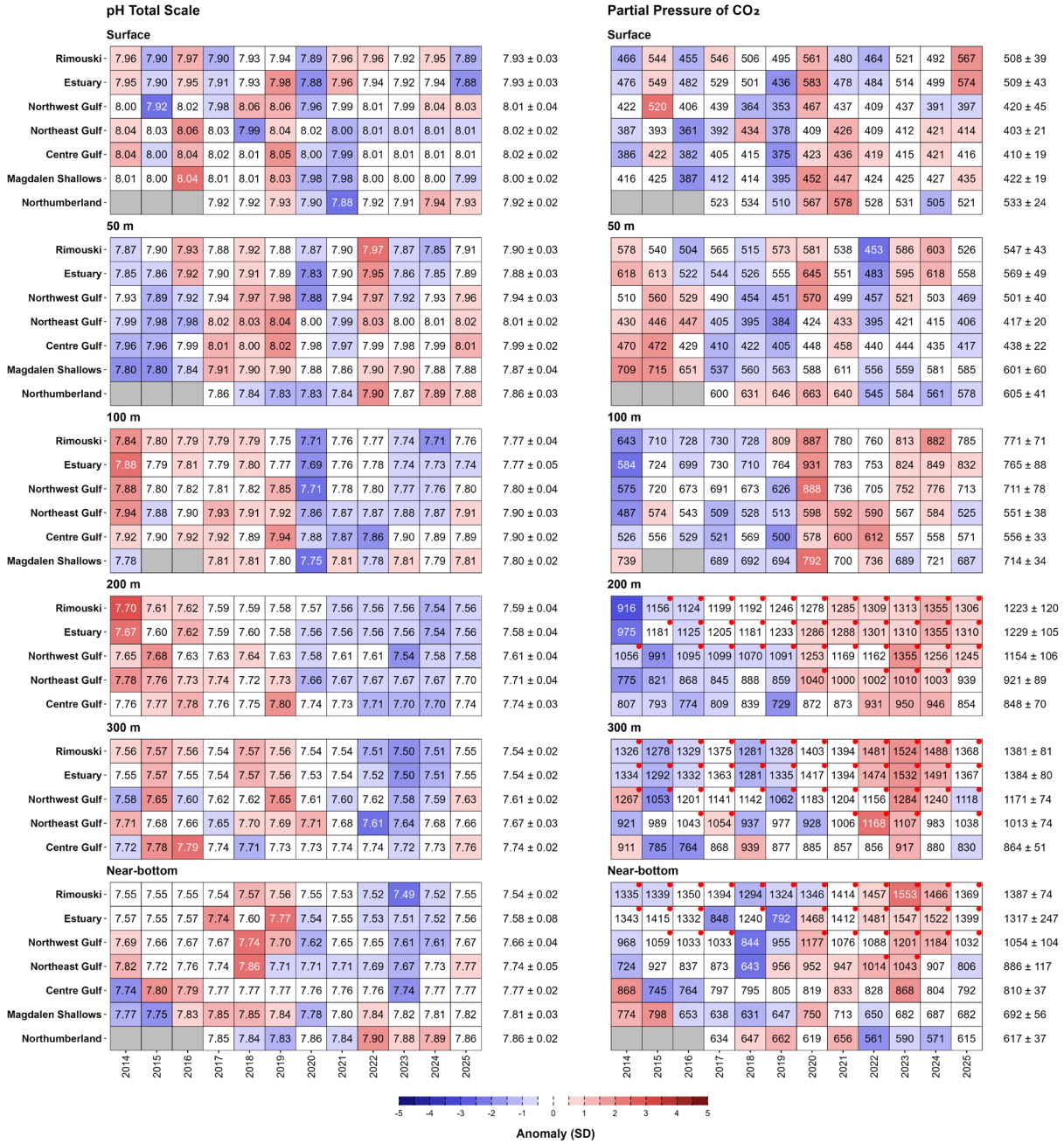


Figure 11: Time series of annual anomalies in pH expressed on the total scale (left panel; pH_T) and partial pressure of CO_2 expressed in µatm (right panel; pCO_2) from 2014 to 2025, respectively measured and calculated at six depths: surface, 50 m, 100 m, 200 m, 300 m, and bottom. The boxed values indicate annual pH_T or pCO_2 averages, while the numbers aligned on the right represent the climatological means and standard deviations (SD) calculated over the period 2014–2025. Cell colours convey the direction and magnitude of anomalies: white cells indicate values within ± ½ SD of the climatological mean, red cells denote above-normal anomalies, and blue cells reflect below-normal anomalies. Grey cells mark insufficient or missing data. To enhance legibility, white text is used within cells where anomalies exceed ± 2 SD. Tiles showcasing a red circle identify years in which the annual average pCO_2 was above the threshold of 1000 µatm.

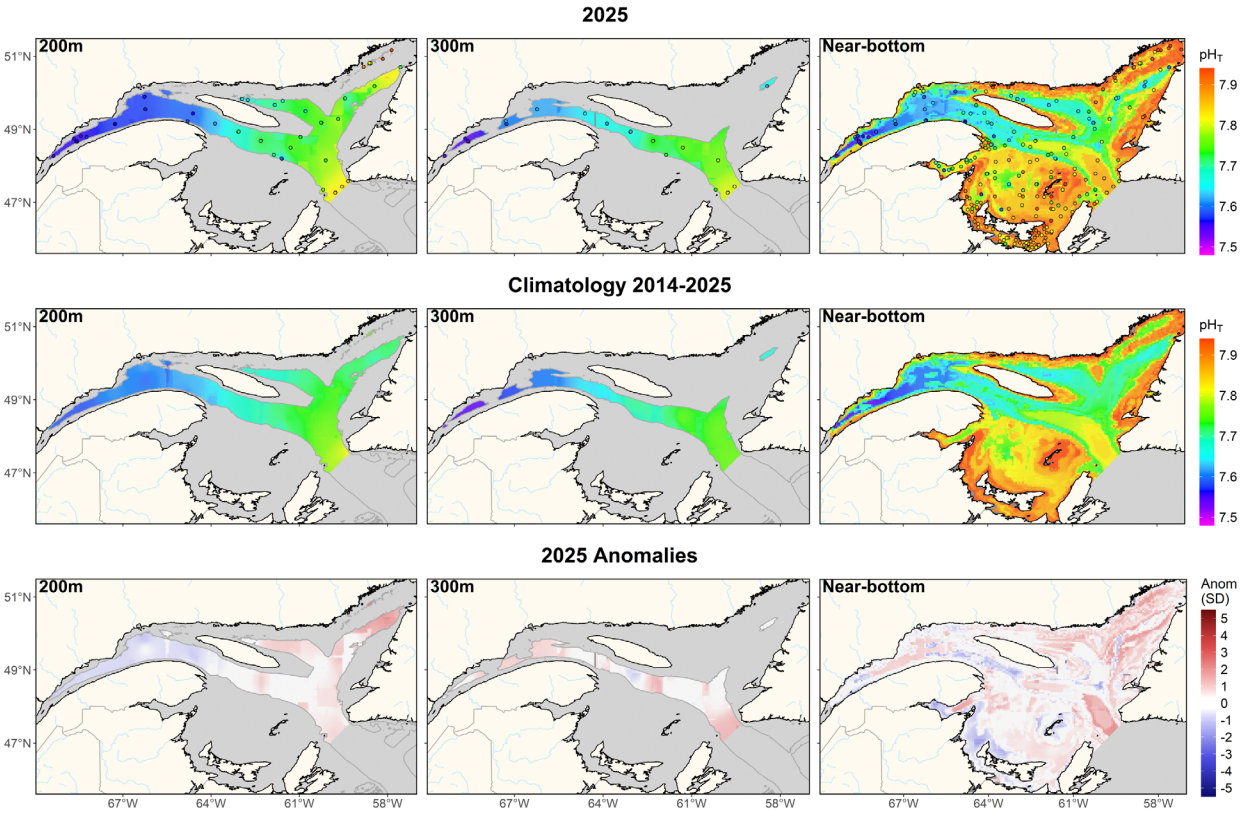


Figure 12: Annual average distribution of in situ pH_T (pH on the total scale) at depths of 200 m and 300 m, and at the bottom in the Estuary and Gulf of St. Lawrence during 2025 (upper panels). The climatology (2014–2025; middle panels) and anomalies (lower panels) are also shown. In the bottom panels, anomaly colours convey both the direction and magnitude of deviations: white indicates normal values within ± ½ standard deviation (SD) of the climatological mean, red denotes above-normal anomalies, and blue reflects below-normal anomalies. Open circles (upper panels) show station locations in 2025.

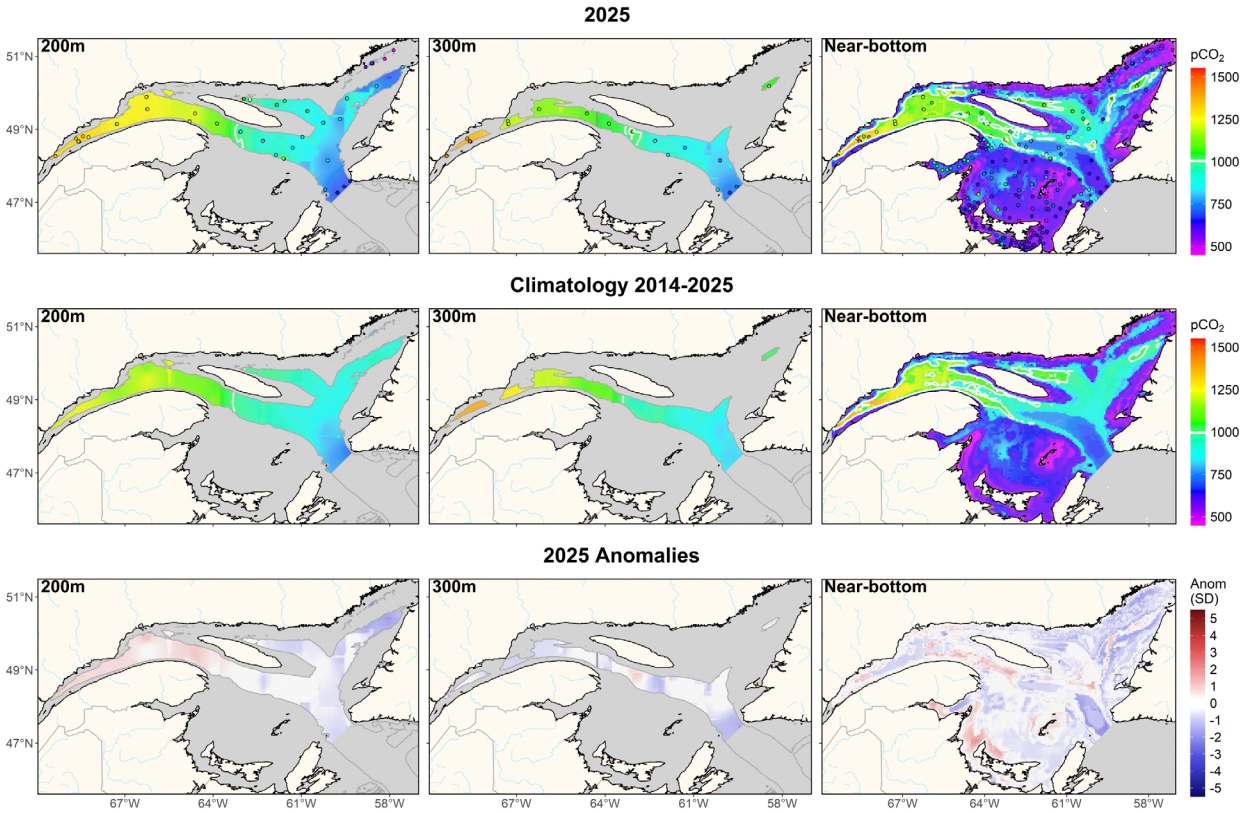


Figure 13: Annual average distribution of partial pressure of CO_2 (pCO_2 in µatm) at the surface, at depths of 200 m and 300 m, and at the bottom in the Estuary and Gulf of St. Lawrence during 2025 (upper panels). The climatology (2014–2025; middle panels) and anomalies (lower panels) are also shown. The white contour line identifies hypercapnic areas ($pCO_2 \geq 1000$ µatm). In the bottom panels, anomaly colours convey both the direction and magnitude of deviations: white indicates normal values within ± ½ standard deviation (SD) of the climatological mean, red denotes above-normal anomalies, and blue reflects below-normal anomalies. Open circles (upper panel) show station locations in 2025.

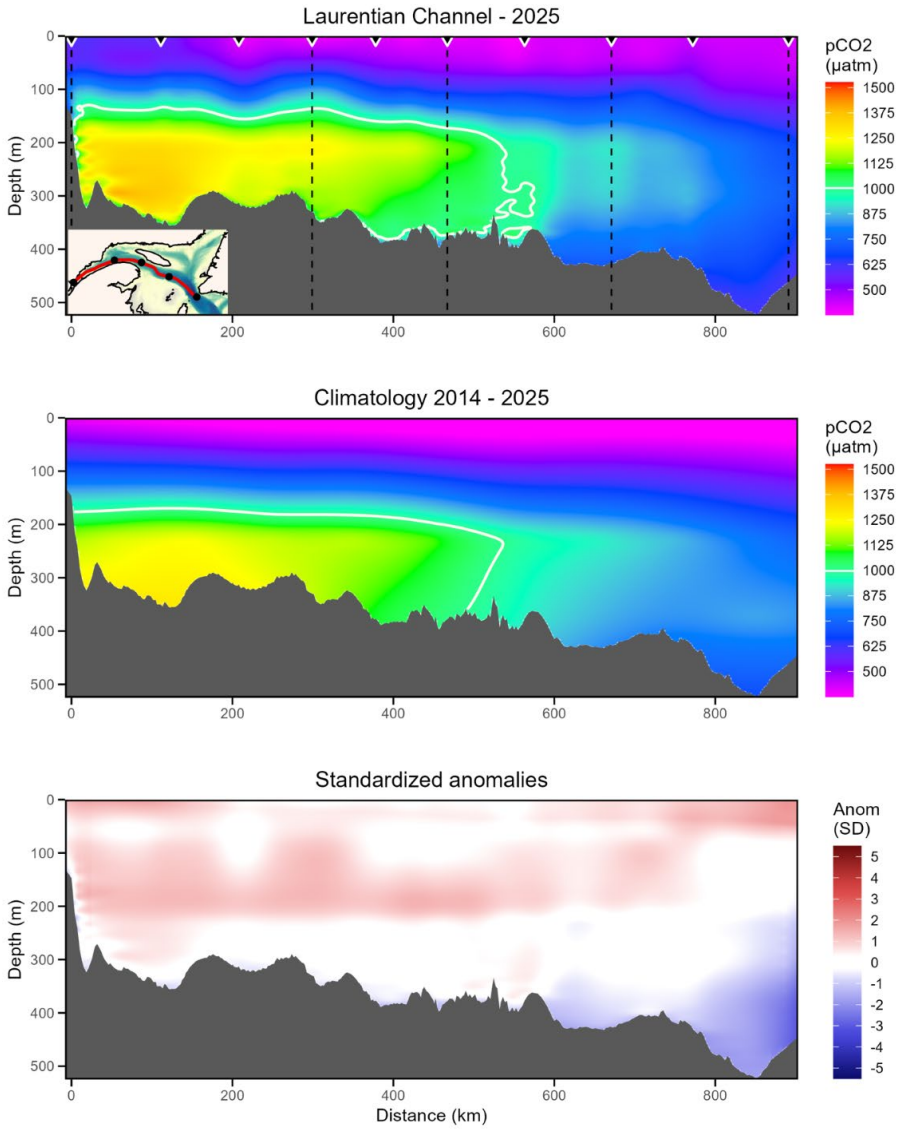


Figure 14: Mean annual vertical distribution of pCO_2 along the Laurentian Channel in 2025 (upper panel) and for climatology (2014–2025; middle panel). Anomaly colours convey both the direction and magnitude of deviations: white indicates normal values within ± ½ standard deviation (SD) of the climatological mean, red denotes above-normal anomalies, and blue reflects below-normal anomalies. The section is presented from the head of the Laurentian Channel (Estuary) to Cabot Strait. Black triangles mark station positions in the upper panel. Dashed vertical lines align with geographic markers shown as black dots on the inset map in the lower-left corner, where only a subset of stations is displayed to avoid masking the transect line.

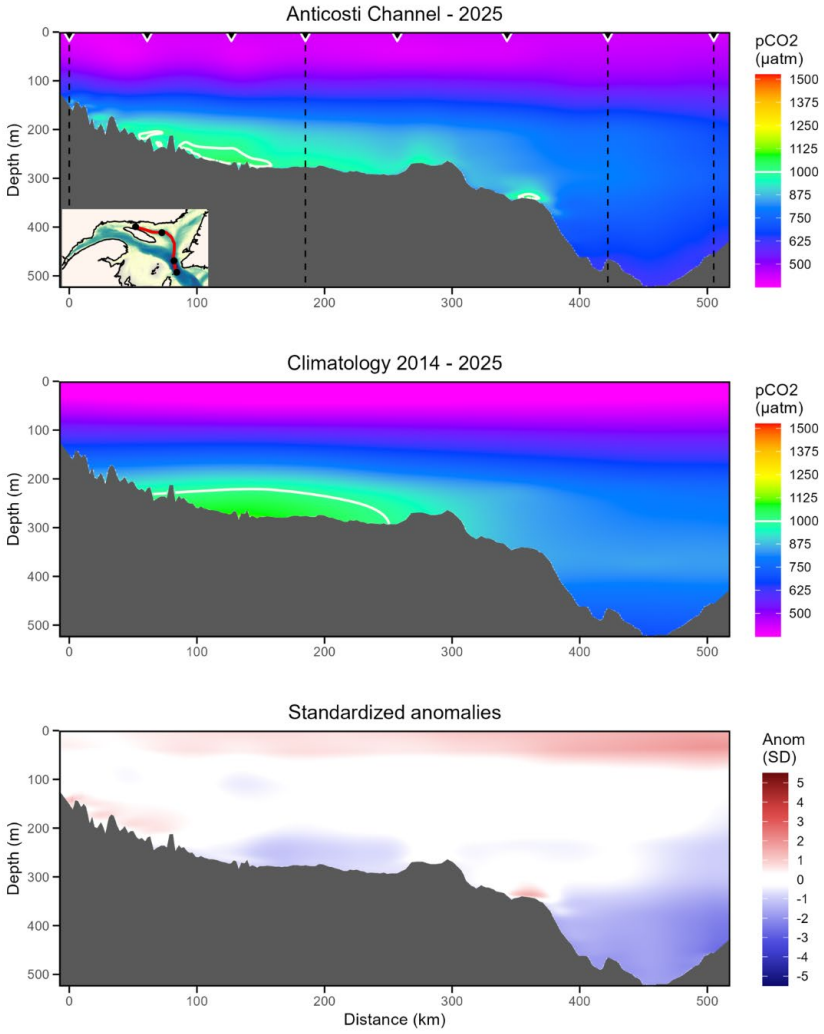


Figure 15: Mean annual vertical distribution of pCO_2 along the Anticosti Channel in 2025 (upper panel) and for climatology (2014–2025; middle panel). Anomaly colours convey both the direction and magnitude of deviations: white indicates normal values within ± ½ standard deviation (SD) of the climatological mean, red denotes above-normal anomalies, and blue reflects below-normal anomalies. The section is presented from the head of the Anticosti Channel to Cabot Strait. Black triangles mark station positions in the upper panel. Dashed vertical lines align with geographic markers shown as black dots on the inset map in the lower-left corner, where only a subset of stations is displayed to avoid masking the transect line.

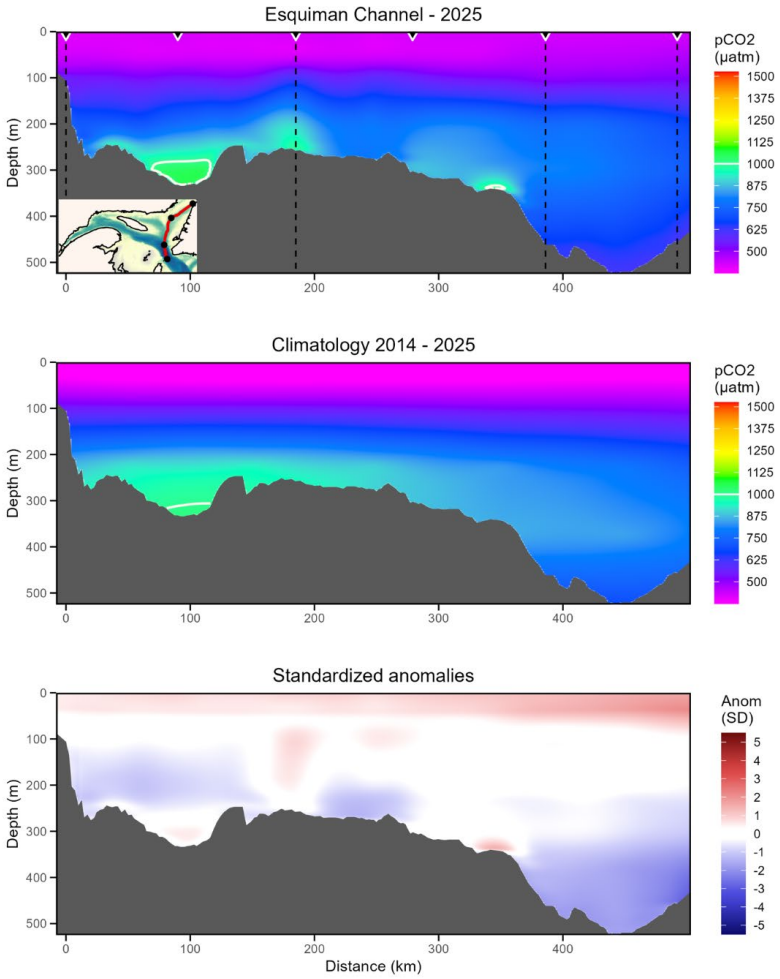


Figure 16: Mean annual vertical distribution of pCO_2 along the Esquiman Channel in 2025 (upper panel) and for climatology (2014–2025; middle panel). Anomaly colours convey both the direction and magnitude of deviations: white indicates normal values within ± ½ standard deviation (SD) of the climatological mean, red denotes above-normal anomalies, and blue reflects below-normal anomalies. The section is presented from the head of the Esquiman Channel to Cabot Strait. Black triangles mark station positions in the upper panel. Dashed vertical lines align with geographic markers shown as black dots on the inset map in the lower-left corner, where only a subset of stations is displayed to avoid masking the transect line.

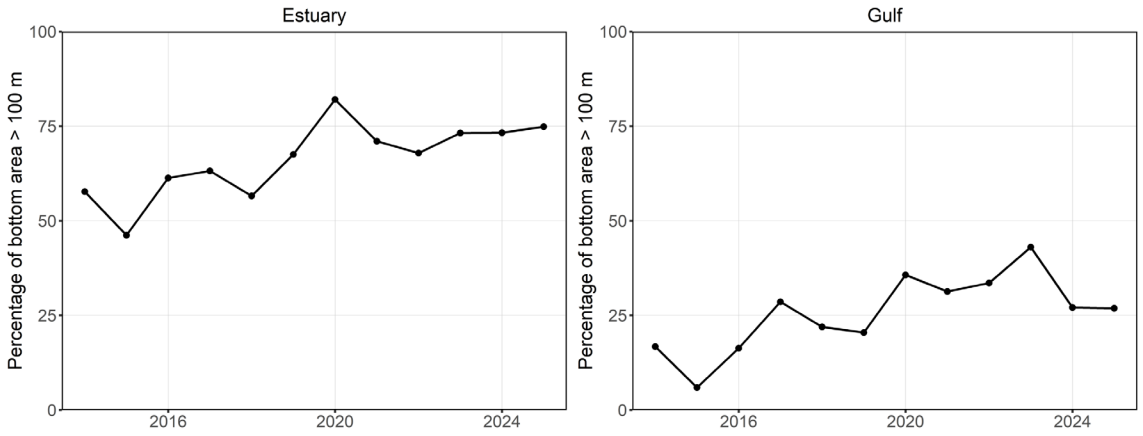


Figure 17: Percentage (%) of the bottom area where waters deeper than 100 m is covered by hypercapnic waters (pCO_2 ≥ 1000 µatm) in the Estuary (left panel) and the Gulf (right panel) of St. Lawrence.

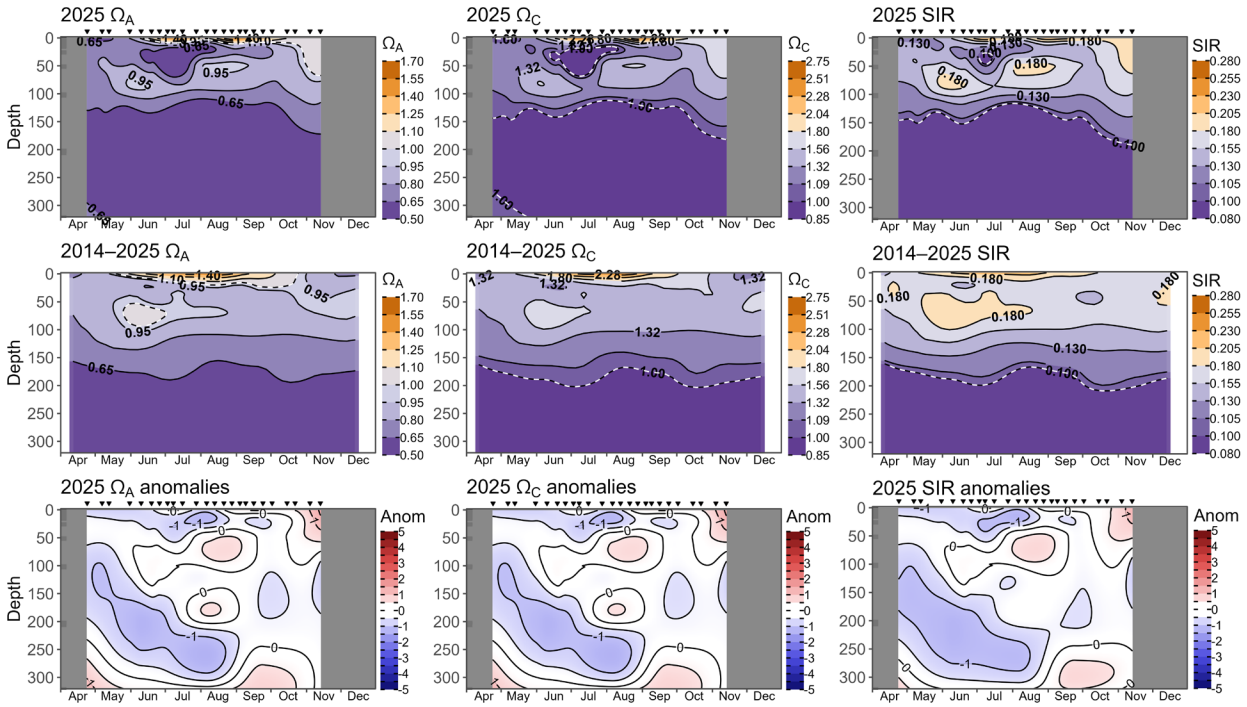


Figure 18: Vertical profiles of saturation state of aragonite (Ω_A; unitless; left panels) and calcite (Ω_C; unitless; middle panels), and the substrate-inhibitor ratio (SIR in mol µmol^{-1}) at Rimouski station in 2025 (upper panels), climatology 2014–2025 (middle panels) and normalized anomalies (bottom panels). Anomaly colours convey both the direction and magnitude of deviations: white indicates normal values within ±½ standard deviation (SD) of the climatological mean, red denotes above-normal anomalies, and blue reflects below-normal anomalies. The dotted lines in panels indicate the critical thresholds of 1 for Ω_A and Ω_C. Note the different ranges in mineral saturation values for aragonite and calcite. Station occupation dates are indicated by black triangles. Months appear on the x-axis, starting from April (Apr) and ending in December (Dec).

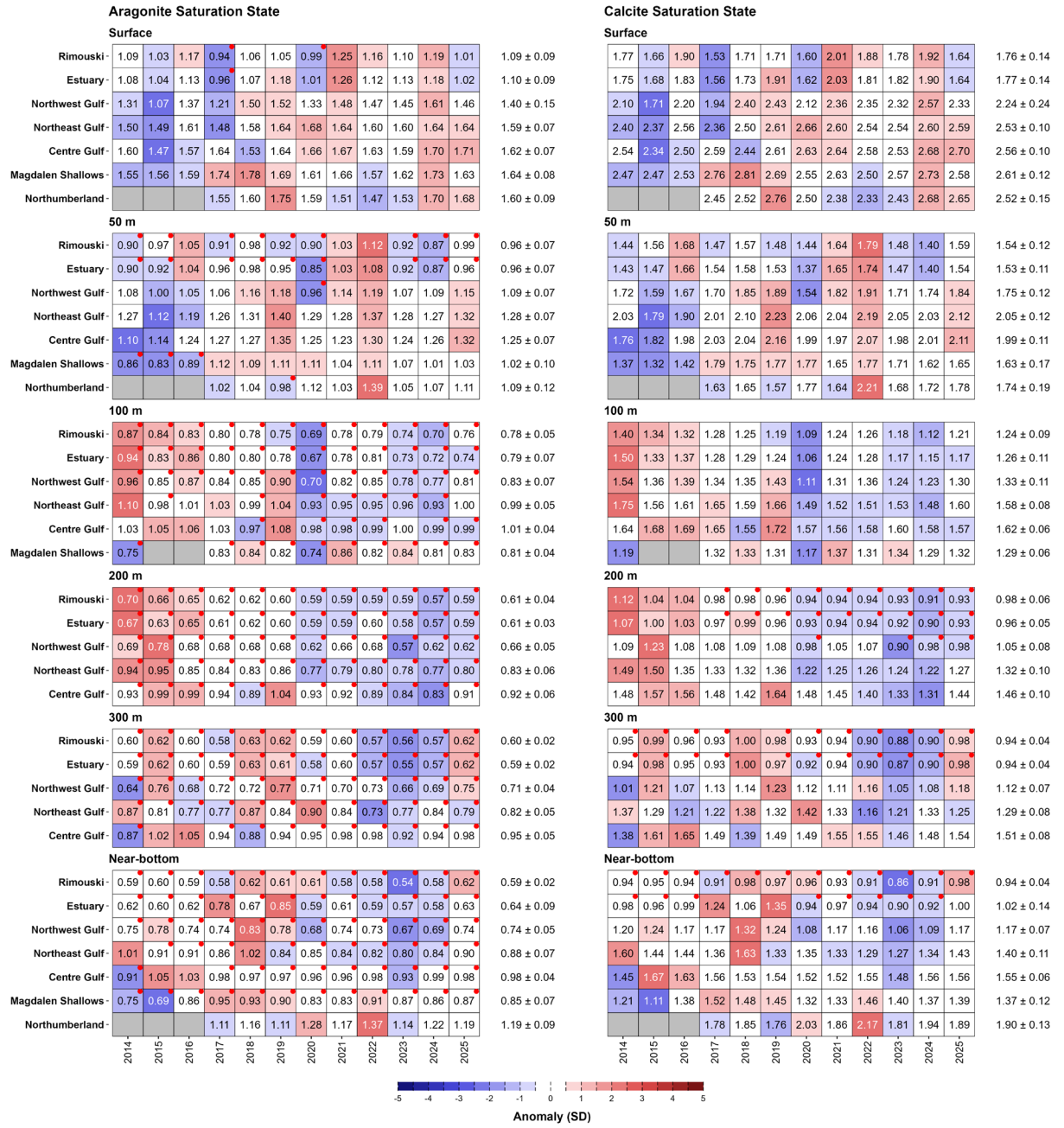


Figure 19: Time series of annual anomalies in saturation states for aragonite (Ω_A; unitless; left panel), and calcite (Ω_C; unitless; right panel), calculated from 2014 to 2025 at six depths: surface, 50 m, 100 m, 200 m, 300 m, and bottom. The boxed values indicate annual Ω_A or Ω_C averages, while the numbers aligned on the right represent the climatological means and standard deviations (SD) calculated over the period 2014–2025. Cell colours convey the direction and magnitude of anomalies: white cells indicate values within ± ½ SD of the climatological mean, red cells denote above-normal anomalies, and blue cells reflect below-normal anomalies. Grey cells mark insufficient or missing data. To enhance legibility, white text is used within cells where anomalies exceed ± 2 SD. Tiles showcasing a red circle identify years in which the annual average Ω_A or Ω_C fell below the threshold of 1.

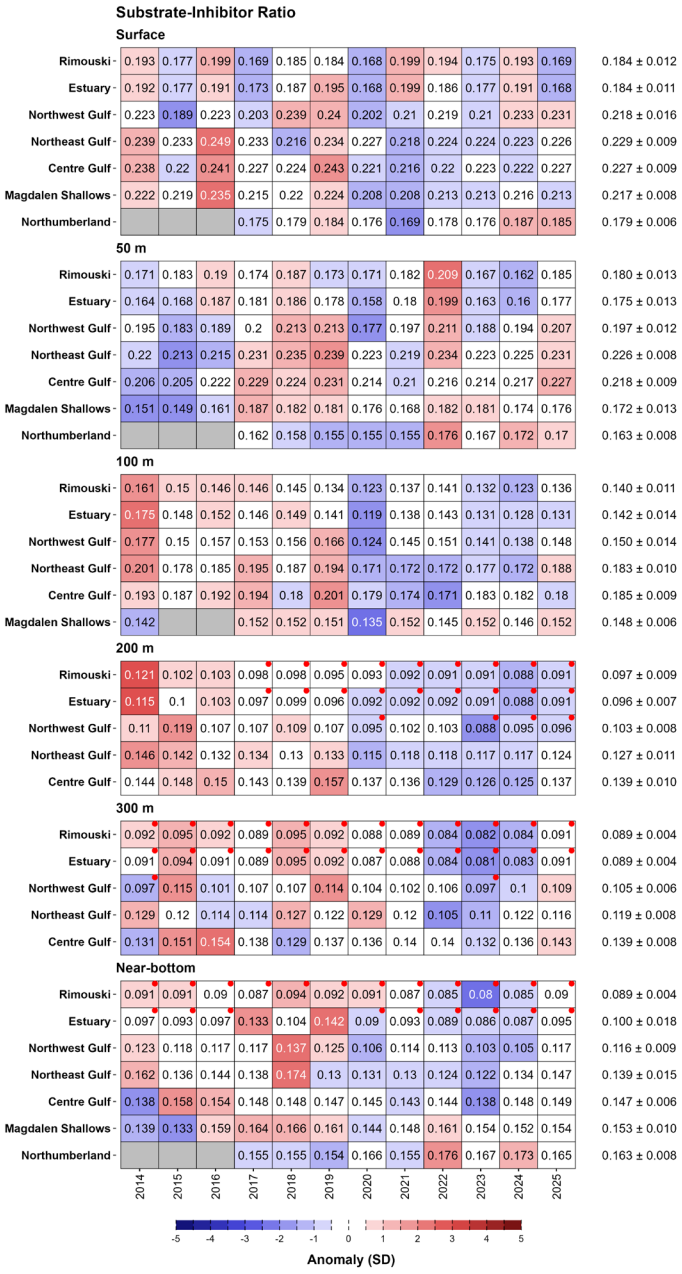


Figure 20: Time series of annual anomalies in the substrate-inhibitor ratio (SIR; expressed in mol μmol^{-1}) from 2014 to 2025, calculated at six depths: surface, 50 m, 100 m, 200 m, 300 m, and bottom. The boxed values indicate annual SIR averages, while the numbers aligned on the right represent the climatological means and standard deviations (SD) calculated over the period 2014–2025. Cell colours convey the direction and magnitude of anomalies: white cells indicate values within ± ½ SD of the climatological mean, red cells denote above-normal anomalies, and blue cells reflect below-normal anomalies. Grey cells mark insufficient or missing data. To enhance legibility, white text is used within cells where anomalies exceed ± 2 SD. Tiles showcasing a red circle identify years in which the annual average SIR fell below the threshold of 0.100.

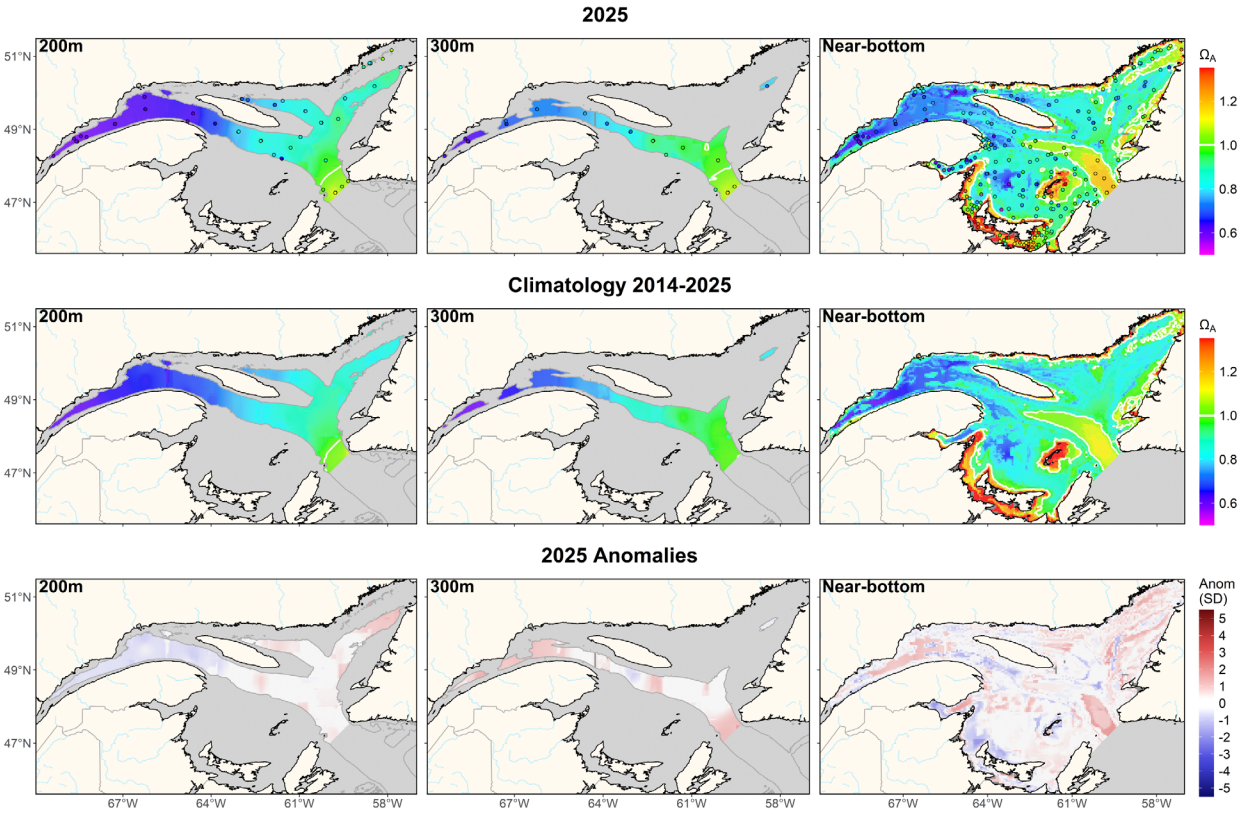


Figure 21: Annual average distribution of the saturation state of aragonite (Ω_A; unitless) at depths of 200 m and 300 m, and at the bottom in the Estuary and Gulf of St. Lawrence during 2025 (upper panels). The climatology (2014–2025; middle panels) and anomalies (lower panels) are also shown. In the bottom panels, anomaly colours convey both the direction and magnitude of deviations: white indicates normal values within ± ½ standard deviation (SD) of the climatological mean, red denotes above-normal anomalies, and blue reflects below-normal anomalies. The white contour line identifies a threshold of 1. Open circles (upper panels) show station locations in 2025.

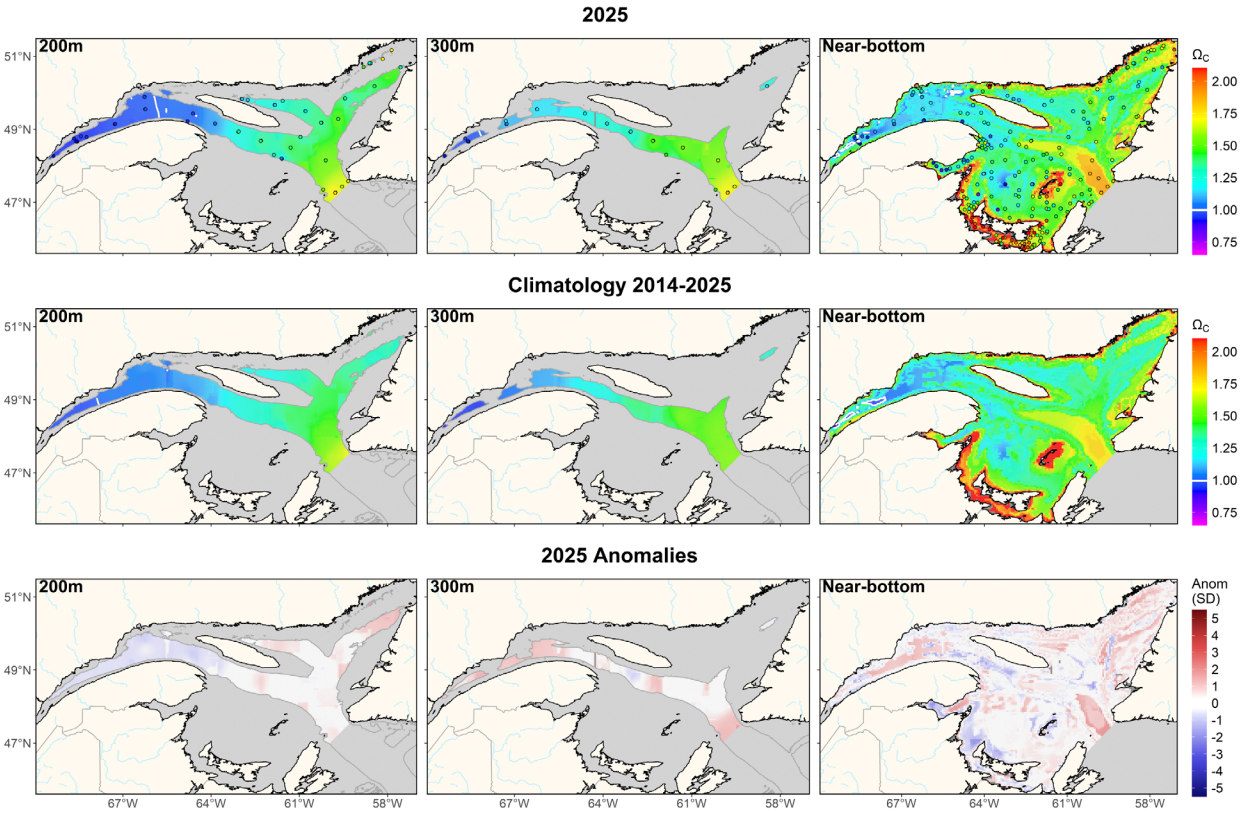


Figure 22: Annual average distribution of the saturation state of calcite (Ω_C; unitless) at depths of 200 m and 300 m, and at the bottom in the Estuary and Gulf of St. Lawrence during 2025 (upper panel). The climatology (2014–2025; middle panel) and anomalies (lower panel) are also shown. In the bottom panels, anomaly colours convey both the direction and magnitude of deviations: white indicates normal values within ± ½ standard deviation (SD) of the climatological mean, red denotes above-normal anomalies, and blue reflects below-normal anomalies. The white contour line identifies a threshold of 1. Open circles (upper panel) show station locations in 2025.

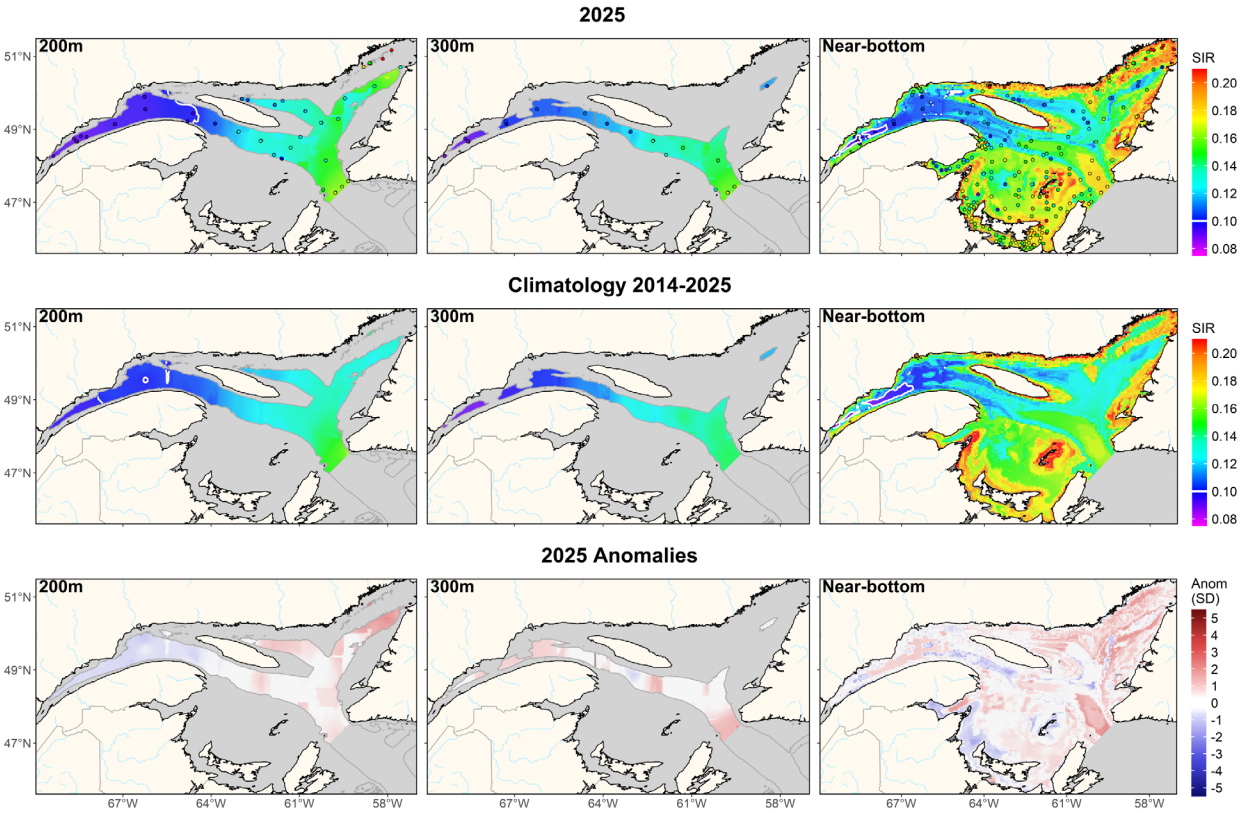


Figure 23: Annual average distribution of the substrate-inhibitor ratio (SIR in mol μmol^{-1}) at depths of 200 m and 300 m, and at the bottom in the Estuary and Gulf of St. Lawrence during 2025 (upper panel). The climatology (2014–2025; middle panel) and anomalies (lower panel) are also shown. In the bottom panels, anomaly colours convey both the direction and magnitude of deviations: white indicates normal values within ± ½ standard deviation (SD) of the climatological mean, red denotes above-normal anomalies, and blue reflects below-normal anomalies. The white contour line identifies a threshold of 0.100. Open circles (upper panel) show station locations in 2025.

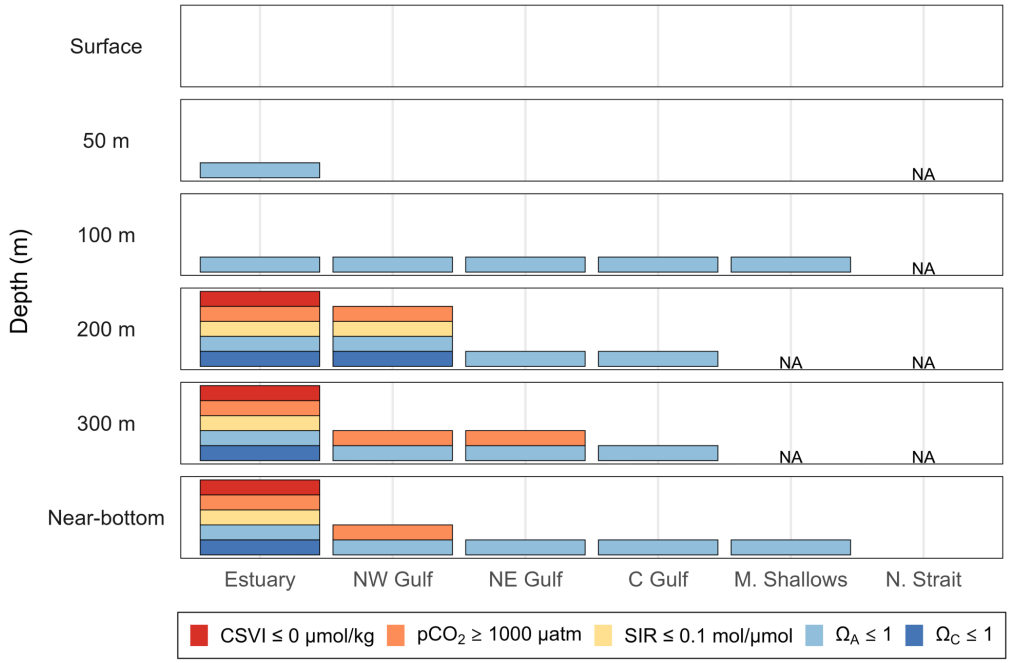


Figure 24: Cumulative CO_2-driven stressor index for 2025, illustrating observations reaching or exceeding the CO_2-related chemical thresholds across the EGSL at different depths. Stacked bars indicate the number of stressors at or beyond the defined threshold (≥ or ≤, depending on the indicator) based on annual mean conditions at each depth. “NA” denotes depths not present within the Magdalen Shallows or Northumberland Strait. CSVI = carbonate system vulnerability index, pCO_2 = partial pressure of CO_2, SIR = substrate-inhibitor ratio, Ω_A = saturation state of aragonite, and Ω_C = saturation state of calcite. Region abbreviations: Estuary = Estuary, Northwest Gulf = NW Gulf, Northeast Gulf = NE Gulf, Centre Gulf = C Gulf, Magdalen Shallows = M. Shallows, and Northumberland Strait = N. Strait.

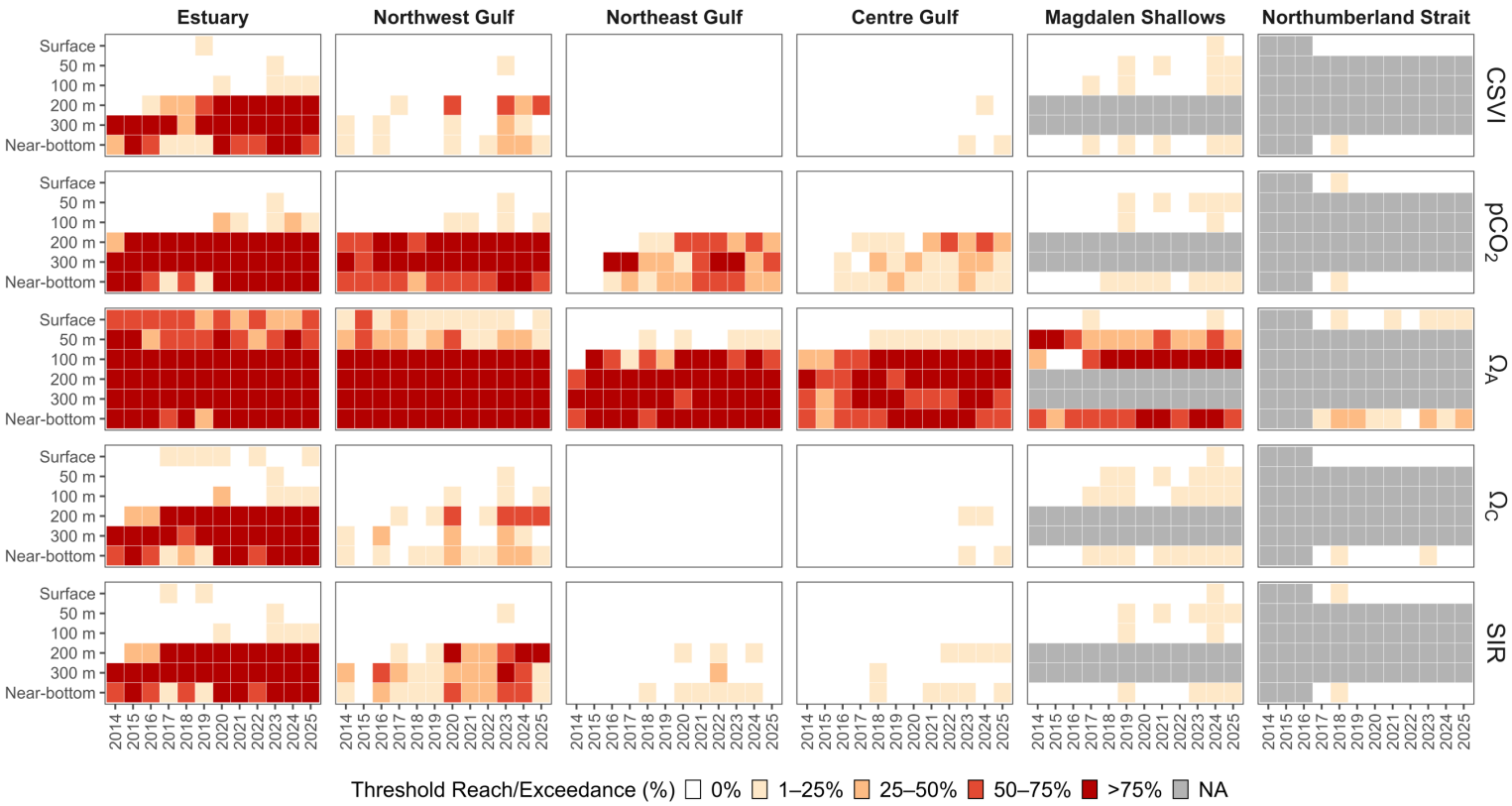


Figure 25: Cumulative frequency of observations meeting CO_2-related chemical thresholds across the EGSL from 2014 to 2025. Each panel shows the percentage (%) of observations at or beyond the defined threshold (≥ or ≤, depending on the indicator) at each depth and year. Rows correspond to stressor indicators: CSVI = carbonate system vulnerability index ≤ 0 µmol/kg, pCO_2 = partial pressure of CO_2 ≥1000 µatm, Ω_A = saturation state of aragonite ≤ 1, and Ω_C = saturation state of calcite ≤ 1, SIR = substrate-inhibitor ratio ≤ 0.100 mol µmol^{-1}. Columns represent the six monitored regions from the Estuary to Northumberland Strait.

APPENDICES

Appendix 1: General linear model results for Rimouski station. The significance (*p*-value) of the year and month effects as well as the adjusted coefficients of determination (R^2) of the regression for carbonate system metrics are presented.

Station	Index	Year (*p*)	Month (*p*)	R^2
Rimouski	TA	0.027	<0.0001	0.46
	DIC	0.039	<0.0001	0.48
	CSVI	0.027	<0.0001	0.52
	pH_T	0.062	0.002	0.32
	pCO_2	0.011	0.002	0.42
	Ω_A	<0.0001	<0.0001	0.62
	Ω_C	<0.001	<0.0001	0.59
	SIR	0.014	0.003	0.34

Appendix 2: General linear model results for EGSL regions. The significance (*p*-value) of the year, season, and station effects as well as the adjusted coefficients of determination (R^2) of the regression for carbonate system metrics are presented.

Region	Index	Year (*p*)	Season (*p*)	Station (*p*)	R^2
Estuary	TA	0.055	<0.0001	<0.0001	0.46
	DIC	0.022	<0.0001	<0.0001	0.32
	CSVI	0.014	<0.0001	<0.0001	0.44
	pH_T	0.013	0.003	0.002	0.20
	pCO_2	0.029	0.002	<0.001	0.19
	Ω_A	<0.0001	<0.0001	<0.0001	0.52
	Ω_C	<0.0001	<0.0001	<0.0001	0.50
	SIR	0.001	0.003	<0.001	0.26
Northwest Gulf	TA	0.053	0.04	<0.0001	0.33
	DIC	0.059	0.008	<0.001	0.25
	CSVI	0.077	0.033	<0.0001	0.21
	pH_T	0.016	<0.0001	<0.0001	0.35
	pCO_2	0.017	<0.0001	<0.0001	0.36
	Ω_A	0.065	0.008	0.007	0.18
	Ω_C	0.061	0.007	0.007	0.19
	SIR	0.054	<0.0001	<0.0001	0.34
Centre Gulf	TA	0.013	0.011	0.001	0.17
	DIC	0.043	0.006	0.101	0.15
	CSVI	0.079	0.011	0.001	0.23
	pH_T	0.075	0.022	0.095	0.13
	pCO_2	0.088	0.027	0.096	0.12
	Ω_A	0.073	0.015	0.012	0.16
	Ω_C	0.077	0.016	0.013	0.15
	SIR	0.077	0.006	0.072	0.14
Northeast Gulf	TA	0.031	0.09	0.006	0.21
	DIC	0.075	0.037	0.013	0.16
	CSVI	0.091	0.024	0.006	0.17
	pH_T	0.086	0.085	0.014	0.12
	pCO_2	0.087	0.083	0.016	0.12
	Ω_A	0.097	0.054	0.031	0.13
	Ω_C	0.095	0.056	0.033	0.12
	SIR	0.071	0.039	0.022	0.13
Magdalen Shallows	TA	0.041	0.018	0.047	0.13
	DIC	0.079	0.028	0.069	0.12
	CSVI	0.024	<0.001	0.087	0.33
	pH_T	<0.0001	<0.0001	0.016	0.66
	pCO_2	<0.0001	<0.0001	0.008	0.71
	Ω_A	0.053	<0.0001	0.012	0.36
	Ω_C	0.058	<0.0001	0.031	0.30
	SIR	<0.0001	<0.0001	0.097	0.66

Northumberland Strait	TA	<0.0001	0.012	0.053	0.29
	DIC	0.001	0.078	0.092	0.19
	CSVI	<0.0001	0.015	0.047	0.26
	pH_T	0.021	0.003	0.014	0.22
	pCO_2	0.017	0.002	0.009	0.28
	Ω_A	0.087	0.073	0.095	0.11
	Ω_C	0.087	0.074	0.097	0.11
	SIR	0.045	0.006	0.002	0.26

Appendix 3: List of acronyms used in this report.

Acronym	Word or series of words
ACCASP	Aquatic Climate Change Adaptation Services Program
AZMP	Atlantic Zone Monitoring Program
Ca^{2+}	Calcium ion
$CaCO_3$	Calcium carbonate
CCGS	Canadian Coast Guard Ship
CI	Confidence Interval
CIL	Cold Intermediate Layer
CO_2	Carbon dioxide
CO_3^{2-}	Carbonate ion
CRM	Certified Reference Material
CSVI	Carbonate system vulnerability index
CTD	Conductivity-Temperature-Depth
DFO	Department of Fisheries and Oceans Canada
DIC	Dissolved inorganic carbon
DOM	Dissolved organic matter
EEA	European Environment Agency
EGSL	Estuary and Gulf of St. Lawrence
GLM	General linear model
H^+	Hydrogen ion
H_2CO_3	Carbonic acid
HCO_3^-	Bicarbonate ion
IDW	Inverse Distance Weighting
K_1	First dissociation constant for carbonic acid
K_2	Second dissociation constant for carbonic acid
K_f	Hydrogen fluoride constant
K_{HSO4}-	Hydrogen sulfate constant
LCW	Labrador Current waters
LOESS	Locally Estimated Scatterplot Smoothing

Mg	Magnesium
NACW	North Atlantic Central waters
NOAA/GML	National Oceanic and Atmospheric Administration/ Global Monitoring Laboratory
OA	Ocean acidification
OLS	Ordinary Least Squares
pCO_2	Partial pressure of carbon dioxide
pH	Potential of hydrogen
pH_T	Potential of hydrogen on the total scale
R^2	Coefficient of Determination
SD	Standard deviation
SIR	Substrate-inhibitor ratio
TA	Total alkalinity
TRIS	Tris(hydroxymethyl)aminomethane
USA	United States of America
Ω_A	Saturation state of aragonite
Ω_C	Saturation state of calcite